The Effects of Green Density, Heating Rate and Pressure during Sintering of Inconel 718

David Levasseur
Department of Mining and Materials Engineering
McGill University, Montreal
August 2015

A thesis submitted to McGill University in partial fulfillment of the requirements of the degree of Doctor of Philosophy

ABSTRACT

Two methods are used to produce Inconel 718 by powder metallurgy (PM): metal injection molding (MIM) followed by pressureless sintering (PS) and hot isostatic pressing (HIPing), and direct HIP. It would be advantageous to directly sinter Inconel 718 without resorting to HIP. The challenge in PS of Inconel 718 is to obtain full density, whereas in pressure assisted sintering the formation of prior particle boundary (PPB) carbides are reducing the high temperature strength of the alloy. Different PM techniques are evaluated as potential alternative to HIP. Supersolidus liquid phase sintering (SLPS) of Inconel 718 is studied to define a process window. Sintering of slip cast compacts and cold gas dynamic spray (CGDS) deposits is compared to assess the advantage of using high green density on the final density. The effect of high heating rates on densification is evaluated in a specially designed experiment using free pressureless spark plasma sintering (FPSPS). Finally, the production of Inconel 718 by spark plasma sintering (SPS) is tested as a pressure assisted alternative to HIP.

Differential scanning calorimetry (DSC) of the powder exhibits two low temperature eutectics at 1098°C and 1247°C, which are identified as γ/Laves and γ/NbC eutectics respectively. The liquid fraction is temperature dependent and has a substantial effect on sintering kinetics and final density. Liquid fraction is also responsible for distortion, but through the definition of a softening parameter it is possible to predict the onset of distortion. As Inconel 718 softening parameter increases beyond 0.0066 $\mu m^{1/3}$, distortion occurs. Sintering temperatures lower than 1250°C yield under 14% liquid fraction, which do not induce enough densification.

CGDS of Inconel 718 permits the formation of high density deposits (97%). The spray parameters yielded an average particle velocity of 750 m/s, while the gas stream was at a temperature of 800°C. In that context, the deposition efficiency is 30%. Post deposition sintering treatment increases the density to 99.7%. Conventional solution heat treatment and aging of sintered CGDS deposits increases their flexural strength; however, several interparticle voids are

observed on the fracture surface which indicates that weak bonding regions are still present after the sintering treatment. The high green density was effective in promoting full density after sintering.

FPSPS is used to sinter Inconel 718 at heating rates from 15°C/min to 200°C/min. Evaluation of the liquid fraction formation exhibits a correlation between heating rate and temperature of liquation. The sintering data is used to construct a master sintering curve (MSC), which provides information on the sintering mechanism. Two different MSC are needed to describe the sintering behavior at heating rates lower than 50°C/min and higher than 75°C/min. The associated activation energy computed for each MSC are 250 kJ/mol and 198 kJ/mol, which is in line with the niobium diffusion activation energy. Using high heating rates (>75°C/min) effectively reduces the thermal work required for sintering.

Sintering Inconel 718 by SPS at 1200°C with 50 MPa pressure yields full density; however, PPB carbides are formed when the sintering temperature exceeds 1100°C. SPS of Inconel 718 presents two densification events at 1100°C and 1175°C, where the density abruptly increases by more than 5%. The densification events are positively related to the formation of a liquid phase at 1100°C (γ/Laves) and supersolidus liquid phase at 1165°C, as predicted by Thermocalc™. The formation of PPB carbides stems from the niobium and titanium enriched liquid phase present at the neck between particles.

RÉSUMÉ

Deux méthodes sont utilisées pour produire des pièces d'Inconel 718 par métallurgie des poudres (MP): le moulage par injection de métal (MIM), suivi par un frittage sans pression externe (FSP) et un pressage isostatique à chaud (HIPing); ou un frittage direct par HIP. Il serait avantageux de fritter directement l'Inconel 718 sans avoir recours au procédé de HIP. Le défi du procédé FSP est d'obtenir la pleine densité; alors que le frittage assisté par pression provoque l'apparition de carbures sur les anciennes surfaces des particules de poudres (ASPP), qui réduisent la résistance mécanique à température élevée de l'alliage. Différentes techniques de MP sont évaluées comme alternative potentielle au procédé de HIP. Le frittage en phase liquide supersolidus (FPLS) de l'Inconel 718 est étudié pour définir une fenêtre de traitement. Le frittage de produits compacts par projection thermique à froid (PTF) est comparé pour évaluer l'avantage d'utiliser une densité initiale élevée. L'effet des taux élevés de chauffage sur la densification est évalué dans une expérience utilisant le frittage sans pression dans un équipement de frittage par courant pulsé (FPSPS). Enfin, la production d'Inconel 718 par frittage par courant pulsé est testée en tant que solution de rechange au procédé de frittage direct par HIP.

La calorimétrie différentielle à balayage (DSC) de poudre d'Inconel 718 présente deux eutectiques à basse température à 1098 ° C et 1247 ° C, qui sont identifiés comme eutectiques γ / Laves et γ / NBC respectivement. La fraction liquide est fonction de la température et a un effet notable sur la cinétique de frittage et la densité finale. La fraction liquide est également responsable de la distorsion. Par contre, à travers la définition d'un paramètre de ramollissement, il est possible de prévoir l'apparition de la distorsion. Celle-ci est prédite lorsque le paramètre de ramollissement de l'Inconel 718 augmente au-delà de 0,0066 $\mu m^{1/3}$. Des températures de frittage inférieures à 1250 °C produisent une fraction liquide inférieure à 14%, ce qui n'induit pas assez de densification.

La PTF de l'Inconel 718 permet la formation de dépôts de haute densité (97%). Les paramètres de projection utilisés ont donné une vitesse moyenne des particules de 750 m/s, tandis que le jet

gazeux est à une température de 800 °C. Dans ce contexte, le rendement du dépôt est de 30%. Un traitement de frittage post-déposition augmente la densité à 99,7%. Un traitement thermique conventionnel de mise en solution et de vieillissement exécuté sur les dépôts PTF frittés augmente leur résistance à la flexion. Cependant, plusieurs vides interparticulaires sont observés sur la surface de rupture ce qui indique que des régions de liaison faibles sont encore présentes après le traitement de frittage. La densité initiale élevée a été efficace dans la promotion de la pleine densité après frittage.

L'expérience de FPSPS est utilisée pour fritter l'Inconel 718 à un taux de chauffage entre 15 °C/min et 200 °C/min. L'évaluation de la fraction liquide formée présente une corrélation entre le taux de chauffage et la température de liquation. Les données de frittage sont utilisées pour construire une courbe maîtresse de frittage (MSC), qui fournit des informations sur les mécanismes de frittage. Deux MSC différentes sont nécessaires pour décrire le comportement de frittage à des vitesses de chauffage inférieures à 50 ° C/min et supérieures à 75 ° C/min. Les énergies d'activation calculées pour chaque MSC sont de 250 kJ/mol et 198 kJ/mol, ce qui est conforme à l'énergie d'activation de diffusion du niobium. L'utilisation de taux de chauffage élevés (> 75 °C/min) réduit efficacement le travail thermique nécessaire pour le frittage.

Le frittage par courant pulsé de l'Inconel 718 à 1200 °C sous une pression de 50 MPa permet d'obtenir la pleine densité. Toutefois, des carbures sont formés aux ASPP lorsque la température de frittage est supérieure à 1100 °C. Le frittage par courant pulsé de l'Inconel 718 présente deux événements de densification à 1100 °C et 1175 °C, où la densité augmente brusquement de plus de 5%. Les événements de densification sont positivement liés à la formation d'une phase liquide à 1100 °C (γ/Laves) et d'une phase liquide supersolidus à 1165 °C, comme prédit par Thermocalc^{MC}. La formation de carbures aux ASPP provient de la phase liquide enrichie en titane et niobium présent au niveau du pont entre les particules.

ACKNWOLEDGEMENTS

En premier lieu, je désire exprimer à mes parents et ma famille à quel point leur support et leur grand cœur a pu me faciliter l'accès à ce rêve. Votre soutien indéfectible au fil des années est un modèle pour moi.

McGill University has been a fantastic learning ground, and this is due in great part to my supervisor Mathieu to whom I wish to express my deepest thanks. He has been a fantastic mentor, and provided me with great opportunities to improve my technical, and scientific abilities; but the most important values he transmitted were ambition and teamwork, which will always drive me in the future. It has been a privilege working with you, and I am grateful.

Speaking of teamwork, I want to highlight the invaluable help of the whole NAIN group in the accomplishment of this work. Particularly, I would like to thank Dom, Pat, Cory (I still hope to make a breakthrough in the Brisket Theory), Ramona, Yaneth, Graeme and Jason who have warmly welcomed me in the group; the two Daves, Rosen, Bamidele, Gil, Rabab, Nesli, Phil the cookie master, and Marie-Pier. Thanks to all the Blades of Wood hockey team, we had glorious moments together. I would like to extend my thanks to Cecile, Pantcho, Renaud, Max, Holger, Florencia and Wilson for the good times we have shared.

I have to thank the skilled technical and administrative staff of our department for their assistance and counsels: Barbara, Terry, Monique, Ray, Helen, Pierre and Robert; all the researchers and technician from Institut des Matériaux Industriels (IMI) who helped me with the cold spray equipment: Bernard Harvey, Frédéric Belval and Eric Irissou; and finally, Phillip Nista for his help.

I spent the last 2 years at the employment of Centre de Métallurgie du Québec and I wish to express my gratitude to the many individuals who make the success of this special research center and especially to Gheorghe Marin for his daily support and patience, Nicolas Giguère, Bernard Tougas, Isabelle Jacob, Jeremy Carignan, and Pierrette Houle.

I should add that this work would not have been possible without the financial support from the National Science and Engineering Research Council of Canada (NSERC) and the Faculty of Engineering through the McGill Engineering Doctoral Award (MEDA).

Finalement, un remerciement très spécial à ma tendre moitié Evelyne qui a fait beaucoup de sacrifices pour m'aider à terminer cette thèse. Tu as été une source de motivation incroyable et d'une aide précieuse. Notre petite famille a reposé sur tes épaules assez longtemps, maintenant que je termine cette étape, je ne désire qu'une chose : prendre soin de toi et de notre petit Marius.

TABLE OF CONTENTS

ABSTRACT ii

RÉSUMÉ iv

ACKNWOLEDGEMENTS vi

LIST OF FIGURES xii

LIST OF TABLES xvi

CONTRIBUTIONS OF AUTHORS xvii

CHAPTER 1. INTRODUCTION 1

CHAPTER 2. BACKGROUND 4

- **2.1. SUPERALLOYS DEVELOPMENT AND APPLICATIONS** 4
- **2.2. GENERAL DESCRIPTION OF SUPERALLOYS** 7
- **2.3. INCONEL 718** 8
  - **2.3.1. Second phase formation in Inconel 718** 8
- **2.4. POWDER METALLURGY** 10
  - **2.4.1. Solid-state sintering** 10
  - **2.4.2. Liquid-phase sintering** 11
  - **2.4.3. Supersolidus liquid-phase sintering** 12
  - **2.4.4. Pressure-assisted sintering** 17
  - **2.4.5. Pressure-assisted supersolidus liquid-phase sintering** 19
  - **2.4.6. Spark plasma sintering** 19
  - **2.4.7. Sintering models** 20
- **2.5. COLD GAS DYNAMIC SPRAY** 27
- **2.6. SINTERING OF INCONEL 718** 29
  - **2.6.1. Pressureless sintering of slip cast and metal injection molded parts** 29
  - **2.6.2. Direct Hot Isostatic Pressing** 30
  - **2.6.3. Prior Particle Boundaries** 31

2.7. References 33
CHAPTER 3. OBJECTIVES 38
CHAPTER 4. EXPERIMENTAL METHODOLOGY 41
4.1. Inconel 718 Powder Feedstock 41
4.2. Differential Scanning Calorimetry 41
4.3. Preparation of the Slip Cast Inconel 718 Compacts 41
4.4. Pressureless Sintering 42
4.5. Cold Gas Dynamic Spray 44
4.6. Spark Plasma Sintering and Free Pressureless Spark Plasma Sintering 44
4.7. Optical Microscopy 47
4.8. Scanning Electron Microscopy 47
4.9. X-ray diffraction 48
4.10. Hardness Testing 48
4.11. Flexural Strength Testing 48
4.12. References 49
CHAPTER 5. SUPERSOLIDUS LIQUID PHASE SINTERING MODELING OF INCONEL 718 SUPERALLOY 50
5.1. PREFACE 50
5.2. Abstract 50
5.3. Introduction 51
  5.3.1. The SLPS Model 52
5.4. Experimental Methods 55
5.5. Results and discussion 57
  5.5.1. Thermal analysis 57
  5.5.2. Densification and microstructure evolution 59
  5.5.3. SLPS model prediction of sintering and distortion onset for Inconel 718 62
5.6. References 66

CHAPTER 6. PRESSURELESS SINTERING OF COLD SPRAYED INCONEL 718 DEPOSIT 68

6.1. PREFACE 68

6.2. ABSTRACT 68

6.3. INTRODUCTION 69

6.4. EXPERIMENTAL PROCEDURES 70

6.4.1. Starting Powder 70

6.4.2. Cold Spray Deposition Trials 71

6.4.3. Sintering Treatment 71

6.4.4. Solution and Aging Treatments 72

6.4.5. Characterization of the sintered components 72

6.5. RESULTS AND DISCUSSION 73

6.5.1. Densification 73

6.5.2. Microstructure evolution 77

6.5.3. Second phase formation 81

6.6. MECHANICAL PROPERTIES 83

6.6.1. Hardness 83

6.6.2. Three-point bending test 85

6.7. REFERENCES 89

CHAPTER 7. EFFECT OF HEATING RATE ON THE PRESSURELESS SINTERING DENSIFICATION OF A NICKEL BASED SUPERALLOY ...91

7.1. PREFACE 91

7.2. ABSTRACT 91

7.3. INTRODUCTION 92

7.3.1. Master Sintering Curve 92

7.4. EXPERIMENTAL METHOD 95

7.5. RESULTS 97

7.5.1. Densification experiments 97

7.5.2. Assessment of porosity distribution 99

7.5.3. Assessment of the grain size evolution 100
7.5.4. Assessment of the microstructure evolution 102
7.5.5. Determination of Q and MSC fit 105
7.6. Discussion 107
7.7. References 112
CHAPTER 8. SPARK PLASMA SINTERING OF INCONEL 718 115
8.1. PREFACE 115
8.2. Abstract 115
8.3. Introduction 116
8.4. Experimental 117
8.5. Results and discussion 120
8.5.1. Effect of sintering temperature on density 120
8.5.2. Liquation of Inconel 718 123
8.5.3. Prior particle boundaries 127
8.5.4. Effect of heating rate 132
8.6. References 134
CHAPTER 9. GENERAL DISCUSSION 137
9.1. Sintering of Inconel 718 in the SLPS regime 138
9.2. The effect of green density on Inconel 718 sintering 140
9.3. The role of heating rate in Inconel 718 sintering 142
9.4. Pressure assisted sintering of Inconel 718 143
9.4.1. Effect of processing parameters on the microstructure evolution 145
9.4.2. The formation of PPB carbides in pressure assisted sintering 147
9.5. Summary 149
CHAPTER 10. CONCLUSION 152
CHAPTER 11. CONTRIBUTIONS TO ORIGINAL KNOWLEDGE 156

LIST OF FIGURES

FIGURE 2-1 : SCHEMATIC SIMPLIFIED OVERVIEW OF GAS TURBINE ZONES AND COMPONENTS (IMAGE ADAPTED FROM DONACHIE & DONACHIE [2.1]) 5

FIGURE 2-2: COMPARISON OF THE NUMBER OF PROCESSING STEPS AND RAW MATERIAL USAGE FOR TRADITIONAL IM, HIP+FORGE, AND DIRECT HIP PROCESSES (IMAGE ADAPTED FROM DONACHIE & DONACHIE [2.1]) 6

FIGURE 2-3: DIAGRAM OF THE SINTERING SEQUENCE DURING SLPS (ADAPTED FROM GERMAN [2.16]) 13

FIGURE 2-4: FRACTIONAL COVERAGE AS A FUNCTION OF LIQUID VOLUME FRACTION AND DIHEDRAL ANGLE (ADAPTED FROM LIU *ET AL.* [2.18]) 14

FIGURE 2-5: COMPARISON OF THE NORMALIZED GRAIN SIZE IN ALUMINA AS A FUNCTION OF DENSITY OBTAINED BY PRESSURELESS SINTERING, HP, AND SPS. PRESSURE-ASSISTED SINTERING TECHNIQUES PRODUCED FINER GRAIN SIZE INDEPENDENT OF THE APPLICATION OF AN ELECTRIC FIELD (ADAPTED FROM GERMAN [2.23]) 20

FIGURE 2-6 : MASTER SINTERING CURVE FOR BORON DOPED 316L STAINLESS STEEL POWDERS SINTERED AT 5 K/MIN SHOWING THE THREE CURVE FITTING REGIONS ASSOCIATED TO SOLID STATE, LIQUID FORMATION (OVER SOLIDUS TEMPERATURE) AND HIGHER TEMPERATURE SLPS. [2.45] 22

FIGURE 2-7 : ILLUSTRATION OF THE ALGORITHM PROPOSED BY BRAGINSKY TO ANNIHILATE VACANCY AT GRAIN BOUNDARIES (BLACK LINES) [2.42] 27

FIGURE 2-8: SCHEMATIC REPRESENTATION OF CGDS PROCESS (ADAPTED FROM GÄRTNER *ET AL.* [2.51]) 28

FIGURE 2-9: PRESSURELESS SINTERING DENSITY AS A FUNCTION OF SINTERING TEMPERATURE FOR 5-H HOLDING CYCLES (ADAPTED FROM HAJMRLE *ET AL.* [2.57]) 29

FIGURE 2-10: HOT ISOSTATIC PRESSING PROCESS FOR CONSOLIDATION OF POWDER METALLURGY PARTS (ADAPTED FROM GERMAN [2.23]) 30

FIGURE 2-11: ELECTRON MICROGRAPH OF HIPED STRUCTURES (A)275 PPM O2 (B)180 PPM O2, AND (C)140 PPM O2 (ADAPTED FROM RAO ET AL. [2.71]) 33

FIGURE 4-1 : SLIP CAST INCONEL 718 COMPACT WITH 12% WEIGHT AMMONIUM ALGINATE SOLUTION 42

FIGURE 4-2 : VACUUM FURNACE UTILIZED TO SINTER SLIP CAST INCONEL 718 AND CGDS DEPOSITS 43

FIGURE 4-3 : CGDS DELAVAL NOZZLE AND FIXTURE USED TO COLD SPRAY INCONEL 718 44

FIGURE 4-4 : THERMAL TECHNOLOGY LLC 10-3 SPS PRESS USED TO SINTER INCONEL 718 POWDER IN THE SPS AND FPSPS EXPERIMENTS 46

FIGURE 4-5 : SKETCH OF THE SPS DIE ASSEMBLY (A) AND FPSPS EXPERIMENT DIE ASSEMBLY (B) 46

FIGURE 4-6 : TINUS-OLSEN H25K-S UNIVERSAL TESTING MACHINE 49
FIGURE 5-1 : A) SEM IMAGE OF THE POWDER AND B) PARTICLE SIZE ANALYSIS 55
FIGURE 5-2 : DSC TRACE OF THE INCONEL 718 POWDER BETWEEN ROOM TEMPERATURE AND 1433K SCANNED AT 10K/MIN 58
FIGURE 5-3 : SOLID FRACTION DETERMINED FOR INCONEL 718 AS A FUNCTION OF TEMPERATURE BY DSC MEASUREMENT AND BY EXPERIMENTAL OBSERVATION [5.22] 59
FIGURE 5-4 : SINTERED DENSITY MEASURED IN THIS STUDY AND FROM OTHER WORKS [5.6, 5.8, 5.10-5.11] 60
FIGURE 5-5 : GRAIN SIZE DATA MEASURED IN THIS STUDY AND FROM OTHER WORKS [5.5-5.6, 5.8, 5.11, 5.25] 61
FIGURE 5-6 : LOG–LOG PLOT USED TO DETERMINE THE GRAIN GROWTH EXPONENT MEASURED IN THIS STUDY AND BY ANGER [5.25] 63
FIGURE 5-7 : SOFTENING PARAMETER CALCULATED FOR THE EXPERIMENTAL CONDITIONS USED IN THIS STUDY AND IN OTHER WORKS [5.5-5.6, 5.8, 5.10-5.11] 64
FIGURE 6-1 : PARTICLE SIZE DISTRIBUTION OF THE INCONEL 718 POWDER 71
FIGURE 6-2 : OPTICAL MICROGRAPH OF THE AS-SPRAYED COATING AND (B) SEM MICROGRAPH OF THE AS-SPRAYED COATING SHOWING POOR INTERPARTICLE BONDS. 75
FIGURE 6-3 : (A) POROSITY MEASUREMENT OF EACH SINTERING CONDITION AND (B) OPTICAL MICROGRAPH FROM A SAMPLE SINTERED AT 1250°C FOR 60 MIN. 77
FIGURE 6-4 : (A) AVERAGE GRAIN SIZE OF THE SINTERED DEPOSITS, (B) GRAIN SIZE DISTRIBUTION OF THE DEPOSIT SINTERED AT 1250°C FOR 10 MIN, 60 MIN, AND 180 MIN. 79
FIGURE 6-5 : LOGARITHMIC PLOT OF GRAIN SIZE VS TIME. THE GRAIN GROWTH EXPONENT CAN BE FOUND FROM THE SLOPE OF THE LINEAR REGRESSION 80
FIGURE 6-6 : MICROGRAPHS FROM INCONEL 718 COLD SPRAY DEPOSIT SINTERED AT A) 1200°C-1H; B) 1225°C-1H; C) EDS ANALYSIS OF THE WHITE CARBIDE PARTICLE; D) HIGH MAGNIFICATION OF THE 1250°C-3H SAMPLE SHOWING δ AND γ” PRECIPITATES. 80
FIGURE 6-7 : (A) ISOTHERMAL EVOLUTION OF CARBIDE VOLUME FRACTION; (B) ISOTHERMAL COARSENING OF THE CARBIDES 82
FIGURE 6-8: MICROGRAPH OF THE AS-SPRAYED DEPOSIT A) BEFORE AND B) AFTER INDENTATION 84
FIGURE 6-9 : MICROGRAPH FROM THE FRACTURE SURFACE OF THE AS-SPRAYED THREE POINT BENDING SAMPLE AT LOW MAGNIFICATION (A) AND HIGH MAGNIFICATION (B) 87
FIGURE 6-10 : MICROGRAPH FROM THE FRACTURE SURFACE OF THE THREE-POINT BENDING SAMPLES SINTERED AT 1250°C FOR 60 MIN (A,B) AND 180 MIN (C,D) 88
FIGURE 7-1: ASSEMBLY USED FOR PRESSURELESS SINTERING IN THE PULSED ELECTRIC CURRENT SINTERING (PECS) APPARATUS. 96
FIGURE 7-2: SINTERING DATA FITTED WITH SIGMOIDAL CURVES FOR HEATING RATES OF 15 K/MIN, 25 K/MIN, 50 K/MIN, 75 K/MIN, 100 K/MIN, AND 200 K/MIN. 98
FIGURE 7-3: ONSET TEMPERATURE OF DENSIFICATION FOR EACH HEATING RATE EXPERIMENT. 98

Figure 7-4: Porosity measurement across the 200 K/min compact sintered at 1635 K. 100
Figure 7-5: Micrograph from an etched sample sintered at 1476 K at 15 K/min........... 101
Figure 7-6: Average grain size evolution with respect to density plotted for each heating rate used in this study; error bars represent the 99% confidence intervals around each value. 102
Figure 7-7: Optical micrograph of the liquation zone and γ/Laves eutectic for the samples sintered at a) 15 K/min at 1549 K and b) 200 K/min at 1635 K. 103
Figure 7-8: Measured liquid fractions of several sintered Inconel 718 samples for heating rates from 25 K/min to 200 K/min. The liquid fraction observed is compared with the calculated onset temperature of sintering identified for each heating rate. 103
Figure 7-9: Temperature of the first observation of liquid phase and γ/Laves eutectic formation for each heating rate. The error bars indicate the highest temperature sample in which no liquid or eutectic was observed.......................... 104
Figure 7-10: EDS linescan of the eutectic zone (a), the liquation zone (the arrow shows the region analyzed) (b) linescan Nb profile.. 104
Figure 7-11: Residual plot for different values of Q for the low heating rate master sintering curve (MSC) (left) and the high heating rate MSC (right). 105
Figure 7-12: MSC for Inconel 718 powders sintered in a non-contacting pulsed DC field with an apparent activation energy of 198 kJ/mol for the low and high heating rates. 107
Figure 7-13: Liquid fraction as a function of thermal work for low and high heating rates. 112
Figure 8-1 : Inconel 718 particle size distribution measured by laser interferometer 118
Figure 8-2 : Inconel 718 final density after SPS at different temperatures and applied pressures.. 122
Figure 8-3 : Inconel 718 SPS microstructure after sintering at a temperature of a)1000°C, b) 1125°C, c) 1175°C and d) Particle surface observed in 1150°C interrupted sintering sample.. 123
Figure 8-4 : Liquid fraction of Inconel 718 determined by DSC and by Thermocalc™ 124
Figure 8-5 : EDS analysis of the remaining dendritic structure after sintering in SPS at 1125°C.. 125
Figure 8-6 : EDS linescan taken on the PPB of Inconel 718 sintered at 1075°C in SPS for 1 min. (a) The linescan locations is given by the black line on the micrograph, (b) enlargement of the linescan area (same scale as *Position* axis in (c)) and (c)

elemental profile across the PPB at position 3µm and capturing a grain boundary carbide at position 5.5µm 128

Figure 8-7 : Two EDS linescans taken on the PPB of Inconel 718 sintered at 1200°C in SPS for 1 min. The linescans locations are given by the black line on the micrograph, b) chemical profile across a PPB particle at position 0.8µm, c) chemical profile across a particle free PPB region at position 0.8µm 129

Figure 8-8 : a) Electrolytic dissolution residue of Inconel 718, b) EDS analysis of the blocky particle observed in a) and c) XRD spectrum of the dissolution residue showing MC carbides and Inconel 718 γ matrix 130

Figure 8-9 : Neck region between two Inconel 718 particles from the 1150°C interrupted sintering test 131

Figure 9-1 : Comparison of the porosity fraction evolution during isothermal holding of slip cast samples and CGDS samples on semi-log scale 141

Figure 9-2 : The effect of pressure on the porosity after sintering (the result at 0 MPa was obtained in a resistance furnace, all the other results were obtained in the SPS press) 144

Figure 9-3 : Comparison of the microstructure obtained for similar density samples and different sintering processes 146

Figure 9-4 : Microstructure of samples sintered at 1200 °C a) CGDS, b) FPSPS, c) Slip cast and d) SPS 148

LIST OF TABLES

TABLE 2-1: EFFECTS OF ALLOYING ELEMENTS FOR INCONEL 718 (ADAPTED FROM BRADLEY [2.3]) 9
TABLE 2-2 : PARAMETERS DEVELOPED FOR THE SOVS MODEL 24
TABLE 5-1 : CHEMICAL ANALYSIS OF THE AMDRY 1718 POWDER 56
TABLE 5-2: PARAMETERS USED TO COMPUTE $Z_{DISTORTION}$ AND Z_{ONSET} 65
TABLE 6-1 : CHEMICAL COMPOSITION OF THE INCONEL 718 POWDER, AS PROVIDED BY THE SUPPLIER 71
TABLE 6-2: MEASURED VICKERS MICROHARDNESS FOR AS-SPRAYED, SINTERED AND AGED DEPOSITS 85
TABLE 6-3 : FLEXURAL STRENGTH AND STRAIN RESULTS FOR THE SINTERED CS SAMPLES 86
TABLE 7-1: SUMMARY OF PUBLISHED DATA ON THE SINTERING OF INCONEL 718 MIM PARTS 93
TABLE 7-2 : CHEMICAL ANALYSIS OF THE AMDRY 1718 POWDER 95
TABLE : 7-3 : LATTICE DIFFUSION ACTIVATION ENERGY OF THE PRINCIPAL CHEMICAL CONSTITUENTS OF INCONEL 718 IN NICKEL 107
TABLE : 7-4 : MELTING AND SOLIDIFICATION EVENTS FOR INCONEL 718 108
TABLE 7-5 : DIFFUSION DEPTH OF NB AT 1498K FOR HEATING RATES OF 15K/MIN TO 200 K/MIN 109
TABLE 8-1 : INCONEL 718 POWDER COMPOSITION 117
TABLE 8-2 : SINTERING PARAMETERS USED FOR THE COMPACTION OF INCONEL 718 SAMPLES.... 119
TABLE 8-3 : INCONEL 718 SINTERING PARAMETERS AS A FUNCTION OF THE HEATING RATE IN SPS 132

CONTRIBUTIONS OF AUTHORS

This thesis is manuscript-based and contains four manuscripts, of which one is published and the three others are submitted for publication. As the first author on the four manuscripts, I conducted all the experimental work and wrote the manuscripts. The contributions of the co-authors for each manuscript are presented below.

Prof. Stephen Yue offered technical expertise and assistance with the cold gas dynamic spray process and creation of the manuscript in Chapter 6.

Prof. Mathieu Brochu supervised the entire project and supplied technical and scientific advice throughout.

CHAPTER 1. INTRODUCTION

Powder metallurgy (P/M) is a process for fabricating near-net-shape, complex metallic parts with the advantages of reducing raw material usage and permitting close tolerances. P/M of superalloys has been explored since the 1950s with the development of oxide dispersion strengthened alloys (e.g., TD-nickel) [1.1]. The process has been applied to many other alloys since then and has allowed more flexibility in alloy development. The prime advantage of the P/M process is its ability to form parts with fine grain structure while avoiding macrosegregation, which is unavoidable in cast billets of highly alloyed superalloys. Macrosegregation limits the formability of such superalloys cast billets since the mechanical response during thermomechanical transformation is inhomogeneous [1.2]. Moreover, alloying content must be kept low relative to P/M compositions in order to avoid severe macrosegregation.

The P/M process was thus first used to produce billets for subsequent superplastic forming (SPF). In this processing route, the superalloy powder is canned in stainless steel containers and consolidated under hot isostatic press (HIP). The consolidated billet is fully dense, fine grained, and homogeneous. It can then be used in SPF processes such as the Pratt & Whitney Gatorizing^{TM} process [1.3].

Near-net-shape P/M, on the other hand, is truly the most economical process with respect to material use and reduction of machining. Consolidation techniques to obtain near-net-shape P/M production are pressureless sintering, hot pressing, and direct HIPing [1.4]. The pressureless sintering route is applied to resin-bound powder obtained by the metal injection molding (MIM) process or binder-jetting (BJ) additive manufacturing process. The two processes allow the economical production of complex parts. The resin is removed by thermal or solvent cleaning before the sintering treatment. Hot pressing is the uniaxial compaction of powder in a die at high temperatures. The process permits somewhat limited part complexity but is an interesting low-cost alternative to direct HIP. In the direct HIP process, a stainless steel container is filled with powder, degassed, and sealed for the HIP cycle. The main difficulty of this process lies in predicting the container deformation and distortion under HIP conditions. Many trials are necessary to produce close tolerances and near-net-shape, which increases the process development cost [1.5].

Direct HIPing can be successful; however, the high cost of consolidation by HIP offsets the gain in material and machining savings. Accordingly, the main objective of this research is the exploration of other methods for the consolidation of superalloy powder.

Inconel 718 is the most used superalloy for turbine disk applications because of its low cost and satisfactory high temperature properties up to 650°C [1.3]. Near-net-shape P/M processes for the production of Inconel 718 parts other than direct HIP have yet to be validated. As such, this thesis focuses on pressureless sintering of slip cast and high density green compacts produced by cold gas dynamic spray, the effect of the heating rate, and the pressure-assisted spark plasma sintering technique.

THESIS OUTLINE

This thesis is manuscript based: appropriate background information is presented in chapter 2; the objectives of the research are given in chapter 3; the experimental procedures are detailed in chapter 4; chapters 5 through 8 are the result chapters, each corresponding to a publication that was submitted throughout the course of this research; chapter 9 is the general discussion; the summary of the thesis findings is provided in chapter 10; and the most important contributions to the scientific literature are discussed in chapter 11.

REFERENCES

1.1. Gessinger, G.H., *Powder metallurgy of superalloys*. Butterworths monographs in materials. 1984, London ; Boston: Butterworths. 348 p.

1.2. Donachie, M.J. and S.J. Donachie, *Superalloys : a technical guide*. 2nd ed. 2002, Materials Park, OH: ASM International, 439 p.

1.3. Reed, R.C., *The superalloys : fundamentals and applications*. 2006, Cambridge, UK; New York: Cambridge University Press.

1.4. German, R.M., *Sintering theory and practice.* Sintering Theory and Practice, by Randall M. German, pp. 568. ISBN 0-471-05786-X. Wiley-VCH, January 1996., 1996. **1**.

1.5. National Materials Advisory Board (1981), *Superalloys from Powder: Production and Properties.* (Report NMAB-369), Washington D.C.: National Academy Press

CHAPTER 2. BACKGROUND

2.1. SUPERALLOYS DEVELOPMENT AND APPLICATIONS

Superalloys are a class of material developed for high temperature applications like gas turbines (used as jet engines or for power generation). The need for corrosion- and creep-resistant materials have pushed the development of advanced stainless steels, which have been termed superalloys. As the amount of alloying elements increases, the alloys are less iron based and become more nickel or cobalt based. A typical example of a heat-resistant alloy is the Nichrome heating element wire found in a variety of applications from industrial heaters to kitchen toasters. The Nichrome-type alloys are not superalloys; they are resistant to hot corrosion but do not have the required high temperature strength. However, minor additions of alloying elements to Nichrome can transform it into an exemplary hot corrosion- and creep-resistant superalloy that can be used in gas turbines at temperatures neighboring 600°C. The key material property of superalloys is thermal stability, and a major objective of materials engineers when developing new grades of superalloys is extending the temperature limit of existing alloys.

The quest for progressively higher heat resistance is driven by turbine efficiency. As for any heat engine, gas turbine efficiency is directly related to combustion temperature. The heat resistance of the ceramics and superalloys that compose the engine are one of the factors limiting combustion temperature increases. Other technologies have been adopted to increase combustion temperatures such as internal cooling and ceramic coatings; however, the high temperature performance of materials is the subject of continued research efforts.

Figure 2.1 presents a schematic representation of a gas turbine. The main components are the fan, compressor, combustion chamber, and turbine. The compressor is composed of disk couplings between the compressor blades and the central shaft. The compressor increases the pressure of incoming air as it travels toward the combustion chamber. In the combustion chamber, fuel is mixed with pressurized air and ignited. The combustion gases are accelerated through the turbine, which drives a shaft to supply mechanical energy to the compressor. The high velocity exhaust gases supply the thrust to accelerate the airplane. Each zone experiences different temperature and stress levels. The components closest to the combustion chamber are heated by 1400°C gases, but the component temperatures decrease with distance from the hot combustion chamber. This thesis focuses on the turbine disk, which is the coupling between the shaft and the blades in the turbine zone. Low pressure turbine disk alloys must sustain temperatures up to 540°C; however, the high rotational speed induces severe stress conditions as well. Superalloys can sustain the high temperatures and high stresses prevailing within the turbine disk; however, superalloys are difficult to shape, necessitating the development of improved production processes.

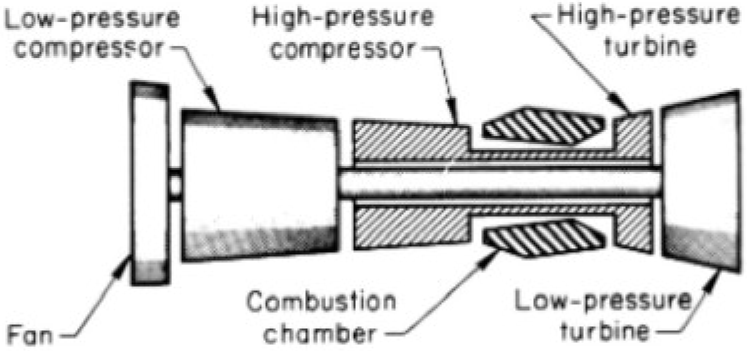

Figure 2-1 : Schematic simplified overview of gas turbine zones and components (image adapted from Donachie & Donachie [2.1])

Superalloy parts are manufactured using one of three methods: casting, wrought ingot metallurgy (IM), or powder metallurgy (P/M). Casting is employed to produce hot section parts with increased creep resistance. Directional solidification technology allows the production of columnar grain or single crystal parts, which have desirable creep resistance. On the other hand, the IM and P/M methods are used for the same applications, such as turbine disk production.

A comparison of the IM and P/M near-net-shape processes is shown in Figure 2.2. The P/M process dramatically reduces the number of production steps and decreases the lead time for part production. Additionally, the metal input is reduced from 95 kg to 18 kg. The ratio of the weight of the material entering the fabrication process to that of the final product is termed the buy-to-fly (BTF) ratio. In this particular case, the BTF of the IM process is 19, whereas the direct hot isostatic pressing (HIP) process BTF is 3.6.

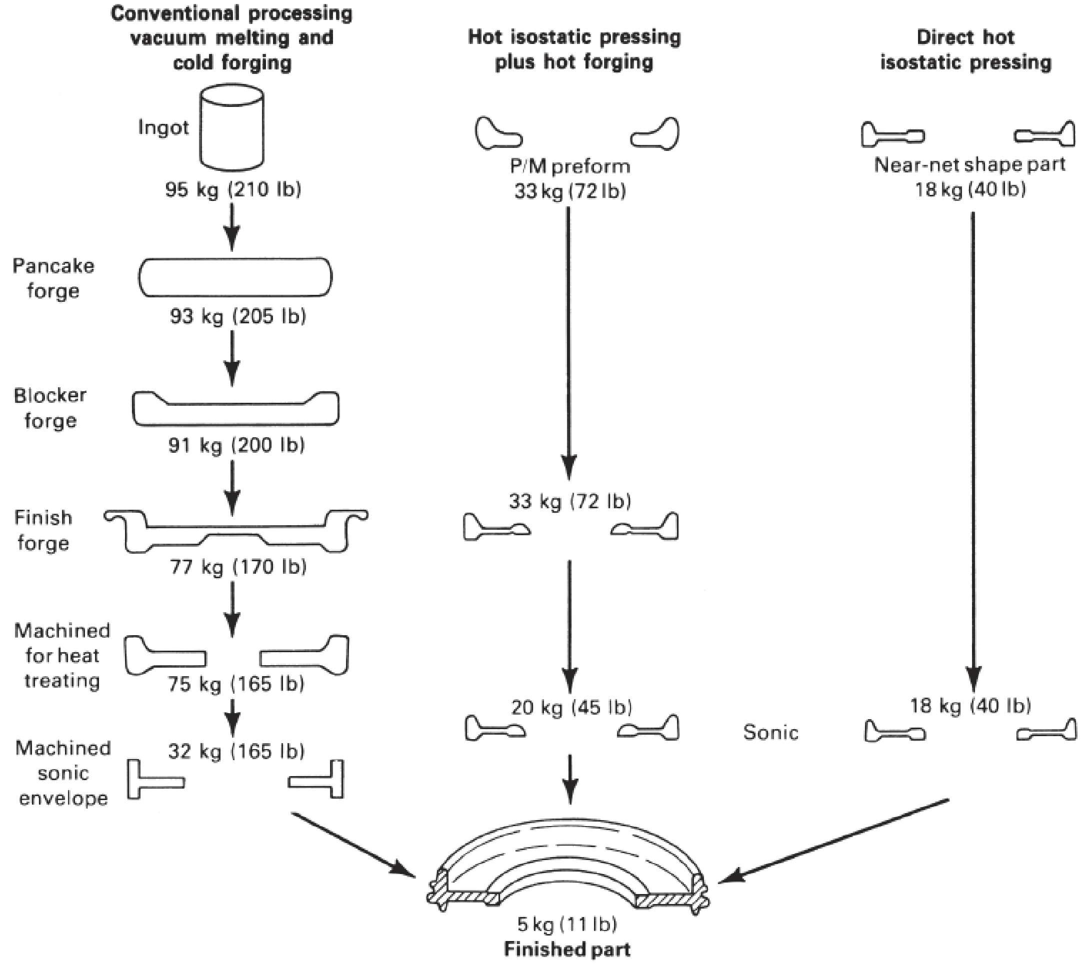

Figure 2-2: Comparison of the number of processing steps and raw material usage for traditional IM, HIP+Forge, and direct HIP processes (image adapted from Donachie & Donachie [2.1])

2.2. GENERAL DESCRIPTION OF SUPERALLOYS

Superalloys are classified into three groups based on their composition: nickel-based, nickel–iron-based, and cobalt-based groups. The manufacturing of each group employs a different strengthening mechanism based on either solid-solution strengthening or second-phase hardening.

Nickel-based superalloys can be solid-solution strengthened by the addition of Fe, Co, W, or Mo as in the Hastelloy X and Inconel 625 alloys. However, the best creep resistance is obtained by precipitation hardening of the γ' phase ($Ni_3(Al,Ti)$) when Al and Ti are added to nickel-based superalloys. Niobium additions allow the formation of γ'' (Ni_3Nb, body-centered tetragonal) and δ (Ni_3Nb, orthorhombic) phases, which are the main strengthening precipitates in Inconel 718. The last family of nickel-based superalloys are the oxide-dispersed strengthened (ODS) alloys. The addition of small oxide particles within alloys improves the high temperature creep resistance at the expense of room temperature strength.

The nickel–iron-based superalloys are the most similar to stainless steels. Addition of solid-solution strengtheners or alloying with aluminum and titanium confers these alloys with better high temperature properties than their stainless steel counterparts. Incoloy 800H, Incoloy 901, and A-286 are typical alloys from the nickel–iron group. Whether Inconel 718 is part of the nickel-based or iron–nickel-based group is debated [2.1-2.2]; it has been included with the nickel group here because its iron level is low.

Finally, the cobalt-based superalloys have good high temperature stability but do not exhibit the same level of high temperature mechanical properties as the nickel- and nickel-iron-based superalloys. The main strengthening mechanism of these alloys relies on carbide formation and solid-solution strengthening. Since no γ' phase or any equivalent phase is known to precipitate in cobalt-based superalloys, their high temperature resistance is limited compared to the nickel- and iron–nickel-based alloys.

2.3. INCONEL 718

As previously mentioned, Inconel 718 is a nickel-based superalloy. It has found widespread use in low- and intermediate-temperature disk fabrication. Inconel 718 is the most used superalloy, not for its superior properties, but for its availability and low price. A surge in Inconel 718 utilization occurred in the 1970s while cobalt alloys were scarcely available and the alloying element prices were rising. The lower nickel content and the absence of cobalt from Inconel 718 contributed to its low cost. Nonetheless, Inconel 718 can be used at temperatures up to 650°C and has good forgeability, which has contributed to its adoption for many turbine disk applications.

The roles of the various elements comprising Inconel 718 are listed in Table 2-1. Nickel has a high solubility, which makes it ideal for solid-solution strengthening. The matrix (γ) is a face-centered cubic (FCC) structure phase composed of Ni, Cr, Fe, Mo, Ti, Al, Ta, Nb, and Mn. Of these elements, some are most useful in forming secondary phases. Al, Ti, Nb, and Ta can combine with nickel to form Ni_3X precipitates.

2.3.1. Second phase formation in Inconel 718

Aluminum and titanium precipitate as γ' ($Ni_3(Al,Ti)$), which has a $L1_2$ structure and is coherent with the matrix. Niobium precipitates as a γ'' phase (Ni_3Nb), which is metastable and has a DO_{22} (bct) structure; it appears as fine (≈30 nm) disk-shaped precipitates coherent with the matrix [2.4]. Many nickel-based superalloys rely solely on γ' for strengthening, but the principal strengthening phase in Inconel 718 is the γ'' phase. The stable Ni_3Nb phase (δ) has an orthorhombic ($D0_a$) structure; it precipitates along the grain boundaries when the alloy is aged at temperatures between 700°C and its solvus (≈1000°C). When the δ phase appears there is normally a hardness decrease due to γ'' depletion in the vicinity [2.5].

Paulonis *et al.* [2.4] first showed the presence of γ″ (≈15% vol.) in Inconel 718 along with small quantities of γ′ (≈4% vol.). They observed rapid coarsening of γ″ at temperatures above 750°C and the eventual dissolution and formation of the more stable δ phase. A few workers have studied the precipitation sequences of γ′ and γ″. Sundararaman *et al.* [2.6] observed simultaneous precipitation of (Al + Ti) and Nb at a ratio of 0.66. Cozar and Pineau [2.7] obtained γ′ precipitates before γ″ for ratio exceeding 0.8, and they observed a γ″ precipitate dissolution temperature of 700°C. When aging the alloy at temperatures over 700°C, the γ″ phase was replaced by the δ phase.

Table 2-1: Effects of alloying elements for Inconel 718 (adapted from Bradley [2.3])

Effect	Elements
- Solid solution hardening	Co, Cr, Fe, Mo, Ta
- FCC matrix stabilizer	Co
- Carbide form	
o MC type	Ta, Ti, Mo, Nb
o M_7C_3 type	Cr
o $M_{23}C_6$ type	Cr, Mo
o M_6C type	Mo
- Carbonitrides (M(CN) type)	C, N
- Forms γ′ $Ni_3(Ti,Al)$	Al, Ti
- Forms γ″ Ni_3Nb (metastable)	Fe*, Nb
- Forms δNi_3Nb (stable)	Fe*, Nb
- Oxidation resistance	Al, Cr, Ta
- Hot corrosion resistance	La, Th
- Sulfidation resistance	Cr
- Enhances creep-rupture properties by grain-boundary morphology changes	B**
- Improves intermediate temperature ductility	Hf

- Causes grain boundary segregation *Ni$_3$Nb do not form in Ni–Nb alloys. **High quantity will promote boride formation.	B, C

In addition to the precipitation of γ' and γ'', an MC carbide phase also precipitates during aging of Inconel 718. The MC carbides are typically NbC or TiC and are found at the grain boundaries where they may be flanked by precipitate-free zones as reported by Boesch [2.8]. After aging, MC carbides were found to form on some grain boundaries after 168 h at 700°C and after a short time at 750°C. However, upon aging at 800°C, the δ phase was found to compete with carbides for nucleation sites on grain boundaries, and at 900°C, only the δ phase was found at grain boundaries.

2.4. POWDER METALLURGY

Sintering is the consolidation of powder particles under heat through necking and mass transport. The aim of the process is to remove the voids between powder particles to obtain a fully dense object. Broadly, three types of sintering are distinguished: solid-state sintering, liquid-assisted sintering, and pressure-assisted sintering.

2.4.1. Solid-state sintering

Solid-state sintering is driven by the reduction of free surfaces and the curvature of the pores within the powder compact. Elimination of surfaces is thermodynamically favorable, and diffusion processes are responsible for the atomic motions toward the neck region between two particles. As a result, small particles and high diffusivity are necessary to obtain high sintering rates. Practically, solid-state sintering is improved when powder particle diameters are under 10 µm; however, particles exceeding 100 µm cannot be sintered to full density by solid-state sintering [2.9].

The diffusion mass transport occurs through volume diffusion, grain-boundary diffusion, and surface diffusion. Among the three mass transport mechanisms mentioned, only surface diffusion does not cause densification. The grain-boundary and volume diffusions are responsible for atomic movement from the particle core toward the neck. On the other hand, surface diffusion enables atomic motion from the particle surface toward the neck. This causes coarsening of the neck without densification. Consequently, the surface diffusion mass transport mechanism should be avoided if fully dense P/M parts are sought. As the surface diffusion mechanism is dominant only at low temperatures, high heating rates can be used to limit the extent of surface diffusion and achieve high sintering rates.

2.4.2. Liquid-phase sintering

Liquid-phase sintering (LPS) occurs when one constituent of the alloy melts and assists densification. The liquid source can be a low-melting point additive, eutectic formation in an elemental powder mix, a melt-depressant additive (such as boron), or simply the alloy itself when heated above solidus. Cambal and Lund [2.10] refer to the sintering of prealloyed powders above the solidus temperature of the alloy as supersolidus liquid-phase sintering (SLPS). Eventually, the liquid can persist throughout the whole sintering cycle or can be transient, depending on its stability and provenance.

LPS is widely used in industrial applications [2.11] since it permits fast sintering rates of coarse powders to full density. In contrast to the solid-state sintering process, LPS implies the co-existence of solid particles and liquid. In this semi-solid system, the liquid phase exerts a capillary force on the solid particles which can drive densification [2.12]. The capillary force was described by Hwang *et al.* [2.13] to be dependent on the particle size (diameter) and the wetting angle. Thus, small powder particles will sinter at higher rates during LPS since the capillary force is higher for finer particles. Alternatively, when the liquid volume fraction is large, rearrangement of the grains occur by grain-boundary sliding [2.12, 2.14]. In this case, the liquid phase lubricates the solid contacts and assists densification by rearrangement. Moreover, the diffusion rate is higher in liquids than in solids; therefore, densification by mass transport occurs at higher rates. Final densification in LPS with low liquid fraction occurs by solution reprecipitation, which involves solubility of the solid in the liquid phase, followed by solid precipitation at the neck region [2.12, 2.15].

2.4.3. Supersolidus liquid-phase sintering

SLPS is a variant of LPS in which prealloyed powder is partially melted when heated between its solidus and liquidus temperature. The amount of liquid formed depends on the temperature and can be estimated from the phase diagram of the alloy [2.16]. Since sintering is a non-equilibrium process, such an estimate is not representative of the true liquid fraction. However, thermal analysis by DSC can provide more accurate data about the liquid fraction evolution.

One characteristic of the SLPS process is that liquid formation starts within the powder particles. On the contrary, during LPS of mixed powders, the melt reaction begins at the surface of particles by either melting the low liquidus powder or a eutectic reaction. This characteristic of SLPS stems from the liquid source, which is the solute-rich interdendritic region in the rapidly solidified powder particles. Figure 2.3 presents the SLPS process sequence: (a) solid-state sintering; (b) liquid formation inside particles at grain boundaries and inside grains; (c) grain coarsening, sintering by viscous flow as the liquid wets the grain boundaries; and (d) final stage sintering with spherical pores.

This representation of SLPS assumes good wetting of the solid phase and is the basis for a phenomenological model proposed by German [2.16]. Densification in SLPS is mainly driven by the capillary force, which induces rearrangement of the grains by viscous flow. Experiments with cupronickel [2.17] have shown the liquid phase distribution in SLPS to follow the sketch presented in Figure 2.3. The liquid phase was present inside grains and at grain boundaries and also spread to particle contacts.

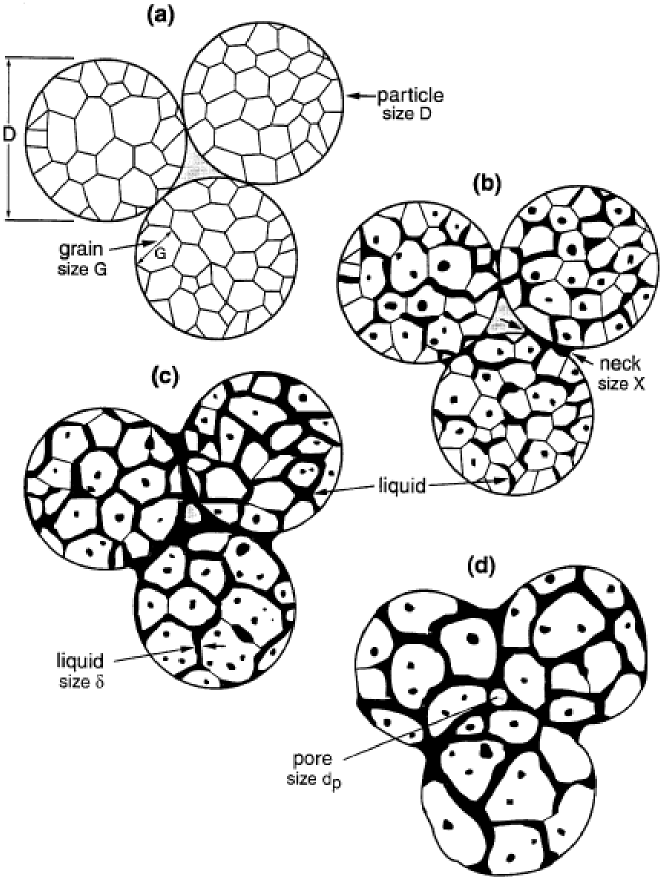

Figure 2-3: Diagram of the sintering sequence during SLPS (adapted from German [2.16])

2.4.3.1. Liquid film thickness

Liquid fraction, grain size, and dihedral angle determine the liquid film thickness at grain boundaries and particle contacts in a given semisolid alloy [2.18-2.19]. Figure 2.4 presents the fractional grain boundary coverage by liquid for different dihedral angles and liquid volume fractions along with experimental data for bronze [2.18].

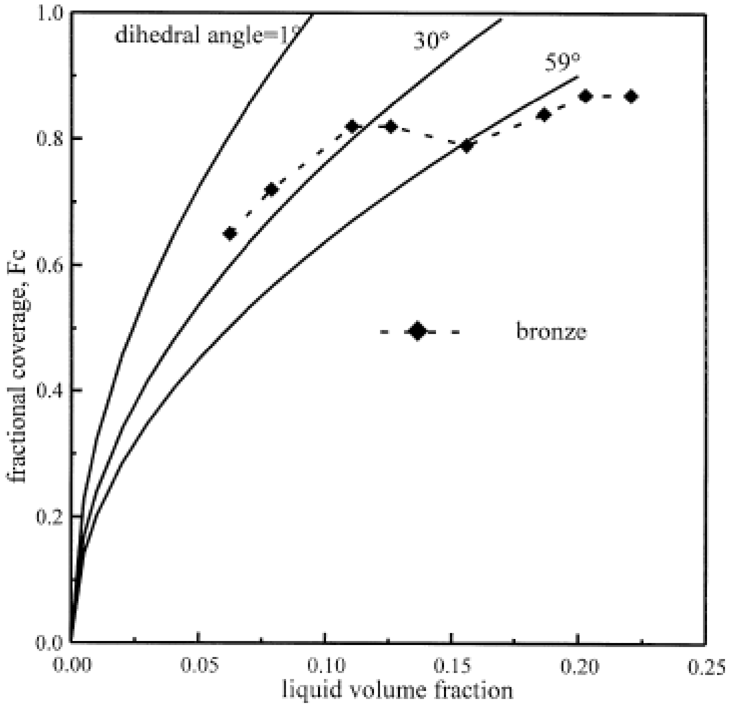

Figure 2-4: Fractional coverage as a function of liquid volume fraction and dihedral angle (adapted from Liu *et al.* [2.18])

As dihedral angles increase, there is less coverage of the grain boundaries, and the liquid film thus thickens. Equation 2.1 [2.20] relates the liquid film thickness to the grain size, volume fraction, and fractional grain boundary liquid coverage:

$$\delta(1 - C_{SS}) = \frac{G}{3}\frac{V_L}{(1 - V_L)}, \qquad \text{eq. 2.1}$$

where δ is the liquid film thickness, C_{SS} is the structural contiguity (i.e. the proportion of solid–solid interfaces in the structure), G is the grain size, and V_L is the liquid volume fraction. A critical liquid film thickness can initiate rapid densification by fragmentation [2.21]. This densification mechanism is unique to SLPS and is active when liquid nucleates at grain boundaries in sufficient amounts to allow grain-boundary sliding rearrangement under capillary force. The liquid film thickness is temperature dependant; therefore, a critical temperature exists over which the fragmentation densification mechanism occurs. In that context, evolution of the liquid fraction during heating of the compact is useful information, especially when using high heating rates.

2.4.3.2. Distortion during SLPS

The presence of liquid at grain boundaries and particle contacts reduces the rigidity of the powder compact and can lead to distortion [2.16, 2.22]. When the forces maintaining the compact shape cannot resist its own weight, shape loss occurs. Liu *et al*. [2.15] developed a model to predict the onset of distortion in SLPS as well as the onset of viscous flow [2.18]. The model is based on microstructure rigidity, defined as the contribution of solid–solid contact in addition to the liquid film viscous resistance. The solid–solid contact (R_{SS}) and liquid film viscous resistance (R_{SL}) are defined by equation 2.2 and 2.3:

$$R_{SS} = C_{SS}\sigma_{SS}, \qquad \text{eq. 2.2}$$

$$R_{SL} = \frac{\eta_L v A^2}{\delta^3}, \qquad \text{eq. 2.3}$$

where σ_{SS} is the contact strength, η_L is the liquid viscosity, A is the grain face area, and v is the relative velocity of the sliding grains. Resistance of the liquid film to viscous flow is inversely proportional to the cube of liquid film thickness, which implies a strong resistance for very thin films and a rapid decrease of resistance as liquid films thicken. Equations 2.2 and 2.3 can be combined into the total bond strength of the compact as shown in equation 2.4:

$$F_{bond} = \pi G^2 C_{SS}\sigma_{SS} + \frac{\alpha\eta_L \pi G^4 (1 - C_{SS})^2}{\delta^3}, \qquad \text{eq. 2.4}$$

where πG^2 is the total grain interface area in the compact and α is a constant with units of velocity. Equation 2.4 considers the area of solid liquid interface (A) to be proportional to $\pi G^2(1-C_{SS})$, and the constant of proportionality is included in the constant α.

Distortion can be predicted if the shear component of the gravitational force acting on the compact is known to exceed the grains bonding strength. Similarly the onset of sintering is predicted when the capillary force exceeds the grains bonding strength. In the first case, the gravitational shear stress acting on the compact bottom grains can be expressed by equation 2.5:

$$\tau_{grav} = \frac{\rho g h}{2}, \qquad \text{eq. 2.5}$$

where τ_{grav} is the shear stress due to gravity, ρ is the materials density, g is the gravitational constant and h is the height of the compact. Using equations 2.4 and 2.5, the onset of distortion is expressed as

$$\tau_{grav} \geq \sigma_{SS} C_{SS} + \frac{\alpha \eta_L G^2 (1 - C_{SS})^2}{\delta^3}, \qquad \text{eq. 2.6}$$

where the distortion is expected when the external force is greater than the solid contact resistance and viscous resistance of the liquid responsible for the semisolid structure rigidity. Substitution of equation 2.1 in 2.6 and rearranging the equation to isolate grain size and liquid fraction on the left hand side and structure parameters and constant on the right hand side yields equation 2.7:

$$\frac{G^{1/3} V_L}{3 V_S} \geq \left(\frac{\alpha \eta_L}{\sigma_{SS}} \right)^{1/3} \frac{(1 - C_{SS})^{5/3}}{\left(\tau / \sigma_{SS} - C_{SS} \right)^{1/3}}, \qquad \text{eq. 2.7}$$

where the left hand side may be defined as the softening parameter $\zeta = \frac{G^{1/3} V_L}{3 V_S}$. The softening parameter is readily obtained when the liquid volume fraction and the grain size of the compact are known. The liquid volume fraction can be predicted by thermodynamic calculations and validated by thermal analysis experiments and the grain size can be modeled using standard isothermal grain growth relationship as shown in equation 2.8

$$G - G_0 = k t^n, \qquad \text{eq. 2.8}$$

where G is the grain size, G_0 is the initial grain size at the beginning of the isothermal hold, k is a temperature dependant kinetic constant, t is time and n is the time exponent.

Liquid film thickness has been shown to be affected by dihedral angle such that low angles favor wetting of the grain boundaries and low film thickness. The prime advantage of SLPS lies in the low dihedral angle of the liquid phase compared with LPS systems. Consequently, the low liquid film thickness in SLPS favors higher compact strength than LPS for a given liquid fraction.

Finally, grain coarsening affects the liquid thickness by reducing grain boundary surface area. Therefore, a fixed volume of liquid is distributed on fewer grain boundaries, and the film thickness thus increases. Long holding times promote grain coarsening and can induce distortion.

2.4.4. Pressure-assisted sintering

Pressure-assisted sintering is used to sinter heat resistant materials to full density. External pressure lowers the sintering temperature needed for complete densification. Moreover, when sintering under pressure (i.e., hot isostatic pressing, hot pressing), rearrangement of particles initially occurs through plastic deformation and creep (i.e., viscous flow). In low density compacts, the particle contact points are small and the applied pressure is amplified. The densification of a powder compact under external pressure is expressed in equation 2.9 [2.23]:

$$\frac{d\phi}{dt} = \frac{1-\phi}{1-\phi_0} B\left(\frac{g\gamma_{SV}}{G} + P_E - P_G\right), \qquad \text{eq. 2.9}$$

where ϕ is density, ϕ_0 is green density, t is time, B is a thermally activated parameter function of the mass transport mechanism, g is a geometrical parameter, γ_{SV} is the solid–vapor interface energy, G is the grain size, P_E is the effective external pressure, and P_G is the gas pressure in the pores. The parenthesis in the right-hand side term of equation 2.9 includes the pressure effects of three components: sintering stress due to the elimination of pores, effective stress applied by external pressure, and pressure from the gas trapped in the pores. The sintering stress term is negligible (<1 MPa) [2.23] when compared to the effective stress, which is the main driving force for densification. Of course, gas filled pores are more difficult to eliminate; therefore, sintering under vacuum to reduce the pore pressure is advantageous.

The particle contact size changes with density as the necks grow. Amplification of the applied pressure is directly related to the particle contact area. Therefore, the effective pressure P_E relates to fractional density through equation 2.10 [2.24]:

$$\left(\frac{P_E}{P_A}\right)=\frac{1-\phi_0}{\phi^2(\phi-\phi_0)}, \qquad \text{eq. 2.10}$$

where P_A is the applied pressure. As density increases, the effective pressure decreases toward the applied pressure value. The very high effective pressure acting on the particle contacts in the initial stage of sintering permits plastic deformation of the particle contact area. The contact flattening continues until the effective stress falls below the yield strength of the powder at the process temperature.

Pressure induces creep when the stress at particle contacts decreases below the yield strength of the powder. At low homologous temperature and low stress, diffusion creep is active and referred to as Coble creep. Coble creep is characterized by grain-boundary diffusion, as the stress enhances mass transport and lattice diffusion is not activated at low temperatures. The net diffusion flux through grain boundaries is enhanced as the area fraction of grain boundaries increases. Small grain sizes are best suited to inducing high shrinkage rates in pressure-assisted sintering as the grain boundary surface increases according to $1/G^3$ [2.25]. Alternatively, at low stresses and high temperatures, the volume diffusion creep (i.e., Nabarro-Herring creep) mechanism is active [2.25]. Nabarro-Herring creep is less sensitive to grain size, and the shrinkage rate scales according to $1/G^2$. As is the case for volume diffusion, temperature is of prime importance to the mass flux and shrinkage is rapidly improved with temperature increases. Diffusive creep, like Coble and Nabarro-Herring creeps, contributes to the final elimination of pores by mass transport along a stress gradient from the neck (i.e., through compression) to the pore surface.

Dislocation creep occurs at high temperature and stress. Dislocations formed at high stress are responsible for grain shape changes. As dislocation motion is assisted by volume diffusion, the shrinkage rate is not influenced by grain size, but is dominated by pressure, followed by temperature.

2.4.5. Pressure-assisted supersolidus liquid-phase sintering

The presence of liquid at the grain interfaces improves densification under external pressure by reducing the strength of the grain boundary and increasing diffusion rates. According to German [2.23], densification of crystalline solids with grain boundary liquid is accomplished by viscous flow. The densification rate by viscous flow is directly proportional to the effective pressure P_E as shown in equation 2.11:

$$\frac{d\phi}{dt} = \frac{3P_E(1-\phi)}{4\eta(1-\phi_0)}, \qquad \text{eq. 2.11}$$

where η is the system viscosity. The difficulty in predicting densification during pressure-assisted liquid-phase sintering is the determination of the system viscosity, which is a function of temperature and pore fraction [2.16, 2.21]. The liquid phase assists grain rearrangement when an external pressure is applied during sintering.

2.4.6. Spark plasma sintering

Using pulsed direct current to heat powder under pressure induces rapid densification. The technique is commonly termed spark plasma sintering (SPS) because of the general belief that electric discharges are generated throughout voids in the powder compact. The attributed effects of this spark-generated plasma are thought to enhance neck formation and growth, eliminate oxides from powder particle surfaces, and activate sintering [2.26]. The aforementioned qualities have been cited without evidence [2.27] to explain two main experimental results: SPS allows sintering at lower temperatures and reduces the holding time to obtain full density.

The SPS process is similar to hot pressing (HP) with respect to the uniaxial pressure applied during sintering. Current flows through the die and powder bed proportional to their respective conductances. Accordingly, more current flows through the die in the early stage of sintering for conductive powders as the compact resistance is higher at low density [2.28].

The major difference between HP and SPS is the direct generation of heat in the powder bed (i.e., Joule heating) instead of radiation heat transfer from an electric furnace. This feature allows heating the powder at rates approaching 1000°C/min [2.29]. Rapid heating is the main advantage of SPS over conventional pressure-assisted techniques as it allows more surface energy from the pores to be carried to high temperature. Since grain boundary diffusion and volume diffusion are active at high temperatures, rapid heating minimizes surface diffusion and promotes high shrinkage rates. Moreover, rapid heating limits grain growth as shown in Figure 2.5. Moreover, Langer *et al.* were able to directly compare HP and SPS techniques to sinter ZnO [2.30], 8YSZ [2.31], and Al_2O_3 [2.32]; however, they did not find any advantages owing to the electric field.

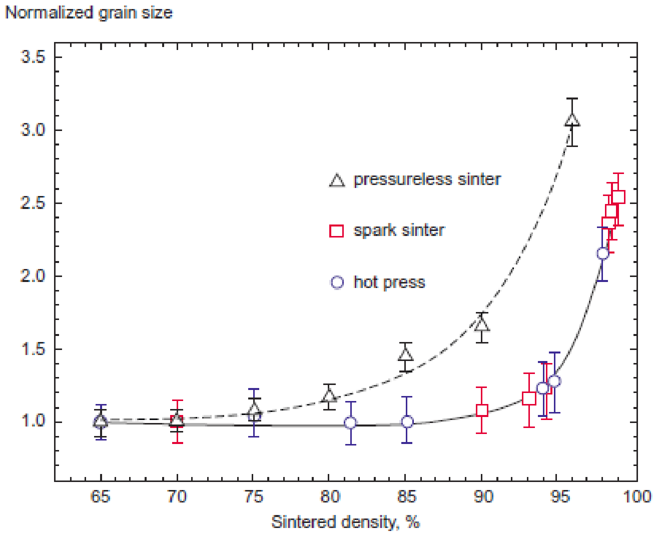

Figure 2-5: Comparison of the normalized grain size in alumina as a function of density obtained by pressureless sintering, HP, and SPS. Pressure-assisted sintering techniques produced finer grain size independent of the application of an electric field (adapted from German [2.23])

2.4.7. Sintering models

Prediction of the densification during sintering has been modeled by numerical methods based on phenomenological models such as the master sintering curve (MSC) introduced by Johnson *et* *al.* [2.33], the Riedel and Svoboda (RS) microstructure-based model [2.34-2.37], the continuum theory of sintering developed by Olevsky [2.38] based on prior work from Skorohod [2.39], and Kinetic Monte Carlo (KMC) simulations developed by Tikare [2.40-2.42]. Reiterer and Ewsuk [2.43] analysed the strengths and weaknesses of these four models and concluded that the choice of the appropriate model depends mainly on the data available and the information needed. This section reviews the attributes of the four mentioned models.

2.4.7.1. Master sintering curve model

The MSC is a phenomenological model derived from the combined-stage sintering model of Hansen *et al.* [2.44] where the linear shrinkage is given by equation 2.12:

$$\frac{d\rho}{3\rho dt} = \frac{\gamma\Omega(\Gamma(\rho))D_0}{kT(G[\rho])^n}\exp\left(-\frac{Q}{RT}\right), \qquad \text{eq. 2.12}$$

where ρ is the relative density, t is time, γ is the surface energy, Ω is the atomic volume, Γ is the lumped scaling parameter as described by Hansen *et al.* [2.44], D_0 is the appropriate diffusion constant (grain boundary or lattice diffusion), k is the Boltzman constant, T is the temperature, G is the grain size, n=3 for lattice diffusion and 4 for grain boundary diffusion, R is the gas constant and Q is the apparent activation energy of sintering.

The first assumption in the MSC model is that the lumped scaling parameter and the grain size are considered to be functions of density alone. Then, equation 2.12 can be reorganized and integrated as follows:

$$\frac{k}{\gamma\Omega D_0}\int_{\rho_0}^{\rho}\frac{(G(\rho))^n}{3\rho\Gamma(\rho)}d\rho = \int_0^t \frac{1}{T}\exp\left(-\frac{Q}{RT}\right)d \qquad \text{eq. 2.13}$$

where ρ_0 is the green density. Equation 2.13 is conveniently arranged to separate the material properties on the left hand side from the activation energy (sintering mechanism) and the temperature-time data on the right hand side. As such, equation 2.13 can be expressed as:

$$\Phi(\rho) = \Theta(t, T(t)) \qquad \text{eq. 2.14}$$

where *Φ(ρ)* includes all the material related parameters except for *Q*, and *Θ(t,T(t))* is the "thermal work" term that can be integrated by numerical methods from the temperature profiles of different sintering tests or from dilatometer curves. Once the apparent activation energy of sintering has been determined by curve fitting, a single function can be used to predict the density as a function of the thermal work.

Bollina *et al.* [2.45] adapted the MSC to SLPS by dividing the sintering into three stages, i.e. solid state, formation of liquid and liquid phase. Each stage has its own activation energy and the transition between each stage is performed by interpolation between the fitted curves as shown in Figure 2-6.

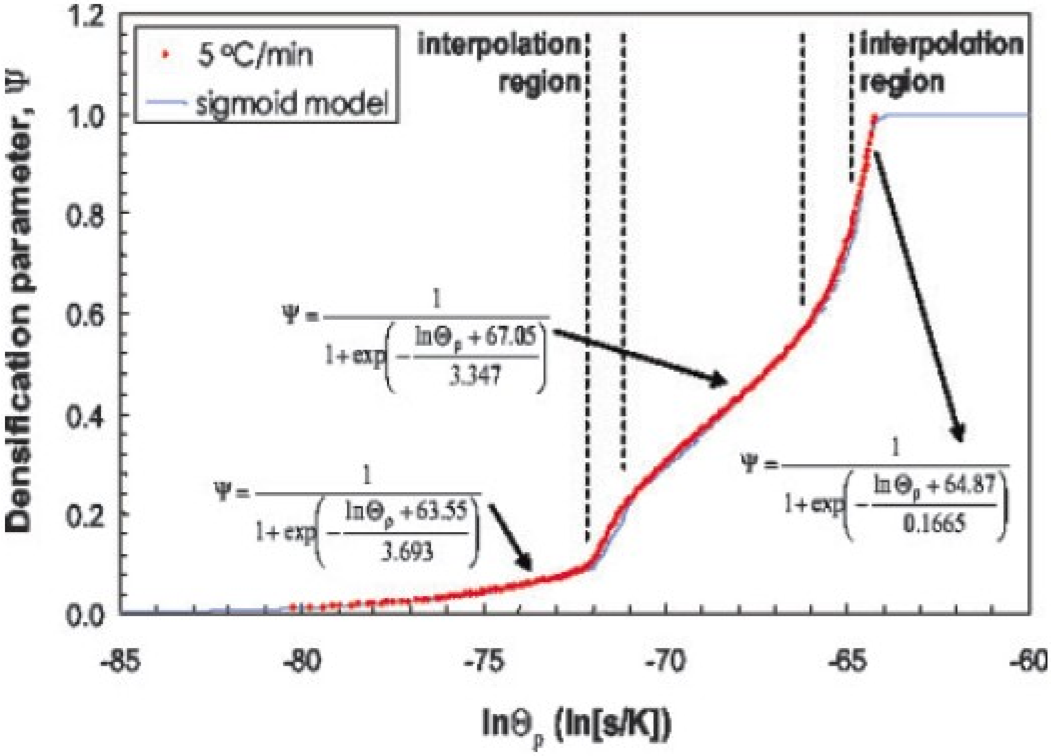

Figure 2-6 : Master sintering curve for boron doped 316L stainless steel powders sintered at 5 K/min showing the three curve fitting regions associated to solid state, liquid formation (over solidus temperature) and higher temperature SLPS. [2.45]

The MSC fitted by Bollina was based on 5 dilatometer curves and was used to predict sintering of boron doped stainless steel 316L water atomized powders.

2.4.7.2. Riedel Svoboda model

This model is based on the work of Ashby [2.46] for the sintering mechanisms and the work of Jagota and Dawson [2.47], and McMeeking and Kuhn [2.48] for the mechanical concepts. It proposes a constitutive equation where the strain rate tensor ($\dot{\varepsilon}_{ij}$) is related to the stress tensor (i.e. sintering stress and external stress) as expressed in equation 2.15:

$$\dot{\varepsilon}_{ij} = \frac{\sigma'_{ij}}{2G} + \delta_{ij}\frac{\sigma_m - \sigma_s + \Delta p}{3K}, \qquad \text{eq. 2.15}$$

where σ'_{ij} is the stress deviator, σ_m is the hydrostatic stress, σ_s is the sintering stress, Δp is the internal pressure of the pores, δ_{ij} is the Kronecker symbol, G and K are the shear and bulk viscosity.

This model was designed for solid state sintering and may take into account the effect of grain growth and mass transport mechanisms through modification of the viscous moduli G and K. Its advantage is the inclusion of external stress effect on the densification rate; however, the impact of partial melting during sintering is not included in the RS model.

2.4.7.3. Olevsky viscous flow model

The rheological theory of sintering put forward by Olevsky [2.38], based on the work of Skorohod [2.39], uses a similar constitutive equation as in the RS model (eq. 2.15) expressed as follow:

$$\dot{\varepsilon}_{ij} = \frac{\sigma'_{ij}}{2\overline{G}} + \delta_{ij}\frac{\sigma_m - \sigma_s}{3\overline{K}}, \qquad \text{eq. 2.16}$$

where $\overline{G}$ and $\overline{K}$ are the effective shear and bulk viscosity. The difference from the RS model is in the definition of these two parameters, which are dependent on the normalized viscosities φ and ψ, and on the temperature dependent shear viscosity of the fully dense solid phase (η_0) as shown in equations 2.17 and 2.18:

$$\overline{G} = \eta_0 \varphi$$ eq. 2.17

$$\overline{K} = 2\eta_0 \psi$$ eq. 2.18

In turn the normalized viscosities and sintering stress are related to relative density through equations 2.19 – 2.21:

$$\varphi = a_1 \rho^{b_1},$$ eq. 2.19

$$\psi = a_2 \frac{\rho^{b_2}}{(1-\rho)^{c_2}},$$ eq. 2.20

$$\sigma_s = a_3 \rho^{b_3} \frac{3\alpha}{r},$$ eq. 2.21

where *a*, *b*, *c* are fitting parameters, α is the surface energy and *r* is the grain (particle) radius. The values of parameters a_1, b_1, a_2, b_2, c_2, a_3 and b_3 were determined by Skorohod [2.39] originally based on continuum mechanics and further refined by Olevsky *et al.* [2.41] and by Arguello *et al.* [2.49] through KMC simulations as shown in Table 2-2:

Table 2-2 : Parameters developed for the SOVS model

Parameter	a_1	b_1	a_2	b_2	c_2	a_3	b_3
Skorohod [2.39]	1	2	2/3	3	1	1	2
Olevsky *et al.* [2.41]	-	-	2/3	2.26	1.12	1.7	0.26
Arguello *et al.* [2.49]	1.12	1.26	-	-	-	-	-

Finally the shear viscosity function was derived by the following Arrhenius type equation:

$$\eta_0(T) = A_1 T \exp\left(\frac{Q_{SOVS}}{RT}\right),$$ eq. 2.22

where A_1 is a fitting parameter, R is the gas constant and Q_{SOVS} is the apparent activation energy for material flow (creep).

The SOVS model is based on continuum mechanics and takes into account the external pressure effect and the rigidity of the solid skeleton through the effective viscosity parameters. The main challenge in the application of SOVS model to SLPS is to define realistic viscosity behavior upon formation of liquid phase, which has never been addressed to the author's knowledge.

2.4.7.4. Kinetic Monte Carlo model

The model developed by Tikare [2.40], Braginsky [2.42] and Olevsky [2.41] is based on the prediction of microstructure evolution during solid state sintering since the microstructure changes are driving the mechanical response of the system. Thus, the Kinetic Monte Carlo model is used to simulate the evolution of grain size, shape and packing along with the evolution of pore size shape and distribution. The microstructure evolution is used to determine the sintering stress, i.e. the sintering driving force.

The model is able to simulate the process of grain growth by short range diffusion, diffusion of pores, diffusion of vacancies and material and annihilation of vacancies at grain boundaries. To begin with, a square lattice is populated with grain sites and pore sites. The grains are allowed to take individual states q, where q_{grains} = [1,2,…,Q]; and the pores all have the same state q_{pore} = -1. Contiguous pore sites have the same state, therefore there are no pore boundaries; however, contiguous grains site that have different state, q, generate a grain boundary interface, while neighboring grain sites of the same state form a grain. The difference between the pore site state and the grain site state also generates a pore/grain boundary. Isolated pore sites are considered as vacancies.

The energy of the system (equation 2.23) is defined as the amount of boundaries existing in the lattice such that reduction of the system energy is driving grain growth.

$$E = \frac{1}{2}\sum_{i=1}^{N}\sum_{j=1}^{8}\left(1-\delta\left(q_i, q_j\right)\right), \qquad \text{eq. 2.23}$$

where N is the total number of sites, $\delta(q_i,q_j)$ is the Kronecker delta with $\delta(q_i = q_j) = 1$ and $\delta(q_i \neq q_j) = 0$, q_i is the state of the grain or pore at site I, and q_j is the state of the nearest neighbor at site j.

Grain growth is simulated by assigning temporarily a new state to a random grain site in the lattice and the evaluation of the change in energy is computed using equation 2.23. The standard Metropolis algorithm is then used to perform the grain growth step. A random number is generated between 0 and 1 and compared to the transition probability P:

$$P = \begin{cases} \exp\left(\dfrac{-\Delta E}{k_B T}\right) & \forall\, \Delta E > 0 \\ 1 \quad \forall\, \Delta E \leq 0 \end{cases} \qquad \text{eq. 2.24}$$

where k_B is the Boltzmann constant and T is the temperature. If the randaom number, $R \leq$ P, then the grain growth step remains, otherwise the grain site state is restored to its original state. The same procedure is used for pore migration, where a pore site and a neighboring grain site are randomly chosen and exchanged; with the grain site state changed to a new state q that minimizes energy. Thus, surface diffusion driven pore migration is simulated by this exchange, the change in energy is computed using equation 2.23, and the Metropolis algorithm is used to perform the pore migration step using equation 2.24 to determine the transition probability. Further, vacancy annihilation can be simulated by exchanging a vacancy at a grain boundary with a grain site on the outside boundary of the compact that is directly in line with the center of mass of the adjacent grain and the vacancy as seen in Figure 2-7.

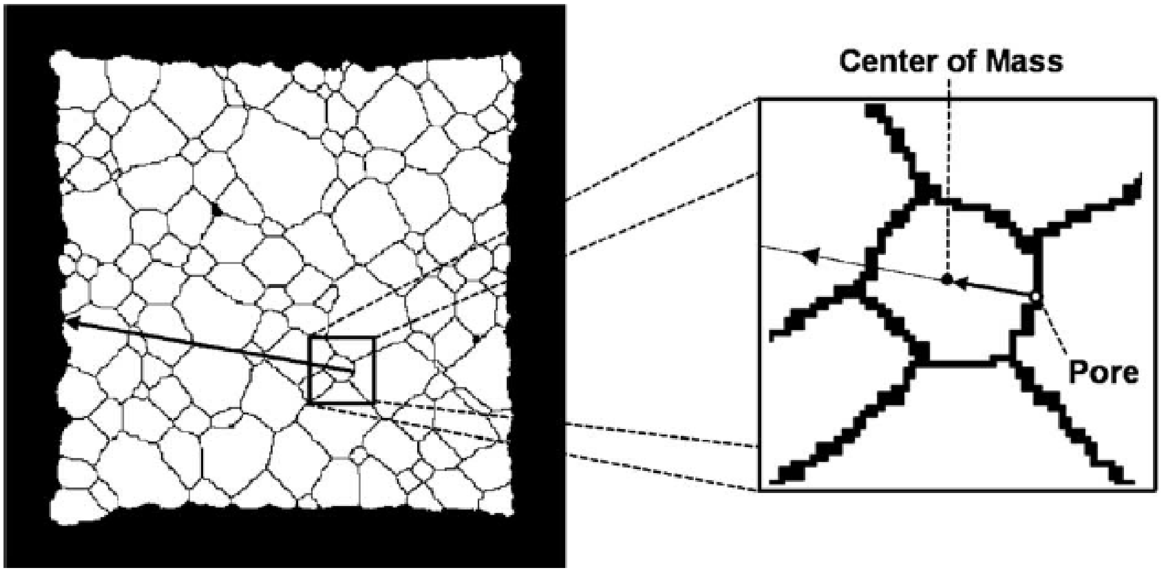

Figure 2-7 : Illustration of the algorithm proposed by Braginsky to annihilate vacancy at grain boundaries (black lines) [2.42]

Since the model is based on Monte Carlo simulation, the time, temperature and space are all in the Monte Carlo scale and has to be fitted to experimental data. The model is powerful because it includes microstructure evolution; however, in its current state, it applies only to solid state sintering. The advancement of this model to liquid phase sintering would be very complex because of the additional phase forming while heating and multiple interactions between solid, liquid and pores. Thus, in its current state this model is not suited to the modeling of Inconel 718 sintering process.

2.5. COLD GAS DYNAMIC SPRAY

The cold gas dynamic spray (CGDS) process is a powder deposition technique that relies on the kinetic energy transmitted from a supersonic gas stream to a particle in order to ensure formation of a splat and its adhesion to a substrate [2.50]. Figure 2-8 presents a schematic of the process.

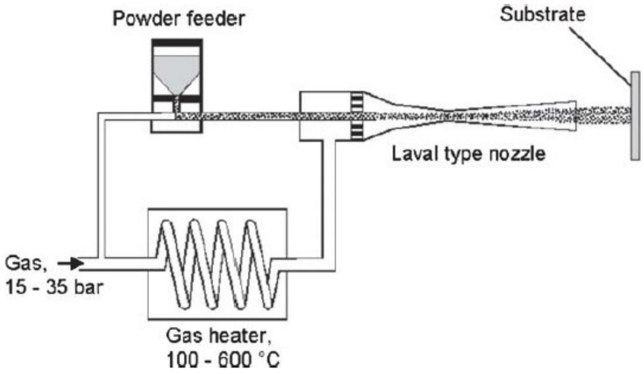

Figure 2-8: Schematic representation of CGDS process (adapted from Gärtner *et al.* [2.51])

The powder is carried by a supersonic gas jet through a de Laval nozzle able to accelerate the particle to high velocities in excess of Mach 2 (680 m/s). High-pressure spray gas, typically nitrogen or helium, flows through a gas or electric heater and is then accelerated to supersonic velocity by the convergent-divergent nozzle.

The gas transfers heat and kinetic energy to the powder particles, which bond to the substrate upon impact. A high plastic deformation rate, termed adiabatic shear instability, is responsible for the intersplat bonding and substrate adhesion. The process has been modeled by Assadi *et al.* [2.52], who found that the adiabatic shear instabilities only occur on a small proportion of the particle surface and such applications result in poor mechanical properties for copper deposits. Investigations into the conditions for adhesion of different material powder have determined the empirical critical velocity over which coating build up was observed [2.53-2.55].

The principal advantage of CDGS over other thermal spray techniques, such as plasma spray and high velocity oxy fuel (HVOF), is the limited powder temperature required for bonding. Low temperature gas streams and even lower temperature powders limit oxidation to less than that typical of other high temperature spray processes [2.51-2.52, 2.56]. On the other hand, CGDS of

Inconel 718 was found to lack adherence when compared to HVOF of the same feedstock [2.56] thus requiring process optimization and potentially requiring post-heat treatment.

2.6. SINTERING OF INCONEL 718

2.6.1. Pressureless sintering of slip cast and metal injection molded parts

Early Inconel 718 sintering investigations were conducted by pressureless sintering of slip cast powder compacts. Experiments by Hajmrle *et al.* [2.57] provide a densification curve in relation to temperature, as seen in Figure 2-9.

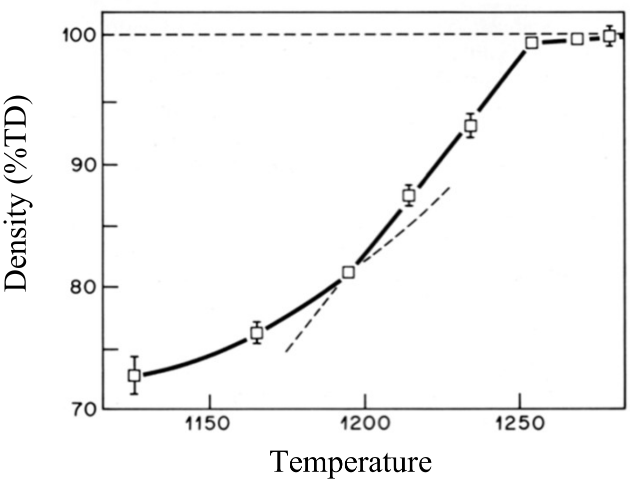

Figure 2-9: Pressureless sintering density as a function of sintering temperature for 5-h holding cycles (adapted from Hajmrle *et al.* [2.57])

Sintering Inconel 718 under vacuum ($6.7\text{x}10^{-4}$–$13\text{x}10^{-4}$ Pa) at temperatures ranging from 1100°C to 1277°C and holding times between 3 and 32 h yielded several conclusions concerning the densification mechanism, grain growth, and phase formation of the sintered powder. For 5-h sintering runs, the highest density (~100%) is obtained at a temperature of 1277°C, and Hajmrle *et al.* [2.57] did not report distortion issues. An inflection of the density curve occurs just below 1200°C and was attributed to the onset of the liquid-phase sintering mechanism without further microstructural evidence. Grain size was subsequently found to increase rapidly at 1230°C, which was related to the elimination of pore pinning [2.58]. Formation of acicular δ phase was observed at sintering temperatures exceeding 1190°C and Nb- and Ti-rich phases were formed at sintering temperatures exceeding 1230°C. MC carbides and γ′/γ″ were observed at all temperatures between 1120°C and 1270°C. MC carbides were mostly Nb and Ti carbides. Hajmrle *et al.* [2.59] later noted losses of Cr upon sintering in high vacuum above 1190°C.

Further studies have been conducted with metal injection molded (MIM) Inconel 718 components [2.60-2.65]. Sintering of Inconel 718 MIM parts was shown to yield high densities (97.2%–98.7%) with fine grain sizes (15–30 µm) using temperatures between 1260°C and 1300°C. However, HIP post-treatment was mandatory to obtain the mechanical properties specified within the AMS 5662 standard [2.66]. Residual porosity was completely eliminated (99.7% density) by HIP treatment without grain size coarsening [2.60].

2.6.2. Direct Hot Isostatic Pressing

Consolidation by direct HIPing uses a high temperature, high pressure gas to press a powder-filled container as shown in Figure 2-10. The main advantage of this process is the ability to sinter complex shapes under pressure. However, the container design is challenging and requires finite element modelling of distortion during the process in order to achieve near-net-shape parts. The combination of high temperature and high pressure yields full density [2.67].

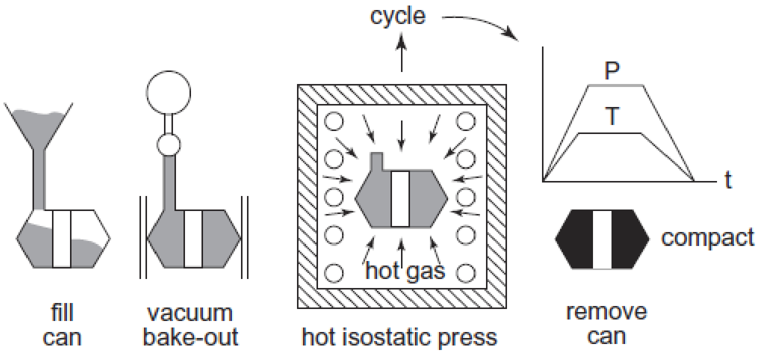

Figure 2-10: Hot isostatic pressing process for consolidation of powder metallurgy parts (adapted from German [2.23])

Investigations of the consolidation, microstructure, and properties of direct HIPed Inconel 718 have been performed by Rao *et al.* [2.68-2.71]. Direct HIP Inconel 718 was reported to be fully dense; however, the mechanical properties did not achieve AMS 5662 specifications [2.68]. The as-HIPed microstructure presented prior particle boundary (PPB) carbides, which were identified as failure initiation regions on a fracture surface. Though the mechanical properties obtained by direct HIP are very close to the specified wrought values, the elimination of PPB carbides has the potential to further increase the performance of Inconel 718 produced by direct HIP.

2.6.3. Prior Particle Boundaries

The main challenge in direct HIP P/M processing of Inconel 718 (and other superalloys) is the formation of MC carbide decorated PPBs [2.67]. This boundary inhibits grain growth beyond the PPB and reduces particle cohesion. Thus, PPBs are predictable crack initiation sites responsible for the low yield strength reported for direct HIP Inconel 718 [2.68]. One method to reduce PPB carbide formation is to decrease the carbon content in the powder and add strong carbide formers, such as tantalum or hafnium, to allow carbide formation to take place within particles [2.67]. Otherwise, a proper combination of HIP and heat treatment can be used to eliminate or transform the MC carbides at the particles surface [2.69-2.70].

PPBs are caused by atomic segregation and oxygen surface contamination [2.72]. Oxides formed on the surface of particles during atomization are suitable sites for the nucleation of MC carbides [2.73]. Specifically, the elements with high oxygen affinity (e.g., Al and Ti) will react with oxygen adsorbed on the surface or present in the process. Rao *et al.* observed fine Al and Ti oxide particles (30–100 nm) on which MC carbides (M is Nb and Ti) had formed (100–500 nm) during the HIP consolidation of Inconel 718 at 1200°C. The PPBs did not allow for particle deformation during HIPing, and the final equiaxed structure was not obtained [2.68]. Moreover, they observed both γ'' and some γ' precipitates, which could only precipitate during the slow cooling stage of the HIP cycle. The precipitates were very fine (10 nm long and 4 nm thick for γ'' disks), which was attributed to the high homogeneity of the material [2.68].

PPBs of direct HIPed parts can be dissolved by heat treatments exceeding 1250°C [2.69]. The ductility for the solution-treated Inconel 718 direct HIP part was high but diminished after aging. However, ductility of aged Inconel 718 direct HIP parts remained higher when the solution treatment was above 1250°C, even if incipient melting was observed. Fractography of the material showed a crack propagation transition from intergranular to transgranular when the solution temperature surpassed 1250°C. Both ductility and stress rupture life improvement have been related to the disruption of PPB networks and better consolidation of the particles [2.69].

Finally, oxygen content in the powder was found to be an important parameter controlling the amount and distribution of PPBs formed during sintering [2.71]. The oxygen content was inversely proportional to particle size, since small particles have more surface area available for oxidation during gas atomization and subsequent handling. Inconel 718 powder particles containing 140 ppm oxygen did not exhibit MC carbides at PPBs; the carbides were uniformly distributed within the matrix instead. Additionally, oxygen content was found to change the recrystallization and twinning behavior of the HIPed material as seen in Figure 2-11. HIPed and heat treated Inconel 718 produced with 275 ppm, 180 ppm, and 140 ppm oxygen powders yielded alloys with ductilities of 2.1%, 4.5%, and 6%, respectively, at 650°C [2.71].

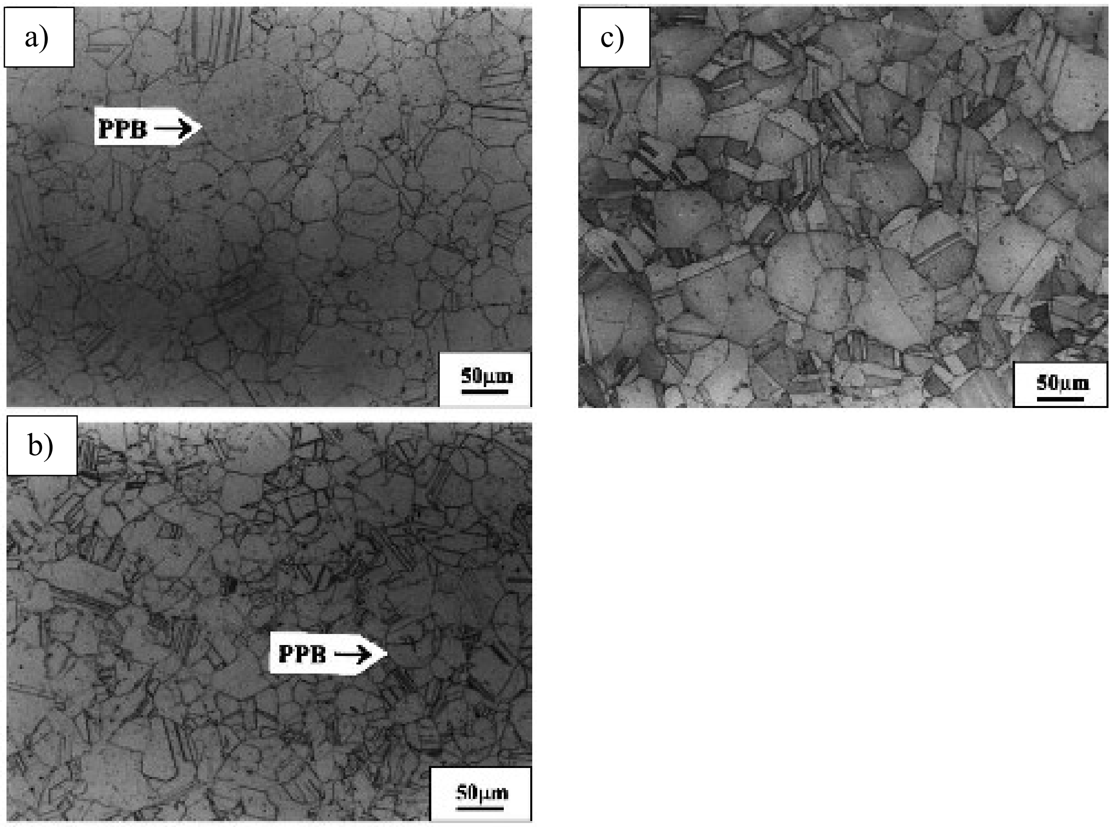

Figure 2-11: Electron micrograph of HIPed structures (a)275 ppm O2 (b)180 ppm O2, and (c)140 ppm O2 (adapted from Rao et al. [2.71])

2.7. REFERENCES

2.1. Donachie, M.J. and S.J. Donachie, *Superalloys : a technical guide*. 2nd ed. 2002, Materials Park, OH: ASM International, 439 p.
2.2. Reed, R.C., *The superalloys : fundamentals and applications*. 2006, Cambridge, UK; New York: Cambridge University Press.
2.3. Bradley, E.F., *Superalloys : a technical guide*. 1988, Metals Park, OH: ASM International. 280 p.
2.4. Paulonis, D.F., J.M. Oblak, and D.S. Duvall, *Precipitation in Nickel-Base Alloy 718.* Asm Transactions Quarterly, 1969. **62**(3): p. 611-622.
2.5. Azadian, S., L.Y. Wei, and R. Warren, *Delta phase precipitation in Inconel 718.* Materials Characterization, 2004. **53**(1): p. 7-16.
2.6. Sundararaman, M., P. Mukhopadhyay, and S. Banerjee, *Some Aspects of the Precipitation of Metastable Intermetallic Phases in Inconel-718.* Metallurgical Transactions a-Physical Metallurgy and Materials Science, 1992. **23**(7): p. 2015-2028.

2.7. Cozar, R. and A. Pineau, *Morphology of Y' and Y'' Precipitates and Thermal-Stability of Inconel 718 Type Alloys.* Metallurgical Transactions, 1973. **4**(1): p. 47-59.

2.8. Boesch, W. and H. Canada, *Precipitation Reactions and Stability of Ni 3 Cb in Inconel Alloy 718.* J METALS, 1969. **21**(10): p. 34-38.

2.9. German, R.M., *Sintering theory and practice.* Sintering Theory and Practice, by Randall M. German, pp. 568. ISBN 0-471-05786-X. Wiley-VCH, January 1996., 1996. **1**.

2.10. Cambal, L. and J. Lund, *Supersolidus sintering of loose steel powders.* Int J Powder Metall, 1972. **8**(3): p. 131-140.

2.11. German, R.M., P. Suri, and S.J. Park, *Review: liquid phase sintering.* Journal of Materials Science, 2009. **44**(1): p. 1-39.

2.12. Kingery, W., *Densification during sintering in the presence of a liquid phase. I. Theory.* Journal of Applied Physics, 1959. **30**(3): p. 301-306.

2.13. Hwang, K., R. German, and F. Lenel, *Capillary forces between spheres during agglomeration and liquid phase sintering.* Metallurgical Transactions A, 1987. **18**(1): p. 11-17.

2.14. Huppmann, W., et al., *ELEMENTARY MECHANISMS OF LIQUID-PHASE SINTERING. 1. REARRANGEMENT.* Zeitschrift fur Metallkunde, 1979. **70**(11): p. 707-713.

2.15. Mortensen, A., *Kinetics of densification by solution-reprecipitation.* Acta Materialia, 1997. **45**(2): p. 749-758.

2.16. German, R.M., *Supersolidus liquid-phase sintering of prealloyed powders.* Metallurgical and materials transactions A, 1997. **28**(7): p. 1553-1567.

2.17. Lund, J. and S.R. Bala, *Supersolidus sintering*, in *Modern developments in powder metallurgy. Vol. 6*. 1974.

2.18. Liu, J., A. Lal, and R. German, *Densification and shape retention in supersolidus liquid phase sintering.* Acta Materialia, 1999. **47**(18): p. 4615-4626.

2.19. Tandon, R., *Densification mechanisms and microstructural evolution leading to high density processing of prealloyed powders in supersolidus liquid phase sintering*. 1995, The Pennsylvania State University: Ann Arbor. p. 204-204 p.

2.20. Liu, J., A. Lal, and R.M. German, *Densification and shape retention in supersolidus liquid phase sintering.* Acta Materialia, 1999. **47**(18): p. 4615-4626.

2.21. Lal, A., *Mechanisms and mechanics of shape loss during supersolidus liquid-phase sintering*. 1999, The Pennsylvania State University: Ann Arbor. p. 252-252 p.

2.22. Wright, C., et al., *Supersolidus Sintering of High Speed Steels: Part 2: Sintering of Tungsten Based Alloys.* Powder metallurgy, 1995. **38**(3): p. 221-229.

2.23. German, R.M., *Chapter Ten - Sintering With External Pressure*, in *Sintering: from Empirical Observations to Scientific Principles*, R.M. German, Editor. 2014, Butterworth-Heinemann: Boston. p. 305-354.

2.24. Helle, A.S., K.E. Easterling, and M.F. Ashby, *Hot-isostatic pressing diagrams: New developments.* Acta Metallurgica, 1985. **33**(12): p. 2163-2174.

2.25. Frost, H.J. and M.F. Ashby, *Deformation mechanism maps: the plasticity and creep of metals and ceramics.* 1982.

2.26. Tokita, M. *Mechanism of spark plasma sintering*. in *Proceeding of NEDO International Symposium on Functionally Graded Materials*. 1999: Japan.

2.27. Hulbert, D.M., et al., *A discussion on the absence of plasma in spark plasma sintering.* Scripta Materialia, 2009. **60**(10): p. 835-838.

2.28. Anselmi-Tamburini, U., et al., *Fundamental investigations on the spark plasma sintering/synthesis process: II. Modeling of current and temperature distributions.* Materials Science and Engineering: A, 2005. **394**(1): p. 139-148.
2.29. Ye, J., L. Ajdelsztajn, and J.M. Schoenung, *Bulk nanocrystalline aluminum 5083 alloy fabricated by a novel technique: Cryomilling and spark plasma sintering.* Metallurgical and materials transactions A, 2006. **37**(8): p. 2569-2579.
2.30. Langer, J., M.J. Hoffmann, and O. Guillon, *Electric Field-Assisted Sintering and Hot Pressing of Semiconductive Zinc Oxide: A Comparative Study.* Journal of the American Ceramic Society, 2011. **94**(8): p. 2344-2353.
2.31. Langer, J., M.J. Hoffmann, and O. Guillon, *Electric Field-Assisted Sintering in Comparison with the Hot Pressing of Yttria-Stabilized Zirconia.* Journal of the American Ceramic Society, 2011. **94**(1): p. 24-31.
2.32. Langer, J., M.J. Hoffmann, and O. Guillon, *Direct comparison between hot pressing and electric field-assisted sintering of submicron alumina.* Acta Materialia, 2009. **57**(18): p. 5454-5465.
2.33. Su, H. and D.L. Johnson, *Master sintering curve: a practical approach to sintering.* Journal of the American Ceramic Society, 1996. **79**(12): p. 3211-3217.
2.34. Riedel, H. and J. Svoboda, *A theoretical study of grain growth in porous solids during sintering.* Acta metallurgica et materialia, 1993. **41**(6): p. 1929-1936.
2.35. Svoboda, J., H. Riedel, and H. Zipse, *Equilibrium pore surfaces, sintering stresses and constitutive equations for the intermediate and late stages of sintering—I. Computation of equilibrium surfaces.* Acta metallurgica et materialia, 1994. **42**(2): p. 435-443.
2.36. Riedel, H., H. Zipse, and J. Svoboda, *Equilibrium pore surfaces, sintering stresses and constitutive equations for the intermediate and late stages of sintering—II. Diffusional densification and creep.* Acta metallurgica et materialia, 1994. **42**(2): p. 445-452.
2.37. Riedel, H., V. Kozak, and J. Svoboda, *Densification and creep in the final stage of sintering.* Acta metallurgica et materialia, 1994. **42**(9): p. 3093-3103.
2.38. Olevsky, E.A., *Theory of sintering: from discrete to continuum.* Materials Science and Engineering: R: Reports, 1998. **23**(2): p. 41-100.
2.39. Skorohod, V., *Rheological basis of the theory of sintering.* Naukova Dumka, Kiev, 1972.
2.40. Tikare, V., M. Braginsky, and E.A. Olevsky, *Numerical Simulation of Solid-State Sintering: I, Sintering of Three Particles.* Journal of the American Ceramic Society, 2003. **86**(1): p. 49-53.
2.41. Olevsky, E.A., V. Tikare, and T. Garino, *Multi-Scale Study of Sintering: A Review.* Journal of the American Ceramic Society, 2006. **89**(6): p. 1914-1922.
2.42. Braginsky, M., V. Tikare, and E. Olevsky, *Numerical simulation of solid state sintering.* International journal of solids and structures, 2005. **42**(2): p. 621-636.
2.43. Reiterer, M.W. and K.G. Ewsuk, *An analysis of four different approaches to predict and control sintering.* Journal of the American Ceramic Society, 2009. **92**(7): p. 1419-1427.
2.44. Hansen, J.D., et al., *Combined-Stage Sintering Model.* Journal of the American Ceramic Society, 1992. **75**(5): p. 1129-1135.
2.45. Bollina, R., S. Park, and R.M. German, *Master sintering curve concepts applied to full-density supersolidus liquid phase sintering of 316L stainless steel powder.* Powder Metallurgy, 2010. **53**(1): p. 20-26.
2.46. Ashby, M., *A first report on sintering diagrams.* Acta Metallurgica, 1974. **22**(3): p. 275-289.

2.47. Jagota, A. and P. Dawson, *Micromechanical modeling of powder compacts—I. Unit problems for sintering and traction induced deformation.* Acta Metallurgica, 1988. **36**(9): p. 2551-2561.

2.48. McMeeking, R. and L. Kuhn, *A diffusional creep law for powder compacts.* Acta metallurgica et materialia, 1992. **40**(5): p. 961-969.

2.49. Argüello, J.G., M.W. Reiterer, and K.G. Ewsuk, *Verification, Performance, Validation, and Modifications to the SOVS Continuum Constitutive Model in a Nonlinear Large-Deformation Finite Element Code.* Journal of the American Ceramic Society, 2009. **92**(7): p. 1442-1449.

2.50. Van Steenkiste, T., et al., *Kinetic spray coatings.* Surface and coatings technology, 1999. **111**(1): p. 62-71.

2.51. Gärtner, F., et al., *The cold spray process and its potential for industrial applications.* Journal of Thermal Spray Technology, 2006. **15**(2): p. 223-232.

2.52. Assadi, H., et al., *Bonding mechanism in cold gas spraying.* Acta Materialia, 2003. **51**(15): p. 4379-4394.

2.53. Stoltenhoff, T., H. Kreye, and H. Richter, *An analysis of the cold spray process and its coatings.* Journal of Thermal Spray Technology, 2002. **11**(4): p. 542-550.

2.54. Papyrin, A., *Cold spray technology.* Advanced materials & processes, 2001. **159**(9): p. 49-51.

2.55. McCune, R., et al., *An Exploration of the Cold Gas-Dynamic Spray Method for Several Materials Systems.* Advances in Thermal Spray Science and Technology, 1995: p. 1-5.

2.56. Marrocco, T., D.G. McCartney, and P.H. Shipway, *Comparison of the microstructure of Cold Sprayed and Thermally Sprayed IN718 Coatings*, in *International thermal Spray Conference*. 2006, ASM International: Seattle.

2.57. Hajmrle, K. and R. Angers, *Sintering of Inconel 718.* International Journal of Powder Metallurgy, 1980. **16**(3): p. 255-266.

2.58. Angers, R. and K. Hajmrle, *Grain growth during sintering of a nickel-base superalloy.* Scripta Metallurgica, 1980. **14**(6): p. 577-581.

2.59. Hajmrle, K., R. Angers, and G. Dufour, *Phase analysis of sintered and heat treated alloy 718.* Metallurgical Transactions A, 1982. **- 13 A**(1): p.5 - 12.

2.60. Valencia, J.J., J. Spirko, and R. Schmees, *Sintering effect on the microstructure and mechanical properties of alloy 718 processed by powder injection molding.* Superalloys 718, 625, 706 and Various Derivatives, 1997: p. 753-762.

2.61. Wohlfromm, H., et al., *Metal Injection Moulding of Nickel-based Superalloys for High Temperature Applications.* Proceedings Euro PM2003 Congr. Exhib., 2003. **3**: p. 207-215.

2.62. Youhua, H., et al., *Preparation and Mechanical Properties of Inconel718 Alloy by Metal Injection Molding.* Rare Metal Materials and Engineering, 2010. **39**(5): p. 775-780.

2.63. Schmees, R., J.R. Spirko, and J. Valencia. *Powder injection molding (PIM) of Inconel 718 aerospace components*. in *Proceedings of the Advanced Particulate Materials & Processes*. 1997.

2.64. Özgün, O., et al., *Microstructural and mechanical characterization of injection molded 718 superalloy powders.* Journal of Alloys and Compounds, 2013. **576**: p. 140-153.

2.65. Bose, A., et al., *Powder injection molding of Inconel 718 alloy.* Advances in Powder Metallurgy & Particulate Materials - 1997, 1997: p. 1899-18112.

2.66. International, S.A.E., *AMS5662M*, in *AMS 5662M* 2009.

2.67. Gessinger, G.H., *Powder metallurgy of superalloys*. Butterworths monographs in materials. 1984, London ; Boston: Butterworths. 348 p.

2.68. Rao, G.A., et al., *Characterisation of hot isostatically pressed nickel base superalloy Inconel*718.* Materials Science and Technology, 2003. **19**(3): p. 313-321.

2.69. Rao, G.A., M. Srinivas, and D.S. Sarma, *Effect of solution treatment temperature on microstructure and mechanical properties of hot isostatically pressed superalloy Inconel*718.* Materials Science and Technology, 2004. **20**(9): p. 1161-1170.
2.70. Rao, G.A., M. Srinivas, and D.S. Sarma, *Effect of thermomechanical working on the microstructure and mechanical properties of hot isostatically pressed superalloy Inconel 718.* Materials Science and Engineering a-Structural Materials Properties Microstructure and Processing, 2004. **383**(2): p. 201-212.
2.71. Rao, G.A., M. Srinivas, and D.S. Sarma, *Effect of oxygen content of powder on microstructure and mechanical properties of hot isostatically pressed superalloy Inconel 718.* Materials Science and Engineering a-Structural Materials Properties Microstructure and Processing, 2006. **435**: p. 84-99.
2.72. Marquez, C., G. Lesperance, and A.K. Koul, *PRIOR PARTICLE BOUNDARY PRECIPITATION IN NI-BASE SUPERALLOYS.* International Journal of Powder Metallurgy, 1989. **25**(4): p. 301-308.
2.73. Menzies, R.G., R.H. Bricknell, and A.J. Craven, *Stem Microanalysis Of Precipitates And Their Nuclei In A Nickel-Base Super-Alloy.* Philosophical Magazine A, 1980. **41**(4): p. 493-508.

CHAPTER 3. OBJECTIVES

Processes for powder metallurgy of superalloys are advantageously used in the production of aircraft engines as well as power generation turbines since the 1960's. The research efforts deployed in this field over the last 50 years are driven by the reduction of machining and labor cost, buy-to-fly (BTF) ratio, segregation and powder processing costs.

Mainstream alloy such as Inconel 718 is a good candidate for P/M process development. Alloy 718 is widely used in medium temperature zones of turbines because of its high temperature strength and oxidation resistance.

The development of near-net-shape P/M processes such as powder injection molding and additive manufacturing have gained increasing attention in the last decade as they nearly offer 1:1 BTF ratio and do not require extrusion and forging as in the powder billet processing route. In order for the mechanical properties of P/M parts to meet the specifications of wrought alloys, it is essential that full density sintering processes are developed to consolidate Inconel 718 P/M parts.

The main challenge in engineering the sintering process for Inconel 718 is to achieve full density while avoiding part distortion, prior particle boundary carbide film and formation of brittle TCP (Laves) phase. Consequently, the sintering behavior of alloy 718 has to be well understood with respect to the sintering temperature cycles, the effect of initial powder packing, heating rates and external pressure application. These parameters are of special interest as they will influence the mass transport kinetics responsible for sintering, grain growth and phase transformation.

The thought process underlying this thesis is focused on linking the sintering parameters to the sintering behavior and final microstructure of Inconel 718. To that extent, Inconel 718 sintering experimental results are presented in support of four specific objectives.

1. **Avoid distortion during pressureless sintering of Inconel 718 at supersolidus temperatures.** Superalloys are commonly sintered at supersolidus temperatures to assist sintering by promoting the formation of a partial liquid phase. Since the liquid phase assist sintering by capillary forces, prediction of the sintering behavior requires the evaluation of the liquid volume fraction with respect to the sintering temperatures. However, if above a critical threshold, the liquid phase content can cause a loss of rigidity in the porous compact resulting in distortion. The rigidity of the compact is of special importance since the near-net-shape advantage is negated when the sintering induces slumping of the part. Therefore, the first objective is to define a process window for the pressureless sintering of Inconel 718 green parts by modelling the softening of the compact in relation to the sintering temperature and grain size.

2. **Improve sintered Inconel 718 final density by starting with low porosity green compacts.** Green density is known to influence the sintered final density of P/M parts. Increasing the green density of Inconel 718 by conventional cold compaction is difficult due to its high strength. Therefore, binders addition are the best alternative to produce green compacts with typical relative densities of 60%-65%. However, cold gas dynamic spraying process can circumvent the limitations of binder-powder slurry injection molding by producing high compaction of Inconel 718 powder. High density green compacts offer good dimensional tolerance control since the sintering does not involve shrinkage. In fact, the sintering occurs mostly by neck formation and growth, converting interparticle mechanical bonds to metallurgical bonds, and filling the remaining pores. The present objective is to assess the final density, microstructure, and mechanical properties obtained after pressureless sintering of CGDS formed compacts.

3. **Controlling the Inconel 718 sintering cycle time by using high heating rates.** Rapid heating of green P/M parts reduces the amount of time spent in the temperature range in which non-densifying diffusion mechanism (surface diffusion) is occurring. Shortening the surface diffusion activity advantageously brings the porous compact at high temperature in a highly sinterable state; which should increase sintering rate and inhibit grain coarsening. Sintering Inconel 718 at high heating rates is interesting both for cutting the sintering cycle time and improving the microstructure. Understanding the impact of rapid heating on the sintering behavior and final microstructure of Inconel 718 is the third objective of this thesis.

4. **Investigate the effect of external pressure on sintered Inconel 718 final microstructure.** The application of external pressure increases the densification rate by a combination of plastic and viscous flow within the porous P/M compact. The pressure assisted sintering can potentially decrease the temperature needed to achieve full density, which will affect the amount of liquid phase formation during densification. In turn, the amount of liquid is believed to be related to TCP phase and prior particle boundary carbide network formation, both of which can be damaging to the mechanical properties of Inconel 718. Consequently, the fourth objective is to assess the microstructure of Inconel 718 sintered under uniaxial pressure; where the focus was on explaining the sintering mechanism and how it affects the final density, grain size and second phase particle formation (TCP and carbides).

CHAPTER 4. EXPERIMENTAL METHODOLOGY

This chapter describes the equipment and experimental methodology that was designed to produce the experimental results reported in chapter 5 through 8.

4.1. INCONEL 718 POWDER FEEDSTOCK

Gas atomized, spherical, Inconel 718 powder was used to prepare slip cast compacts. The powder was commercially distributed by Oerlikon (formerly Sulzer Metco) under the tradename AMDRY1718. The powder particle size distribution of AMDRY1718 is tailored for High Velocity Oxy Fuel (HVOF) spray technique and was chosen for the Cold Gas Dynamic Spray (CGDS) experiments as well as the sintering experiments. The powder chemical analysis, morphology and particle size distribution are reported in chapter 5 through 8.

4.2. DIFFERENTIAL SCANNING CALORIMETRY

The Inconel 718 powder was analysed by Differential Scanning Calorimetry (DSC) using a Netzsch TGA/DSC (STA-449-F3). The temperature scanning was from room temperature to 1260°C at a rate of 10°C/min. The measurement was performed under flowing argon (30 ml/min). The loose powder sample (57.8 mg) was enclosed in an alumina crucible. Finally, the DSC was calibrated by performing a blank to measure the baseline of the equipment. The baseline was substracted from the measurement automatically by the Netzsch software.

4.3. PREPARATION OF THE SLIP CAST INCONEL 718 COMPACTS

The binder used by Hajmrle and Anger [4.1] was selected for the production of slip cast Inconel 718 compacts. The binder is an aqueous solution of ammonium alginate (1%) which is commonly used in the food industry as a thickener. Binder proportions of 9%, 10%, 11% and

12% by weight were tested with AMDRY1718 powder. However, the fluidity of the slip cast compound below 12% of binder was not sufficient to properly fill the plaster mold cavity.

Plaster molds for slip casting were made out of Paris plaster mixed following the manufacturer instructions. The wet plaster was cast in cylindrical shaped molds: 150 mm diameter and 50 mm height. The wet plaster was left to cure and dry for 24h before machining cylindrical cavities of 25 mm diameter and 12 mm depth.

After machining the cavities, the slip cast compound was poured and packed in the plaster mold using a clean laboratory stainless steel spoon. The compacts were left to dry for 24h at room temperature and they were reclaimed by breaking the plaster mold with a chisel. Figure 4.1 presents a slip cast Inconel 718 compact.

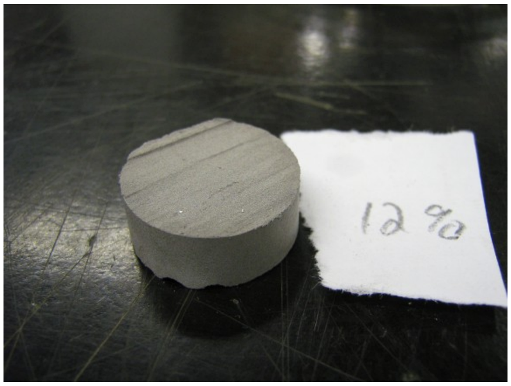

Figure 4-1 : Slip cast Inconel 718 compact with 12% weight ammonium alginate solution

4.4. PRESSURELESS SINTERING

A vertical tube furnace mounted with a diffusion pump unit was used for the pressureless sintering experiments as shown in Figure 4.2. The slip cast compacts were loaded on a mullite ceramic platform which could be raised in the vertical tube, along with titanium sponge that acted as oxygen and nitrogen getter.

After inserting the sample in the furnace and sealing the tube, two argon purges were performed. The purge was done by using the mechanical pump to reduce the tube inner pressure to 1 mTorr, after which the vacuum valve was shut to perform an argon backfill.

The heat schedule included a debinding isothermal hold for the slip cast compacts, followed by sintering. Of course, debinding was skipped when sintering the CGDS deposits. Debinding was performed under vacuum (1 mTorr) by heating to 530°C at 3°C/min and holding for 20 minutes. Sintering was done under higher vacuum with the diffusion pump open (10^{-2} mTorr). The heating rate to the sintering temperature was 5°C/min and the furnace control was able to maintain the temperature within ±5°C of the setpoint. After completion of the sintering holding time, the sample was furnace cooled to 200°C and then the vacuum was shut to purge the tube with argon.

Figure 4-2 : Vacuum furnace utilized to sinter slip cast Inconel 718 and CGDS deposits

4.5. COLD GAS DYNAMIC SPRAY

CGDS was performed using a CGT Kinetiks 4000 gun (Cold Gas Technology, Ampfing, Germany), with nitrogen as the carrier gas. The key part of the CGDS gun is the deLaval nozzle (convergent-divergent) which is designed to accelerate the gas stream to supersonic velocity. The nozzle used for this study is shown in Figure 4.3. The nozzle is characterized by a few measurements as the throat diameter (2.67 mm), convergent / divergent length (43 mm / 120 mm), inlet inside diameter (17.8 mm) and outlet inside diameter (5.3 mm).

Figure 4-3 : CGDS deLaval nozzle and fixture used to cold spray Inconel 718

The gun to substrate distance was 60 mm, the gas pressure was 35 bars, and the gas was heated to 800°C. The particle velocity was measured using a time-of-flight particle diagnostic system DPV2000 (Tecnar Automation, St-Bruno, QC, Canada). For the process parameters employed, the average particle velocity was 750 m/s, with a powder feed rate of 23.7 g/min, and a travel speed of 100 mm/s. The powder deposited using CGDS was sintered in a vacuum furnace to study the effect of green density on the sintering behavior of Inconel 718.

4.6. SPARK PLASMA SINTERING AND FREE PRESSURELESS SPARK PLASMA SINTERING

SPS and FPSPS experiments were performed with a Thermal Technology LC 10-3 press shown in Figure 4.4. The press has a 3000 Amp power supply with maximum voltage of 10V. The current and hydraulic pressure applied to the rams are controlled by a PID unit in the control panel. The temperature sensor for the control loop is located in the graphite lower punch, 2 mm from the sample as shown in Figure 4.5a. The experimental parameters were the sintering temperature, heating rate, pressure and holding time. All experiments were done using the same on/off pulse ratio of 36:8 ms.

The procedure for SPS of Inconel 718 required special attention to the powder loading into the graphite die. Alloy 718 is rich in carbide forming elements and a bonding reaction was found to occur for sintering temperature higher than 1200°C. To avoid contamination of the powder compact surface with carbon (and ruining the die), the graphite die was lined with 12µm thick molybdenum foil.

The FPSPS experimental setup is shown in Figure 4.5b. The setup is inspired from Bradbury and Olevsky [4.2] and was used to study the effect of high heating rates on the sintering of Inconel 718. In the FPSPS experiment, the current flows through the die, but not through the sample. Therefore, the die is heated by Joule effect and the sample is heated by radiation heat transfer within the graphite chamber.

Figure 4-4 : Thermal Technology LLC 10-3 SPS press used to sinter Inconel 718 powder in the SPS and FPSPS experiments

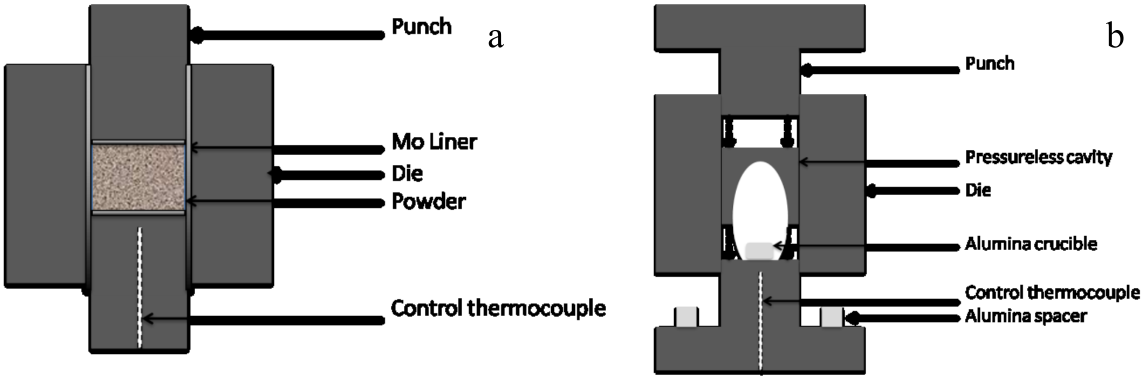

Figure 4-5 : Sketch of the SPS die assembly (a) and FPSPS experiment die assembly (b)

The density of sintered Inconel 718 was measured using the Archimedes method as per ASTM B962 [4.3]. The final sintered density was used to compute the density of the powder during the SPS experiment from the ram displacement data using equation 4.1.

$$\rho = \rho_f h \big/ \big(h + (\Delta L)\big) \qquad \text{eq. 4.1}$$

where ρ is fractional density, ρ_f is final fractional density, *h* is height of the sintered compact (mm) and $\Delta L=L(t)-L_f$ is displacement difference between the ram position at time *t* and the final position of the ram once the sintering cycle is finished.

4.7. OPTICAL MICROSCOPY

Optical micrographs were obtained using a Nikon optical microscope equipped with a Clemex Vision system for image analysis. Samples sections were cut using a low speed waffering diamond blade. Prepared sections were cold mounted in epoxy under vacuum for pore impregnation. Mounted samples were then manually grinded with 600 grit paper and polished using 9 µm, 3 µm, 1 µm and colloidal silica. Chemical etching with Aqua Regia (3:1 $HCl:HNO_3$) immersion for 3-20 sec. was used to reveal grain boundaries of CGDS samples. FPSPS samples were electroetched using a solution of 10 ml HNO3, 5 ml glacial acetic acid and 85 ml H2O under 1.5V for 5-20 seconds. Grain size characterization was performed using the Clemex software by manually measuring the diameter of the grains. Each grain was measured on its longest and shortest diameter to average the grain size. CGDS deposits porosity was characterized by image analysis of the polished sections. Clemex software was utilized for pore detection and area fraction calculations.

4.8. SCANNING ELECTRON MICROSCOPY

A Hitachi 4700SN FE-SEM and a Hitachi 3400N were used to acquire images of the bending test rupture face, grain boundaries, carbides and PPBs. Microchemical analysis of the phases found in the structure was performed by Energy Dispersive X-Ray Spectroscopy (EDS). Electron Channeling Contrast Images were obtained on this microscope to measure grain size of the Inconel 718 sintered in SPS (see procedure in 4.7). The sample preparation for this technique was different than the procedure given in 4.7. The samples were left unmounted and were electropolished in 2:8 perchloric acid:methanol at -40°C and 25V for 25 sec, followed by electroetching in the same solution at 5V for 3 sec.

4.9. X-RAY DIFFRACTION

Phase analysis for the identification of the residue from electrolytic etching performed in chapter 8 was conducted by X-Ray diffraction using Phillips PW1070 diffractometer (Cu Kα $\lambda = 1.54056$ Å). A pattern was obtained by scanning from 30°-80° (2θ) using a step size of 0.005° and a dwell time of 0.15 s/step. The patterns were analyzed using XPert Highscore software for signal processing and association with the powder diffraction file (pdf) database.

4.10. HARDNESS TESTING

Polished cross sections of CGDS Inconel 718 as deposited and sintered were used to measure the microhardness with a Clark Microhardness tester (CM-100-AT). Loads of 25 gf and 500 gf were used with a loading time of 15 sec. Images taken before and after indentation were used to assess the Inconel 718 deposit consolidation.

4.11. FLEXURAL STRENGTH TESTING

Three-point bending tests were performed, both on as-sprayed and sintered CGDS samples, using a Tinius-Olsen H25K-S Universal testing machine (Figure 4.6) equipped with a 25 KN load cell and LVDT for displacement measurement. Three bars (12 mm x 1 mm x 1 mm) for each condition were tested using a jig with a span of 7 mm. The reported flexural strength and strain were taken from the average of three tests. Flexural stress was calculated from the force measurement and the sample geometry through equation 4.2:

$$\sigma_{flex} = \frac{3PL}{2bd^2} \qquad \text{eq. 4.2}$$

where σ_{flex} is the flexural stress (MPa), P is the force applied (Newton), L is the span between the sample supports (mm), b is the width, and d is the thickness of the sample (mm), respectively. Similarly the strain was computed from equation 4.3 :

$$\varepsilon_{flex} = \frac{6Dd}{L^2} \qquad \text{eq. 4.3}$$

where ε_{flex} is the flexural strain, and D is the displacement.

Figure 4-6 : Tinus-Olsen H25K-S Universal testing machine

4.12. REFERENCES

4.1. Hajmrle, K. and R. Angers, *Sintering of Inconel 718.* International Journal of Powder Metallurgy, 1980. 16(3): p. 255-266.

4.2. Bradbury, W.L. and E.A. Olevsky, *Production of SiC-C composites by free-pressureless spark plasma sintering (FPSPS).* Scripta Materialia, 2010. 63(1): p. 77-80.

4.3. *ASTM B962-14, Standard Test Methods for Density of Compacted or Sintered Powder Metallurgy (PM) Products Using Archimedes' Principle*. 2014: West Conshohocken, PA.

CHAPTER 5. SUPERSOLIDUS LIQUID PHASE SINTERING MODELING OF INCONEL 718 SUPERALLOY

D. Levasseur and M. Brochu

5.1. PREFACE

The first study presented in this thesis is directly in line with the first objective, which is to avoid distortion during pressureless sintering of Inconel 718. This chapter focuses on the formation of liquid phase in the powder compact as a sintering driving force, but also as a source of distortion. The results are compared with data for Inconel 718 obtained by other workers and the whole dataset is used to model the distortion threshold of Inconel 718 based on the model developed by Liu *et al.* Note that the conclusion was removed from the manuscript and is reported in Chapter 10: Conclusions

This manuscript was submitted to Metallurgical and Materials Transactions A (2015)

5.2. ABSTRACT

Powder metallurgy of Inconel 718 superalloy is advantageous as a near-net shape process for complex parts to reduce the buy-to-fly ratio and machining cost. However, sintering Inconel 718 requires the assistance of supersolidus liquid formation to achieve near full density and involves the risk of distortion at high temperatures. The present work is focused on modeling the onset of sintering and distortion as a function of temperature, grain size and part geometry for Inconel 718. Using experimental sintering results and data available in the literature, the supersolidus liquid phase sintering of Inconel 718 was modeled. The model was used to define a processing window where part distortion would be avoided.

5.3. INTRODUCTION

Powder injection molding (PIM) and binder jetting (BJ) additive manufacturing (AM) routes [5.1] are key avenues to fabricate complex parts, and more advantageous for high strength and specialty alloys. The PIM and BJ routes involve the mandatory use of a binder to create the green compact either under a molding action or via a layer-by-layer approach, followed by a sintering cycle. Some of the benefits of these near-net shape routes include the sustainable raw material usage, lower energy consumption, and limiting the difficulties associated with machining operations. These processing advantages explain the surge of research on these processes for the Inconel systems [5.2-5.12] for high temperature applications including turbines (jet engine, energy production), pumps or rocket motors [5.13].

The primary drawback of these approaches for Inconel 718 resides in the low sinterability of the green compact. Typical industrial practices, to reach mechanical properties equivalent or superior to that of wrought counterparts, involve a two-step process where sintering is initially carried out followed by hot isostatic pressing (HIP) as the final step [5.6, 5.8-5.12]. This first sintering step can be associated with distortion [5.14-5.15], defeating the advantage of the near-net shape approach. As such, a careful understanding of the sintering cycle is necessary to control the competitive interaction between maximising density and minimising distortion.

Nickel-based superalloys are often sintered in the semisolid regime, a technique also called supersolidus liquid phase sintering (SLPS) [5.6, 5.10]. The development of a liquid phase during sintering causes rapid shrinkage of the part and is used by many to achieve close to full density with Inconel 718 powders [5.3-5.6, 5.8-5.12]. Shape retention during SLPS was studied by Liu *et al*. [5.14]. They modeled the distribution of the liquid phase in the compacted powder microstructure and were able to predict the onset of sintering and distortion based on the physical properties of the powder and the sintering temperature. Their model is described in the following section.

5.3.1. The SLPS Model

The effect of the liquid formation on the compacted powder part is directly related to the structure of the part, in essence the particle size and the grain size. The liquid first covers grain boundaries and disrupts particle cohesion leading to a rearrangement of the grains driven by capillary forces and liquid flow under pressure gradients [5.14, 5.16-5.17]. The rigidity of the part is assumed to be mainly linked to the extent of solid bonds between grains. The liquid film at grain boundaries may act as a lubricant for grain sliding, but can also maintain the cohesion between grains by its viscous resistance to deformation [5.14]. The understanding of the distribution of liquid on grain boundaries is thus the first step in assessing the rigidity of the compacted powder.

The coverage of solid grains by liquid (F_C) was described by Campbell [5.18] with a simple model using the liquid volume fraction (V_L) and the dihedral angle (ϕ) as shown in equations 5.1 and 5.2:

$$F_C = 2.64\left(\frac{V_L}{k}\right)^{1/2} \qquad \text{eq. 5.1}$$

$$k = \sqrt{3} + \frac{3}{\tan\left[30-(\phi/2)\right]} - \left[\frac{30-(\phi/2)}{60}\right]\frac{\pi}{\sin^2\left[30-(\phi/2)\right]} \qquad \text{eq. 5.2}$$

The model was used by Liu *et al.* [5.14] to define the contiguity of the semisolid structure (C_{SS}) as per equation 5.3:

$$C_{SS} = 1 - F_C \qquad \text{eq. 5.3}$$

They further used a geometrical relationship to link the thickness of the grain boundary liquid film (δ) with the contiguity, the grain size (G) and the liquid volume fraction by using equation 5.4:

$$\delta(1-C_{SS})=\frac{G}{3}\frac{V_L}{(1-V_L)} \qquad \text{eq. 5.4}$$

This equation states that the grain boundary liquid film thickens when either the liquid fraction or grain size increases. In turn, an increase in liquid film thickness reduces the viscous resistance of said film as expressed by equation 5.5:

$$R=\frac{\eta_L \upsilon A^2}{\delta^3} \qquad \text{eq. 5.5}$$

where R is the force of the resistance to movement between two grains, η_L is the viscosity of the liquid phase, v is the relative velocity of the two grains and A is the area of the grain faces.

The liquid film viscous force combined with the resistance of the solid contacts between grains (σ_{SS}) defines the bond strength between two grains as shown in equation 5.6:

$$F_{bond}=\pi G^2\sigma_{SS}C_{SS}+\frac{\alpha\eta_L\pi G^4(1-C_{SS})^2}{\delta^3} \qquad \text{eq. 5.6}$$

where πG^2 is the surface area of a grain and α is a constant with units of velocity. Equation 5.6 is used to define the rigidity of the compacted powder part with the first term expressing the resistance of the solid contacts and the second term relating to the viscous resistance of the liquid film between grains.

Two forces acts on the grains during sintering, namely the capillary force and gravity. The former is responsible for the shrinkage of the porous part while the latter is responsible for the distortion of the semisolid part. The onset of shrinkage occurs when the capillary force becomes larger than the bonding force; and in the same way the onset of distortion occurs when the gravitational force is higher than the resistance of the part. The capillary force acting on grains separated by a liquid film has been studied by Liu *et al*. [5.19] and is estimated by equation 5.7:

$$\sigma=\frac{5.2\gamma_{LV}\cos\theta}{D\left(1-(\rho_g/\rho)^{1/3}\right)} \qquad \text{eq. 5.7}$$

where γ_{LV} is the liquid-vapor surface energy, θ is the wetting angle (assumed to be 0°), D is the mean particle diameter, and ρ and ρ_g are the density of the part and the green density respectively. The densification during SLPS is driven by the shear stress which is half the capillary stress between two grains [5.17]. Thus to take into account the shear stress and the force acting on the grains equation 5.8 is used:

$$F_{\max} = \frac{2.6\gamma_{LV}\cos\theta}{D\left(1-\left(\rho_g/\rho\right)^{1/3}\right)}\pi G^2 \qquad \text{eq. 5.8}$$

The gravitational force on the other hand is expressed by equation 5.9:

$$F_G = \frac{\rho g h}{2} \qquad \text{eq. 5.9}$$

where F_G is the maximum shear force caused by gravity on the bottom grains of a part with height h and density ρ.

Comparing equations 5.8 and 5.9 with equation 5.6, Liu *et al.* [5.14] defined two criteria for the onset of sintering and onset of distortion, respectively. Since the rigidity of the part is related to the liquid film thickness, equation 5.4 is also used to define the criteria. The reader is referred to the work of Liu *et al.* for a complete demonstration of the model, as only the criteria are presented here in equations 5.10 – 5.12:

$$\xi_{densif} = \left(\frac{\alpha\eta_L}{\sigma_{SS}}\right)^{1/3}\frac{\left(1-C_{SS}\right)^{5/3}}{\left(A-C_{SS}\right)^{1/3}}, A = \frac{2.6\gamma_{LV}\cos\theta}{D\left(1-\left(\rho_g/\rho\right)^{1/3}\right)}\frac{1}{\sigma_{SS}} \qquad \text{eq. 5.10}$$

$$\xi_{distort} = \left(\frac{\alpha\eta_L}{\sigma_{SS}}\right)^{1/3}\frac{\left(1-C_{SS}\right)^{5/3}}{\left(B-C_{SS}\right)^{1/3}}, B = \frac{\rho g h}{2}\frac{1}{\sigma_{SS}} \qquad \text{eq. 5.11}$$

$$\xi = \frac{G^{1/3}}{3}\frac{V_L}{\left(1-V_L\right)} \qquad \text{eq. 5.12}$$

where ζ_{densif} is the criterion for the onset of sintering, $\zeta_{distort}$ is the criterion for the onset of distortion and ζ is the softening parameter. Therefore, when $\zeta \geq \zeta_{densif}$ the shrinkage is initiated and when $\zeta \geq \zeta_{distort}$ distortion of the part occurs.

The objective of this paper was to combine experimental data and reported values to propose a unified SLPS model, delineating the processing window for Inconel 718. The experimental data and relationships generated for this work include the liquid fraction evolution with temperature, the densification and the grain size for different sintering cycles. The proposed model, which accounts for the effects of the microstructure and the part geometry, was able to predict the onset of sintering and distortion from analysis of the rigidity of the semisolid system.

5.4. EXPERIMENTAL METHODS

The Inconel 718 powder used in this study was provided by Sulzer Metco, under the trade name of AMDRY 1718. The powder composition, as provided by the manufacturer, is listed in Table 5.1. A micrograph of the powder is shown in Figure 5.1a. The particle size distribution was measured by laser interferometry using a Horiba LA-920 Particle Size Analyzer and the particle size cumulative frequency graph is presented in Figure 5.1b.

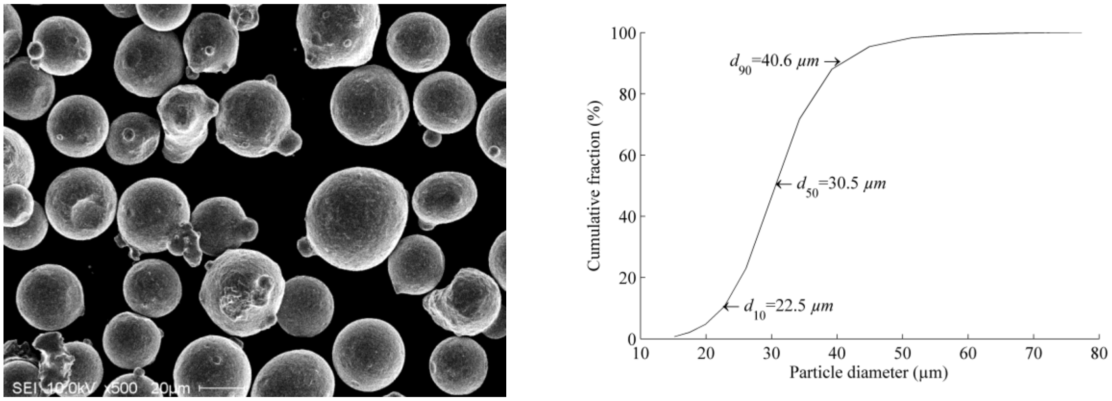

(a) (b)

Figure 5-1 : a) SEM image of the powder and b) particle size analysis

The multi-melting events were measured using differential scanning calorimetry (DSC) of the powder in a Netzsch TGA/DSC (STA-449-F3), with a scanning interval from room temperature to 1533K using a heating rate of 10K/min under a flowing argon atmosphere. The contribution of the heat capacity from the sample and crucible are subtracted from the heat balance equation (equation 13) by calibration and baseline fitting which is commonly used for DSC analysis [5.20].

$$Q_{melting} = V_l m_{sample} \Delta H \qquad \text{eq. 5.13}$$

where $Q_{melting}$ is the heat (Joules) measured by DSC after correction of the DSC trace, m_{sample} is the sample mass and ΔH is the latent heat of fusion.

Table 5-1 : Chemical analysis of the AMDRY 1718 powder

	Al	C	Co	Cr	Fe	Nb	Ni	Mo	Ti	O
wt%	0.43	0.05	0.09	19.11	17.92	5.07	53.07	3.13	0.94	0.02

The preparation of compacts was done using a slip casting technique described by Hajmrle and Anger [5.4]. The slip casting slurry was prepared with 60 vol. % solid loading using a 1 wt% ammonium alginate aqueous solution as the binder. The slurry was cast in plaster molds to obtain cylindrical samples with a diameter of 2.5 cm and height of 0.6 cm, then left to dry in ambient air for 24 h. The green compacts were then debinded by a thermal decomposition step at 803K for 20 min under vacuum (10^{-3} torr). Upon debinding the vacuum level was reduced to 10^{-5} torr and the furnace was ramped to the sintering temperature at a rate of 5K/min. The sintering temperatures and soak times used in this study were 1473K, 1498K and 1523K, and 10, 60 and 180 min, respectively. The temperature deviation in the furnace was measured to be ±5K using a thermocouple located beside the compact. After the soaking period, the compacts were furnace cooled to room temperature. The compacts density was measured using the Archimedes method [5.21]. Preparation of the samples for microstructure observation was done using cold resin mounting under vacuum to ensure impregnation of the porous compact. The mounted samples were ground and polished using silicon carbide grinding papers (80, 200, 600 grit) and diamond suspension (9µm, 1µm) on polishing cloths, respectively. A final polishing step was done with colloidal silica immediately followed by etching with Aqua Regia solution (3:1 $HCl:HNO_3$) for 3 - 20 seconds. The microstructure was observed using a light optical microscope and grain size was measured using Clemex image analysis software. A minimum of 300 grains were measured to compute the average grain size.

5.5. RESULTS AND DISCUSSION

5.5.1. Thermal analysis

DSC was used to detect the melting events in the starting powder in order to identify the boundaries for the SLPS trials. A representative DSC trace is presented in Figure 5.2. As depicted, three thermal events were detected. First, two endothermic peaks measured at 1271K and 1401K were attributed to the γ+Laves→L event and agree well with the data from Antonsson *et al.*[5.22] who measured a solidification temperature range of 1433K – 1348K for this reaction. The second thermal event identified was the exothermic reaction γ+Laves→L+NbC occurring at 1411K. Antonsson *et al.* [5.22] reported the formation of NbC carbides to occur at 1433K, which is also in agreement with the current measurements. Finally, the γ+NbC→L event, shown as an endothermic peak, starts at 1520K. This eutectic temperature is in line with the eutectic onset temperature found in the literature (1498K − 1544K) [5.22-5.23]. The thermal events detected demonstrate that the current powders exhibit the characteristic melting events observed in Inconel 718. The small discrepancies observed between the reported temperatures and the experimental data is common for superalloys, and is explained by differences in alloying element content, segregation level and dendrite arm spacing of the starting materials [5.22]. As reported, the first melting event occurs at 1271K, defining the SLPS regime lower boundary.

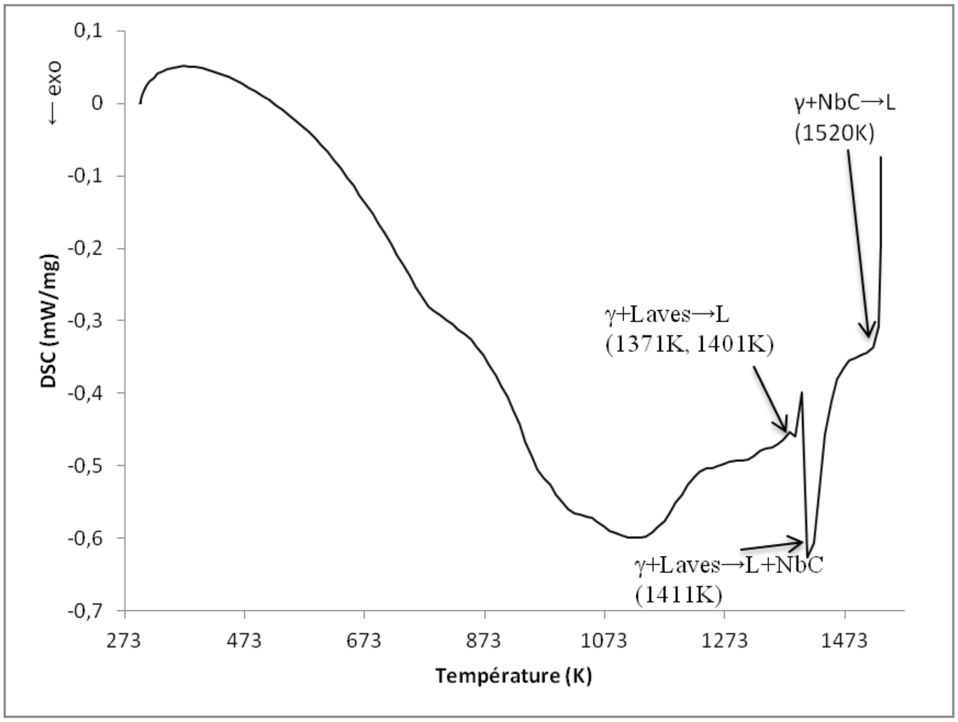

Figure 5-2 : DSC trace of the Inconel 718 powder between room temperature and 1433K scanned at 10K/min

The DSC results were used to evaluate the liquid fraction developed in the Inconel 718 powder by using equation 5.13. Using the latent heat of fusion reported by Antonsson *et al.* (241 kJ/kg) for all the melting events, the liquid fraction formed was calculated. The liquid fraction values obtained within the experimental limits of the available equipment are presented in Figure 5.3. The melting behavior of Inconel 718 powders is a non-equilibrium process. No experimental data of the liquid fraction formed during powder heating has been reported in previous work. However, Antonsson *et al.* reported on the liquid fraction present during solidification of Inconel 718 calculated from DSC heat release and measured from the microstructure of 8 samples quenched at temperatures of 1597K, 1593K, 1567K, 1566K, 1516K, 1461K, and 1411K. Their reported experimental liquid fraction values are shown in Figure 5.3. As depicted, the current results are in agreement with Antonsson *et al.'s* work. Moreover, Thermo-Calc software was used to assess the effect of binder carbon contamination on the liquid formation. The solid fraction of Inconel 718 at two carbon concentration of 0.05% and 0.12% was computed and the resulting melting curves are shown in Figure 5.3. The solid fraction is significantly modified by carbon contamination, especially at temperatures over 1540K, where it decreases sharply for the 0.12% carbon concentration. The 1540K solid fraction obtained at 0.12% carbon is 6.8% lower than at 0.05% carbon and the difference increases to 8.6% at a temperature of 1472K. Carbon contamination from the binder or other sources modifies the sintering behavior of Inconel 718 by changing the equilibrium liquid fraction formation, however the carbon contamination using ammonium alginate binder was shown to be negligible by Hajmrle [5.24]. In the current study, an exponential regression line fitting both DSC data sets obtained in this study and by Antonsson *et al.* was used to interpolate the liquid fraction for all temperatures needed to cover the SLPS regime.

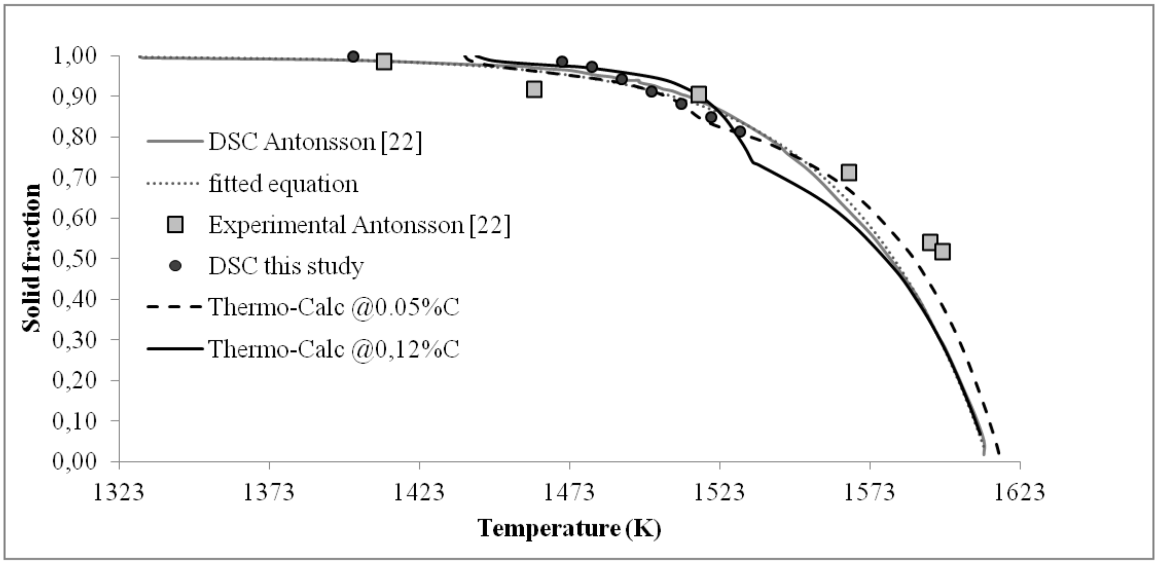

Figure 5-3 : Solid fraction determined for Inconel 718 as a function of temperature by DSC measurement and by experimental observation [5.22]

5.5.2. Densification and microstructure evolution

The densities measured for each sintering experiment are presented in Figure 5.4, along with reported densities from other works. As expected, both time and temperature were found to positively influence the densification. The densification is more efficient at 1523K with a density of 89.9% after 10 minutes compared to 71.1% and 57.7% after 10 minutes at 1498K and 1473K, respectively. This difference is due to the increase in liquid fraction; the calculated liquid fractions are 4.7% for 1473K, 8.1% for 1498K and 14.0% at 1523K, respectively. The samples were not distorted after sintering meaning they still had enough rigidity to sustain their own weight.

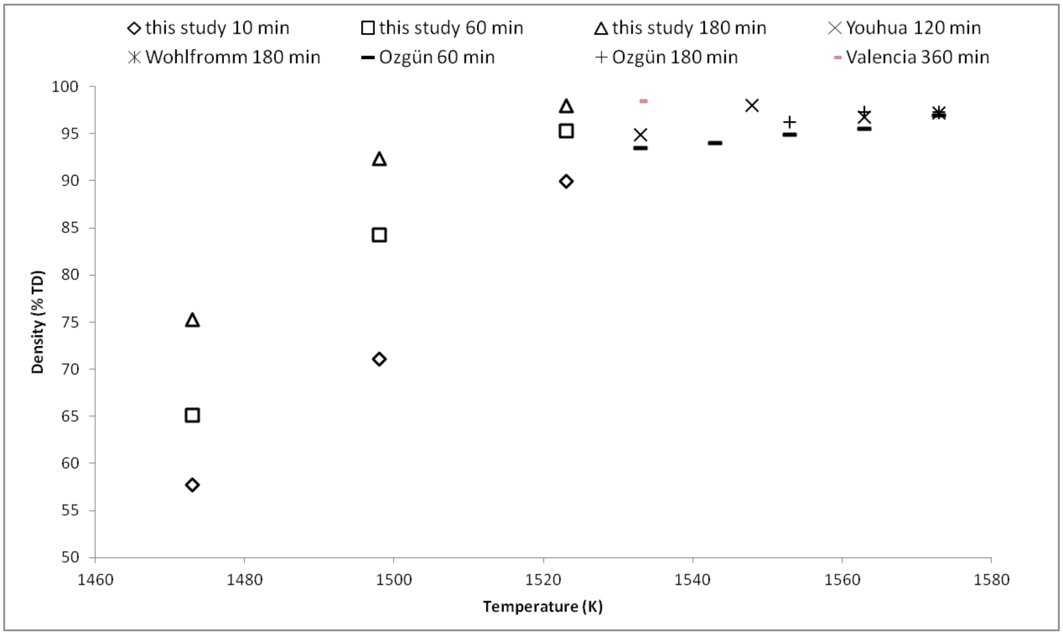

Figure 5-4 : Sintered density measured in this study and from other works [5.6, 5.8, 5.10-5.11]

The last experimental data needed to calibrate the SLPS model is the grain growth during sintering. The grain size was measured for each sample and presented in Figure 5.5. As depicted, the results are in agreement with previously published studies.

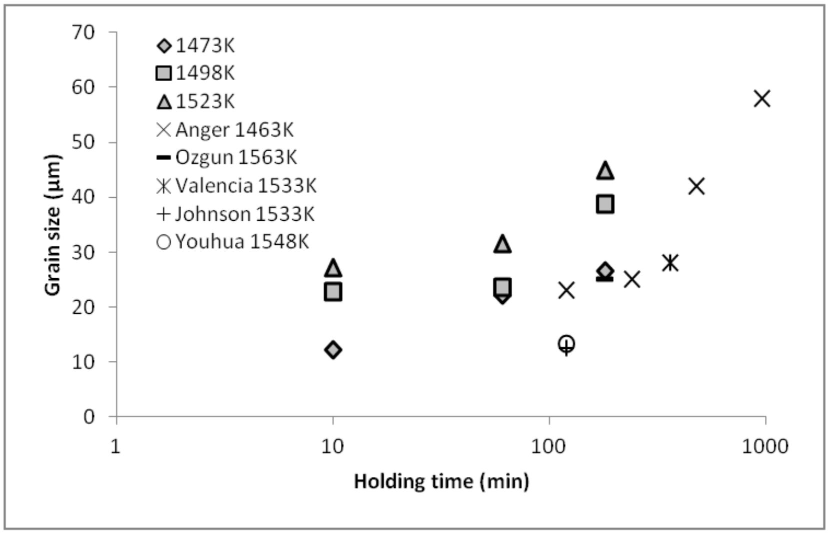

Figure 5-5 : Grain size data measured in this study and from other works [5.5-5.6, 5.8, 5.11, 5.25]

The grain size measured at 1473K is in line with the results obtained by Anger and Hajmrle at 1463K for similar powder particle size [5.25]. However, the mean particle size used in other studies varies from 7.4 µm to 15 µm, which is one-half to one-third of the average particle size used in this study and explains the lower grain size obtained in other studies. Grain growth during sintering is often described by the usual coarsening model as expressed in equation 5.13:

$$G^n - G_0^n = kt \qquad \text{eq. 5.13}$$

where G_0 is the grain size at the beginning of the isothermal hold, n is the grain growth exponent (usually $n \geq 2$ [5.26]), k is the temperature dependant constant, and t is the isothermal time. The grain sizes in the current study and from the work of Anger and Hajmrle were analyzed to determine the grain growth exponent in order to identify the grain growth mechanism occurring during SLPS; regression analysis of the grain size data is presented in Figure 5.6. Lack of completeness in the reported grain size and extent of studied processing parameters prevented the analysis of a larger number of works. As shown, the data is converging towards a grain growth exponent of 1, which is associated with partial pinning of the grain boundaries by the remaining porosity. This influence of the porosity on the grain growth also qualitatively fits the grain size measurement from others works, where smaller grain size were obtained for increased sintering conditions, as per their smaller starting particle size.

5.5.3. SLPS model prediction of sintering and distortion onset for Inconel 718

The sintering results obtained in this work, as well as reported works carried out in a similar temperature range, exhibit typical SLPS behavior. The density increases steeply between temperatures of 1473K – 1523K due to the increasing liquid volume fraction that allows capillary forces to act on grains and fill voids between particles. As previously mentioned, the liquid fractions calculated for the samples sintered at 1473K, 1498K and 1523K are 4.7%, 8.1% and 14.0%, respectively. According to German [5.16], the liquid fraction needed to achieve semisolid state is between 10% - 40%; when the liquid volume fraction is within this range the compact is mushy (5% - 25%), whereas the compact is considered rigid when the liquid fraction is lower (<5%). The mushy state refers to a semisolid structure where the liquid cannot flow within the solid skeleton. The overlap between mushy and semisolid state is related to the melt behavior of different materials. Densification is still assisted by the presence of <10% liquid fraction. However, as demonstrated for the samples sintered at 1523K, the shrinkage drastically increases when the liquid fraction increases over 10%.

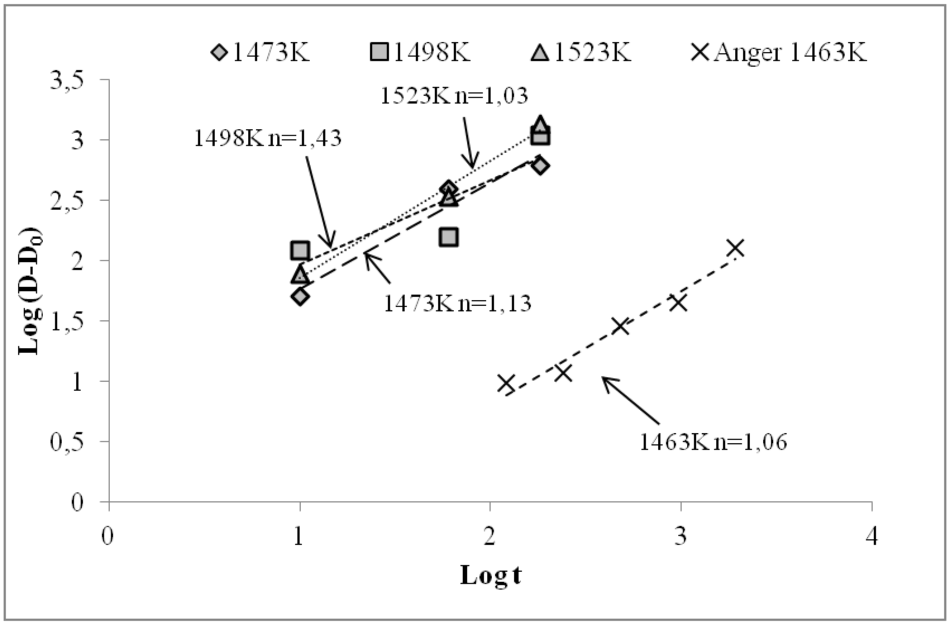

Figure 5-6 : Log–log plot used to determine the grain growth exponent measured in this study and by Anger [5.25]

The sintering temperatures used in other studies mostly range from 1533K to 1573K. The 1573K upper limit was reported by Wohlfromm [5.10] as the maximum temperature that could be used without distortion caused by slumping of the compact. In fact the liquid fraction predicted for 1573K is 42% which is larger than the 40% maximum liquid fraction defining the semisolid regime. At this liquid fraction content, most metals behave like fluids and distortion is expected.

To take into account the effect of microstructure (particle size, grain size) on the distribution of liquid in the compacts, Liu *et al.* [5.14] introduced a factor defined as the softening parameter (ζ). The definition of this parameter uses the liquid fraction and grain size to determine the liquid film thickness as shown in equation 5.12. The softening parameter for Inconel 718 was calculated for the current experimental data as well as for the available literature data. The modeled curves of the softening parameter as a function of grain size for each temperature used in this study and by other workers can be found in Figure 5.7, superimposed with the softening parameter calculated for the corresponding experimental data points.

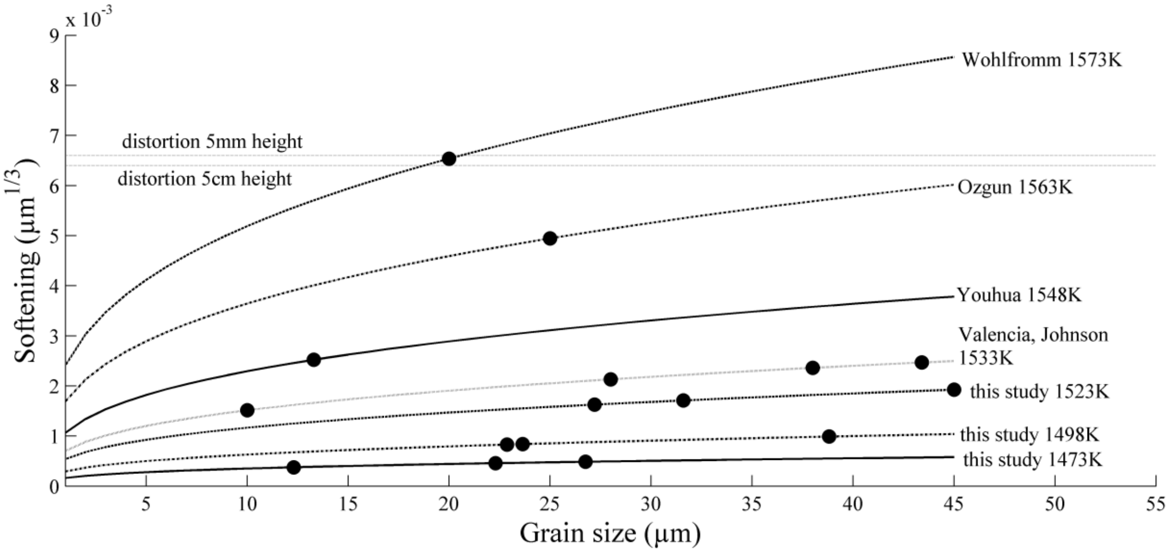

Figure 5-7 : Softening parameter calculated for the experimental conditions used in this study and in other works [5.5-5.6, 5.8, 5.10-5.11]

The softening parameter increases with grain size, and more so increases with temperature. The distortion threshold was determined according to the results of Wohlfromm *et al.* who found the maximum temperature of sintering without distortion for 5 mm height Inconel 718 samples was 1573K with an average grain size of approximately 20 µm. As seen in Figure 7, at 1573K a slight increase in grain size over 20 µm during the sintering of 5 mm height samples can potentially cause distortion because the softening parameter crosses the distortion threshold for this geometry. The onset of distortion estimated from the experimental data of Wohlfromm [5.10] is indicated on the graph at a softening value of 0.0066 µm$^{1/3}$. Interestingly, Ozgun *et al.* reported distortion at 1573K but not at 1563K meaning that the grain size they obtained was probably higher than the threshold for their sample geometry (not described by the author). Finally, to determine the onset of sintering, we defined its occurrence as when the shrinkage (defined as the linear dimensional change $\Delta L/L_0$) reached 1%. Based on the results of Hajmrle and Anger and the results of this study, a softening parameter at the onset of sintering of 0.0005 µm$^{1/3}$ was found. Using the experimental values of $\zeta_{distortion}$ and ζ_{onset} in equation 10 and 11, along with the experimentally determined viscosity of liquid Inconel 718 [5.27] and a dihedral angle of

30°, the set of equations were solved to find α and σ_{ss}. To simplify the calculations, the average viscosity of Inconel 718 between 1473K and 1573K was considered constant [5.27]. All the parameters used in the calculations are given in Table 2. The mechanical strength of solid-solid contacts was found to be 0.173 MPa, which is a reasonable value given that the yield strength of semisolid systems usually range between 0.00001 MPa and 100 MPa [5.16]. The velocity constant was found to be 0.319 m/s. This model permits the prediction of $\zeta_{distortion}$ and ζ_{onset} for varying compact geometry and powder particle size.

Table 5-2: Parameters used to compute $\zeta_{distortion}$ and ζ_{onset}

Viscosity	Dihedral angle	Wetting angle	Liquid vapor surface energy	Green density	Sintering onset density	Distortion onset density	Height
9 mPa	30° [5.14]	0° [5.16]	1.5 J [5.16]	0.6	0.61	1	5 mm [5.10]

As seen from the data presented in Figure 5.7, sintering Inconel 718 at temperatures higher than 1563K can be problematic if the furnace has poor temperature control or long sintering time is used (increase in grain size); because both the liquid fraction, which is temperature dependant, and grain growth, could increase the value of the softening parameter (eq. 5.12) over the distortion threshold value. However, simulations with various sample heights did not show a strong effect of this parameter on the distortion onset. The distortion onset for a 5 mm height sample occurred at 0.0066 $\mu m^{1/3}$ whereas it occurred at 0.0064 $\mu m^{1/3}$ for a 5 cm height part. This change could be enough to cause slumping during sintering at 1573K; however, the softening parameter for sintering done at 1563K seems to remain below the critical values for the range of grain sizes considered in this study.

ACKNOWLEDGEMENTS

The authors would like to acknowledge the McGill Engineering Doctoral Award financial support provided to D. Levasseur.

5.6. REFERENCES

5.1. Sachs, E., et al., *Three Dimensional Printing: Rapid Tooling and Prototypes Directly from a CAD Model.* Journal of Manufacturing Science and Engineering, 1992. **114**(4): p. 481-488.

5.2. Contreras, J.M., A. Jiménez-Morales, and J.M. Torralba, *Improvement of rheological properties of Inconel 718 MIM feedstock using tailored particle size distributions.* Powder Metallurgy, 2008. **51**(2): p. 103-106.

5.3. Davies, P.A., et al., *Metal Injection Moulding of Heat Treated Alloy 718 Master Alloy.* Advanves In Powder Metallurgy and Particulate Materials, 2003. **8**: p. 8-12.

5.4. Hajmrle, K. and R. Angers, *Sintering of Inconel 718.* International Journal of Powder Metallurgy, 1980. **16**(3): p. 255-266.

5.5. Johnson, J.L., et al., *Mechanical properties and corrosion resistance of MIM Ni-based superalloys.* Proceedings of PM2Tec 2004, 2004: p. 89-101.

5.6. Özgün, O., et al., *Microstructural and mechanical characterization of injection molded 718 superalloy powders.* Journal of Alloys and Compounds, 2013. **576**: p. 140-153.

5.7. Sicre-Artalejo, J., et al., *High-density inconel 718: Three-dimensional printing coupled with hot isostatic pressing.* International Journal of Powder Metallurgy (Princeton, New Jersey), 2008. **44**(1): p. 35-43.

5.8. Valencia, J.J., J. Spirko, and R. Schmees, *Sintering effect on the microstructure and mechanical properties of alloy 718 processed by powder injection molding.* Superalloys 718, 625, 706 and Various Derivatives, 1996: p. 753-762.

5.9. Schmees, R., J.R. Spirko, and J. Valencia. *Powder injection molding (PIM) of Inconel 718 aerospace components*. in *Proceedings of the Advanced Particulate Materials & Processes*. 1997.

5.10. Wohlfromm, H., et al., *Metal Injection Moulding of Nickel-based Superalloys for High Temperature Applications.* Proceedings Euro PM2003 Congr. Exhib., 2003. **3**: p. 207-215.

5.11. Youhua, H., et al., *Preparation and Mechanical Properties of Inconel718 Alloy by Metal Injection Molding.* Rare Metal Materials and Engineering, 2010. **39**(5): p. 775-780.

5.12. Bose, A., et al., *Powder injection molding of Inconel 718 alloy.* Advances in Powder Metallurgy & Particulate Materials - 1997, 1997: p. 1899-18112.

5.13. Betteridge, W. and S.W.K. Shaw, *Development of Superalloys.* Materials Science and Technology, 1987. **3**(9): p. 682-694.

5.14. Liu, J., A. Lal, and R.M. German, *Densification and shape retention in supersolidus liquid phase sintering.* Acta Materialia, 1999. **47**(18): p. 4615-4626.

5.15. German, R.M., *Manipulation of Strength During Sintering as a Basis for Obtaining Rapid Densification without Distortion.* Materials transactions, 2001. **42**(7): p. 1400-1410.

5.16. German, R.M., *Supersolidus liquid-phase sintering of prealloyed powders.* Metallurgical and Materials Transactions A: Physical Metallurgy and Materials Science, 1997. **28**(7): p. 1553-1567.

5.17. Liu, Y.X., R. Tandon, and R.M. German, *Modeling of Supersolidus Liquid-Phase Sintering .2. Densification.* Metallurgical and Materials Transactions a-Physical Metallurgy and Materials Science, 1995. **26**(9): p. 2423-2430.

5.18. Campbell, J., *Dihedral angle and the equilibrium morphology of grain boundary phases.* Metallography, 1971. **4**(3): p. 269-278.

5.19. Liu, Y.X., R. Tandon, and R.M. German, *Modeling of Supersolidus Liquid-Phase Sintering .1. Capillary Force.* Metallurgical and Materials Transactions a-Physical Metallurgy and Materials Science, 1995. **26**(9): p. 2415-2422.

5.20. Starink, M., *Analysis of aluminium based alloys by calorimetry: quantitative analysis of reactions and reaction kinetics.* International Materials Reviews, 2004. **49**(3-4): p. 191-226.

5.21. German, R.M. and S. Sant, *Powder Metallurgy and Particulate Materials Processing.* 2006. **31**(4): p. 351.

5.22. Antonsson, T. and H. Fredriksson, *The effect of cooling rate on the solidification of INCONEL 718.* Metallurgical and Materials Transactions B-Process Metallurgy and Materials Processing Science, 2005. **36**(1): p. 85-96.

5.23. Fayman, Y.C., *Microstructural Characterization and Elemental Partitioning in a Direct-Aged Superalloy (Da-718).* Materials Science and Engineering, 1987. **92**: p. 159-171.

5.24. Hajmrle, K., *Forgeage d'ébauches poreuses d'Inconel 718 préparées par coulage en moule poreux et frittage*. 1978, Université Laval: p. xxii, p. 413

5.25. Angers, R. and K. Hajmrle, *Grain growth during sintering of a nickel-base superalloy.* Scripta Metallurgica, 1980. **14**: p. 577-581.

5.26. Hu, H. and B.B. Rath, *On the time exponent in isothermal grain growth.* Metallurgical Transactions, 1970. **1**(11): p. 3181-3184.

5.27. Saunders, N., et al., *Using JMatPro to model materials properties and behavior.* JOM, 2003. **55**(12): p. 60-65.

CHAPTER 6. PRESSURELESS SINTERING OF COLD SPRAYED INCONEL 718 DEPOSIT

D. Levasseur, S. Yue and M. Brochu

6.1. PREFACE

The second result chapter addresses the second objective of the thesis: exploring the advantage of starting with a high density compact on the final density and microstructure. Compaction of prealloyed powder is not possible by cold pressing and other techniques must be sought. Cold gas dynamic spray (CGDS) process is used to obtain high-density deposits, which are sintered to consolidate the particles and achieve full density. The CGDS process uses high kinetic energy and moderate heat to compact prealloyed powders like Inconel 718. The following results are a first step to determine the feasibility and potential of the technique. The density, grain size, hardness and flexural strength obtained after pressureless sintering of Inconel 718 CGDS deposits are reported to compare to the wrought alloy properties. As mentioned previously the conclusion of this manuscript was removed and placed in Chapter 10.

Published: D. Levasseur, S. Yue, M. Brochu, Pressureless sintering of cold sprayed Inconel 718 deposit, Materials Science and Engineering: A, Volume 556, 30 October 2012, Pages 343-350
doi:10.1016/j.msea.2012.06.097

6.2. ABSTRACT

The deposition of Inconel 718 powders, by cold spray, was performed on a mild steel substrate. The deposits showed a porosity level lower than 3%, but lacked interparticle bonding, hence strength. To circumvent the problem, the deposits were used as green compacts for pressureless sintering at temperatures of 1200, 1225, and 1250°C for 10, 60, and 180 minutes. The grain size, second-phase distribution, micro-hardness, and flexural strength were measured. Upon sintering, the flexural strain increased from 0.026 to 0.183, and the fracture surfaces exhibited fewer interparticle defects. During the sintering treatment, minimal grain growth occurred in the 1200 and 1225°C trials where the calculated grain growth exponent was $n = 1/8$. However for the

sintering trials at 1250°C, the grain growth exponent was found to be n = 1/2. The grain growth was found to be influenced by secondary MC carbides that precipitated during the sintering treatment but dissolved at 1250°C. The carbides acted as a pinning phase during the sintering treatment, explaining the reduced grain growth for the 1200°C and 1225°C conditions.

6.3. INTRODUCTION

Cold Spray (CS) is a new technology known to deposit coatings with lower/minimal heat input imposed on the substrate and powder feedstock [6.1, 6.2]. In addition to coating applications, CS was found to be attractive for building protrusions on substrates [6.3] and even for joining materials [6.4]. The scientific literature tends to agree that jetting and adiabatic shear at the particle boundaries is responsible for the establishment of the interparticle metallurgical bonds [6.5]. However, this line of thought is believed to be valid only for soft materials, such as Cu. For hard-to-deform materials, such as Inconel, the limited plastic deformation upon particle impact is believed to be insufficient to cause metallurgical bonding. Consequently, such deposits would possess a mechanical behavior similar to a high-density/quality green compact, i.e. low strength without ductility.

In order to investigate the possibility of gaining physical and mechanical properties, post-deposition heat treatments are starting to be investigated. Phani *et al.* [6.6], in particular, have studied the effects of annealing Cu deposits to recover physical properties. Their results have shown a reduction of the electrical resistivity from 5.5 µΩcm, in the as-sprayed condition, to 2.1 µΩcm, after a heat treatment at 300°C. This was accompanied by a gradual decrease in hardness from 1300 MPa to 600 MPa for an annealing period of 1h while increasing the temperature from 0.27 to 0.87 T_M. They have also observed isothermal grain growth from 2 µm - 6 µm during annealing. A similar annealing procedure was studied by Meng et al. [6.7] on CS stainless steel samples between 0.25 - 0.6 T_M for a 1h duration and the results showed an increase in strength, from 67 MPa to 357 MPa, and in elongation, from 0.1% to 3%. Other works reporting annealing trials of other systems show similar trends [6.8-6.10]. In all these works, despite a gain in mechanical properties, the actual strength and ductility recorded are far from the bulk values, which justifies the need for further investigation of sintering, which is typically performed between 0.6 - 0.9 T_M, as a post-deposition process to reach near bulk mechanical properties in the CS deposit.

The lack of metallurgical bonding in CS Inconel 718, due to the lack of deformation, is the primary reason to investigate post-spraying sintering as a means of increasing strength. This family of materials is used in high temperature environments, such as land-based and jet engines, where their mechanical reliability is of critical importance. In this study, the densification occurring during sintering of porous CS samples, the evolution of the microstructure, and the gain in mechanical properties, are presented as a function of sintering parameters known for Inconel 718.

6.4. EXPERIMENTAL PROCEDURES

6.4.1. Starting Powder

Gas atomized Inconel 718 powder from Sulzer Metco (AMDRY1718) was used for this investigation. The particle size distribution, as shown in Figure 6.1, was measured using a Horiba LA-920 particle size analyzer. The average particle size was 33 μm. The starting powder composition, as provided by the manufacturer, is presented in Table 6.1.

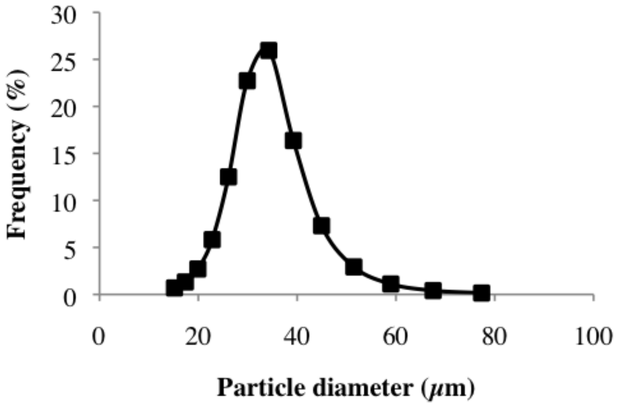

Figure 6-1 : Particle size distribution of the Inconel 718 powder

Table 6-1 : Chemical composition of the Inconel 718 powder, as provided by the supplier

	Al	B	C	Co	Cr	Fe	Nb	Ni	Mo	Ti	O
WT%	0.43	<0.006	0.05	0.09	19.11	17.92	5.07	53.07	3.13	0.94	0.02

6.4.2. Cold Spray Deposition Trials

CS was performed using a CGT Kinetiks 4000 gun (Cold Gas Technology, Ampfing, Germany), with nitrogen as the carrier gas. The powder was sprayed on a low carbon steel substrate. The stand-off distance was 60mm, the gas pressure was 35 bars, and the gas was heated to 800°C. The particle velocity was measured using a time-of-flight particle diagnostic system DPV2000 (Tecnar Automation, St-Bruno, QC, Canada). For the process parameters employed, the average particle velocity was 750 m/s, with a feeding rate of 23.7g/m, and a travel speed of 100mm/s.

6.4.3. Sintering Treatment

Stand-alone coating samples were extracted from the deposit using a slow-cutting wafering saw. The sprayed samples obtained were bars of approximately 5mm X 3mm X 1mm. Moreover, bending samples of 12mm X 1mm X 1mm were also extracted to measure flexural strength. The as-deposited samples were sintered in a vacuum furnace, equipped with a diffusion pump, at 1200, 1225, and 1250°C for 10, 60, and 180 min, respectively, employing a heating rate of 5°C/min. The samples were then furnace cooled to room temperature. Based on previous work by Anger *et al.* [6.11], this set of temperatures was estimated to be the best compromise between consolidation time and grain growth.

6.4.4. Solution and Aging Treatments

The solution and aging treatments were performed on deposits sintered at 1250°C for 60 and 180 min to evaluate any further gain in mechanical properties. Both treatments were done in a vacuum furnace with a mobile heat source, allowing for rapid cooling. The solution treatment temperature was set at 980°C and held for 60 min, followed by a rapid cooling (~400°C/min between 980°C and 600°C). The aging treatment was conducted as per AMS 5662 [6.12]. The samples were soaked at 720°C,and held for 8h, furnace cooled (50°C/hr) to 625°C and held for 8h before cooling (50°C/min) to room temperature.

6.4.5. Characterization of the sintered components

Sample preparation for metallographic observations followed the usual grinding and polishing sequence. Light Optical Microscopy (LOM) and image analysis software (Clemex) were employed to measure the porosity on unetched micrographs. The porosity was calculated from a total of 10 micrographs taken at a magnification of 200X. After etching the samples with Aqua Regia (3HCl / 1HNO_3), further observations were conducted using a Hitachi S-4700 Field Emission Scanning Electron Microscopy (SEM). The microscope was used under back-scattering mode to take advantage of the electron channeling contrast effect. Clemex image analysis software was used to measure the grain size upon sintering. Microhardness was measured using (Clark Microhardness 100AT) with 500g and 25g loads for a loading time of 15s. Each hardness measurement reported corresponds to the average of 10 or more indents on a polished surface.

Three-point bending tests were performed, both on as-sprayed and sintered samples, using a Tinius-Olsen Universal testing machine equipped with a 25 KN load cell and LVDT for displacement measurement. The sintering condition for the flexural testing was chosen according to the highest hardness obtained, corresponding to sintering at 1250°C for 1h. Three bars for each condition were tested and the reported flexural strength and strain were taken from the average of the three tests. Flexural stress was calculated from the force measurement and the sample geometry through equation 6.1:

$$\sigma_{flex} = \frac{3PL}{2bd^2} \qquad \text{eq. 6.1}$$

where σ_{flex} is the flexural stress (MPa), P is the force applied (N), L is the span between the sample supports (mm), b is the width, and d is the thickness of the sample (mm), respectively. Similarly the strain was computed from equation 6.2:

$$\varepsilon_{flex} = \frac{6Dd}{L^2} \qquad \text{eq. 6.2}$$

where ε_{flex} is the flexural strain, and D is the displacement. Analysis of the fracture surface was conducted with the SEM.

6.5. RESULTS AND DISCUSSION

6.5.1. Densification

In previous work, Marrocco *et al.* [6.13] deposited Inconel 718 by cold spray using room temperature helium gas at 29 bar stagnation pressure and a powder feedstock of 14 μm average particle size. The particle velocity achieved under these conditions was computed assuming a one-dimensional isentropic flow as modeled by many workers; the description of the models can be found in [6.14-6.16]. Once the flow properties were determined, the particle velocity was computed from the following equation 6.3:

$$m_p \frac{dv_p}{dt} = \frac{C_D A_p \rho (v - v_p)^2}{2} \qquad \text{eq. 6.3}$$

where m_p is the particle mass, v_p is the particle velocity, t is time, C_D is the drag coefficient, A_p is the cross section area of the particle, ρ is the gas density, and v is the gas velocity. The drag coefficient, for the spray conditions used in the current study, was determined by comparing the computed particle velocity to the measured particle velocity. The drag coefficient was adjusted so that the predicted particle velocity fitted the measurements. As a first approximation, the same drag coefficient was used to evaluate the particle velocity obtained by Marrocco *et al.* The modeled velocity for a 14 µm particle at the nozzle exit was found to be 760 m/s. With these conditions, the density they obtained was 97.2%. The microstructure of a representative cross-section of the as-sprayed coating from this study is shown in Figure 6.2. The density, measured by image analysis of the pore volume fraction, was 97.5%, and the pore geometry was irregular. This result is in line with the density of 97.2% obtained by Marrocco *et al*.

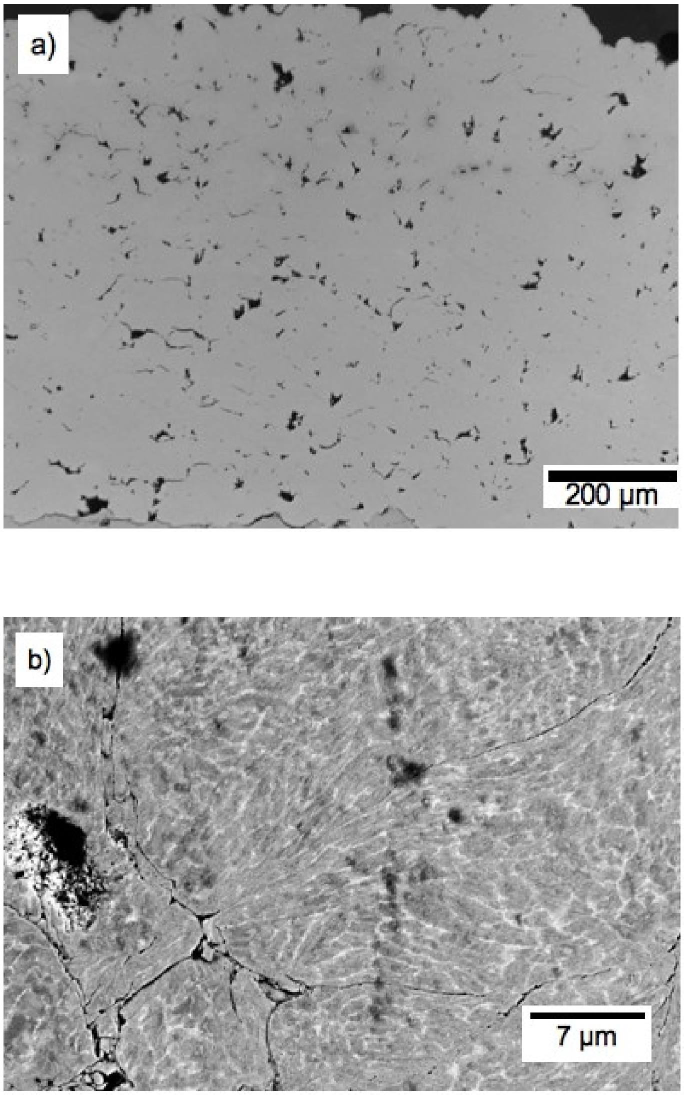

Figure 6-2 : Optical micrograph of the as-sprayed coating and (b) SEM micrograph of the as-sprayed coating showing poor interparticle bonds.

Significant consolidation occurred during the sintering treatment, as shown in Figure 6.3. From the graph in Figure 6.3a), it is noticeable that the porosity decreased to approximately 1.4% after 10 minutes of holding at 1200°C and did not change significantly with sintering time. Similar results were obtained for the 1225°C trials. The sintered density for the trials at 1250°C reached 99.8% (0,2% porosity), as shown in Figure 6.3b). Comparing Figure 6.2a) and 6.3b), it can clearly be observed that the debonded locations were consolidated. During pressureless sintering, the green compacts typically have a low density and densification causes the porous compacts to shrink until the pore structure is closed. The typical density for which the pore structure changes from open pores to closed pores lies at 93%-95%. With an initial porosity of 2.5%, the CS compact starts the sintering process with a tight pore structure and there is very limited shrinkage to occur. The unbonded interparticle regions are not spherical, thus reduction of pore surface through neck growth is enhanced because of the small curvature radius, known to increase material flux in such location. Hence the healing of the unbonded particles is fast, and consolidation reaches a stage where only rounded pores, arising from the triple junction points, remain, as depicted in Figure 6.3b). The step increase in density for the sintered samples performed at 1250°C could be linked with the formation of a transient liquid phase. Similar observation was done by Hamjrle *et al.* [6.11], who reported that the sintering rate of Inconel 718 increased when the temperature reached 1187°C, and near-full density samples were obtained when sintering for short durations at a temperature higher than 1250°C. This gain in densification was associated with the presence of a liquid phase.

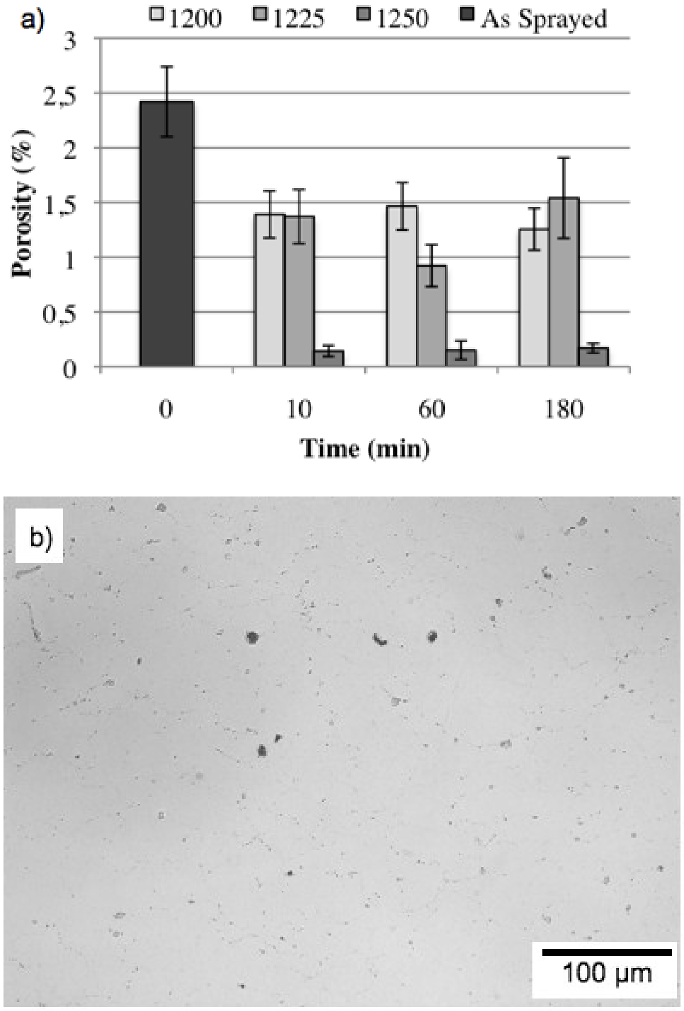

Figure 6-3 : (a) Porosity measurement of each sintering condition and (b) optical micrograph from a sample sintered at 1250°C for 60 min.

6.5.2. Microstructure evolution

The grain size was measured by image analysis to obtain the average grain size, and grain size distribution, for each sintering run. The results are presented in Figure 6.4, where the grain size is plotted against holding time for each sintering temperature (see Figure 6.4a). The grain size increases slightly as a function of time for the sintering performed at 1200°C (9.5, 11.3 and 13.9 µm) and 1225°C (12.9, 15.3 and 18.5µm), but increases steadily with time when sintering at

1250°C (18.0, 30.2 and 81.3 μm). The grain size distribution shown in Figure 6.4b) shows a shift of the mean grain size and a broadening of the distribution with time for the sintering test at 1250°C. Grain growth can be fitted to the empirical equation 6.3:

$$G - G_0 = kt^n \qquad \text{eq. 6.3}$$

where G is the grain size, G_0 is the grain size at the start of the isothermal hold, t is the time, n is the grain growth exponent, and k is a temperature dependant growth constant. The grain growth exponent, in ideal conditions, takes a value of 1/2 [6.17]. The grain growth exponent is obtained from the grain size data by plotting ln(G) vs ln(t), taking into consideration that k is constant at a given temperature, as shown in Figure 6.5. From the slope of the linear fit for the 1200°C and 1225°C sintering runs, the grain growth exponent was found to be 1/8; but, for the trials at 1250°C, it increased to 1/2. In fact, the small grain growth exponent calculated for the 1200 and 1225°C runs is expected [6.17-6.20], as equation 6.3 does not consider the presence of pinning phases at the grain boundaries. It has been observed that the grain growth exponent changes as a function of temperature, impurities, and second phase distribution [6.17-6.20]. The micrographs presented in Figure 6.6 (a-b) depict the microstructure for the sintering tests at 1200°C-60 min and 1225°C-60 min respectively. In each micrograph, small, white particles are present in the matrix as well as on grain boundaries. The precipitates were analyzed by EDS and the resulting spectrum is presented in figure 6.6c. The precipitates were found to have high niobium and titanium concentrations compared to the matrix. By comparison with similar results found in the literature, the second phases were identified as secondary MC carbides (M= Nb,Ti) [6.21-6.25]. The presence of these second phase particles at grain boundaries during sintering can slow down and stop grain growth due to the Zener pinning effect.

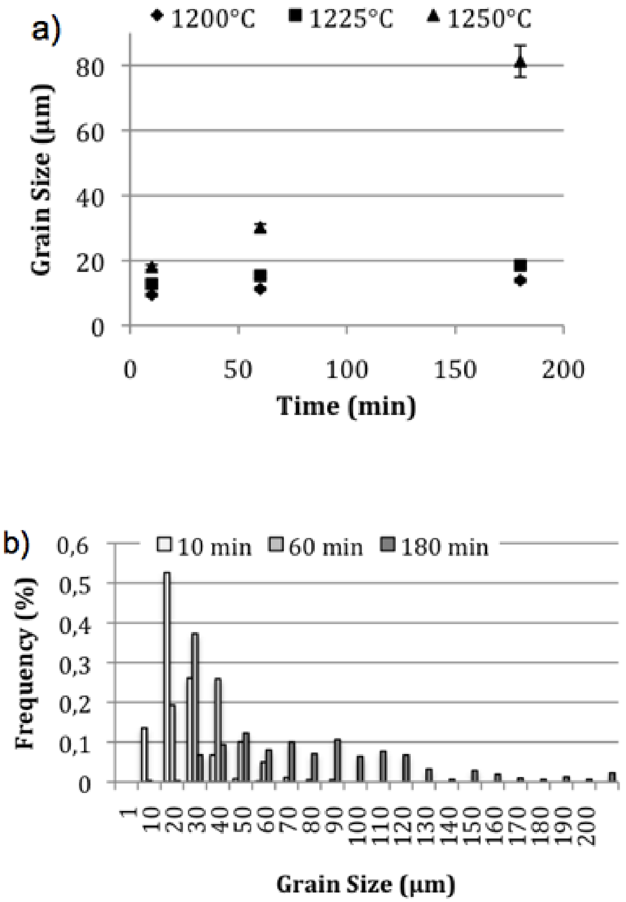

Figure 6-4 : (a) Average grain size of the sintered deposits, (b) grain size distribution of the deposit sintered at 1250°C for 10 min, 60 min, and 180 min.

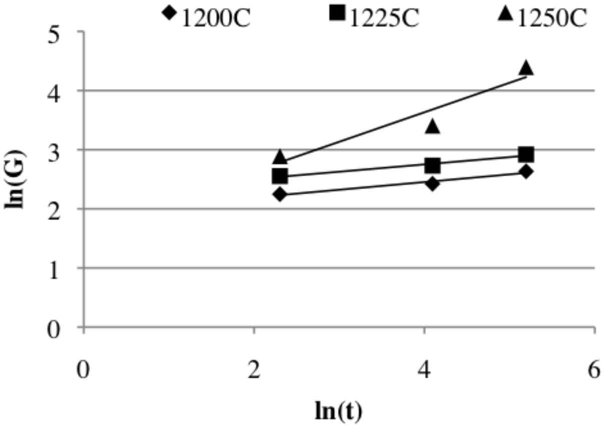

Figure 6-5 : Logarithmic plot of grain size vs time. The grain growth exponent can be found from the slope of the linear regression.

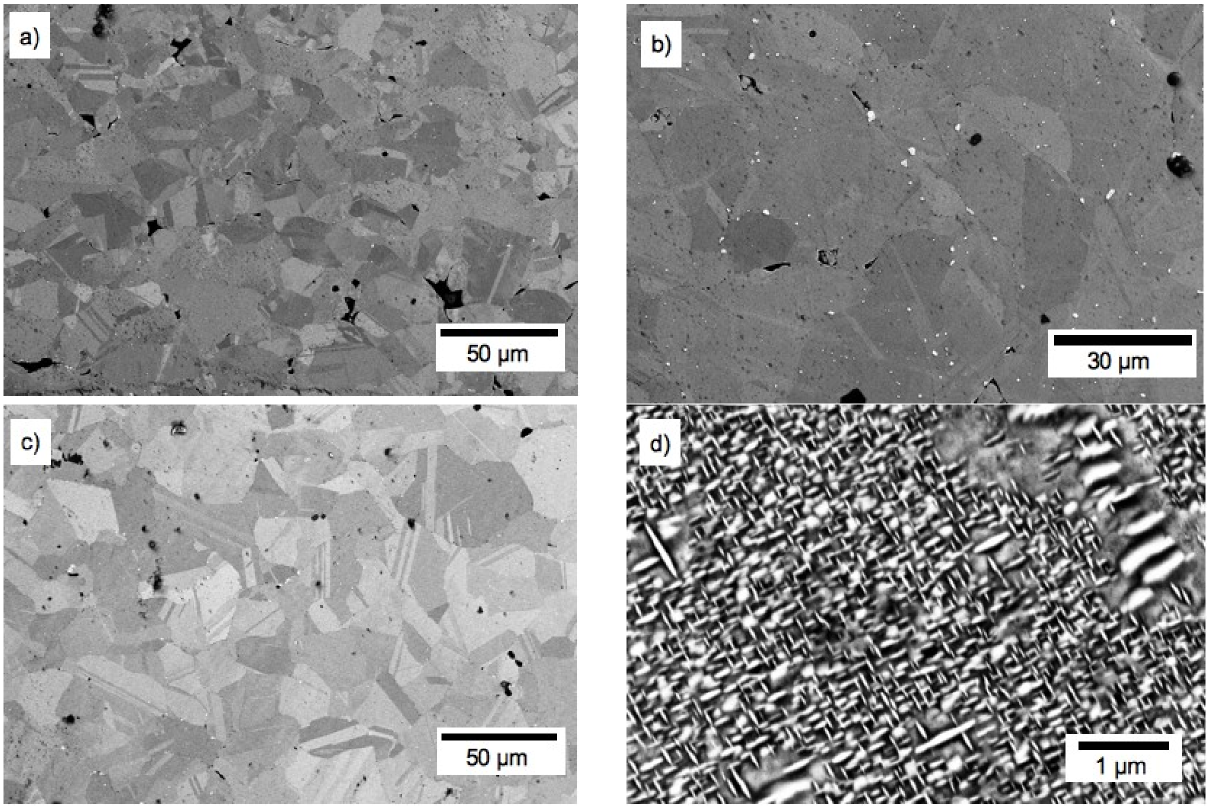

Figure 6-6 : Micrographs from Inconel 718 cold spray deposit sintered at a) 1200°C-1h; b) 1225°C-1h; c) EDS analysis of the white carbide particle; d) High magnification of the 1250°C-3h sample showing δ and γ” precipitates.

6.5.3. Second phase formation

During the heating and cooling stages of the sintering cycle, some precipitates may form which could influence the microstructure's evolution. The potential precipitates forming in Inconel 718 are the δ phase, the γ" phase, and the γ' phase, which are unlikely to modify the sintered microstructure as the solution temperature for these precipitates are 1000°C for the δ phase [6.26], and 900°C for the γ"/γ' phase [6.27]. The MC carbides, on the other hand, should be stable up to around 1250°C, and thus could form and grow during the whole sintering process [6.28]. From the micrographs shown in Figure 6.6, the variations in the amounts and sizes of carbides, as a function of the sintering condition, can be clearly observed. The measurement of the average size and volume fraction of the carbides was done by image analysis and the results are presented in Figure 6.7. As a function of time, the volume fraction of carbides increased during the sintering trials at 1200°C, remained relatively stable for the trials at 1225°C, and decreased for the 1250°C runs. The results strongly suggest that the 1250°C temperature was sufficiently high to dissolve the carbides that formed during the heating ramp of the sintering process. As a function of time, the carbide dissolution was slow; such that, after 60 min of soaking time, the carbides were still present to pin the grain boundaries. This is in good agreement with the grain growth behavior presented in Figure 6.4. For the 1200°C sintering, both the carbide volume fraction and size remained similar after 10 min and 60 min, but increased for the 180 min soak. This delayed growth suggests that the carbide growth kinetics are slow at this temperature. The 1225°C sintering results show an initial increase in carbide volume fraction and size, but no further coarsening seems to occur over 60 min of sintering. This is unexpected, as normally small precipitates dissolve and large precipitates coarsen correspondingly. No previous data on the coarsening of carbides in PM Inconel 718 could be found in the literature, but further work needs to be performed to better understand the carbide precipitation behavior and its interaction with the sintering process.

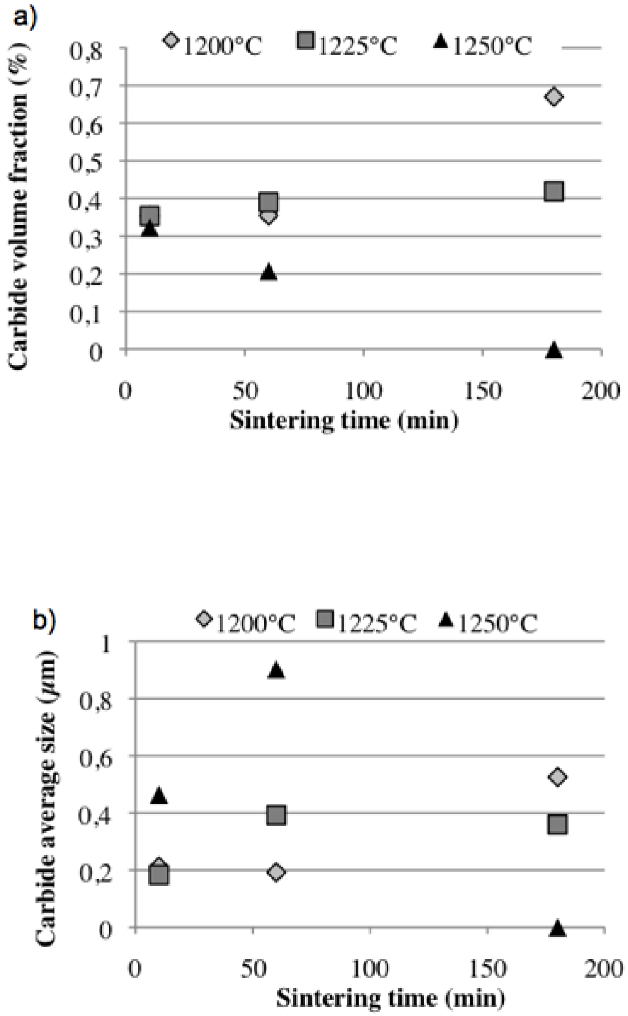

Figure 6-7 : (a) Isothermal evolution of carbide volume fraction;
(b) Isothermal coarsening of the carbides

Interestingly, in the sample sintered at 1250°C for 180 min, other niobium precipitates formed during cooling. Figure 6.6d) shows the small disk-like structure, associated with γ”, observed in this sample. The size of the precipitates at peak hardness, after a 4h aging treatment at 750°C, was reported as 30nm by Slama *et al.* [6.29]. The approximate size of the precipitates shown in Figure 6.6d) ranges between 100 and 200 nm, suggesting that the sample is in the over-aged condition. The larger plates, seen in the top right corner, are associated with δ precipitates and are surrounded by a precipitate-free zone that is typical of this alloy.

6.6. MECHANICAL PROPERTIES

6.6.1. Hardness

The Vickers hardness was measured at two different loads to differentiate between the local hardness at the particle level, and the overall hardness of the deposit, including the effect of bonding and the presence of defects. An example of the observation of the structure before and after indentation is shown in Figure 6.8. In the as-sprayed condition, the indentation under 500g load produced debonding, highlighting poor interfacial strength. On the other hand, none of the sintered coatings have shown sign of debonding after indentation.

The summary of the average hardness measurements is reported in Table 6.2 with the corresponding 95% confidence interval. The hardness of the as-sprayed coating is 516±22 HV when measured at 25g load, and drops to 423±26 HV when tested under a 500g load. This hardness reduction is explained by the formation of cracks emerging from the indenter when the load is sufficient to separate weakly bonded particles.

The 1200°C sintered samples present an increase in hardness from 399 HV to 456 HV with time for the low load measurements, while the hardness values remain statistically similar (360 HV) for the high load measurements. The samples sintered at 1225°C were found to have a statistically constant hardness around 390 HV for the low load measurement. Similarly, for the high load measurement, the hardness remains statistically similar, at around 380 HV. The small difference between the results obtained for the two tested loads is a qualitative indication that the consolidation is better than for the sintering tests performed at 1200°C. Finally, the hardness for the samples sintered at 1250°C followed the same trend as for the 1225°C samples,with respect to the difference between low load and high load measurements. However, the hardness range is higher, reaching a maximum of 466 HV after the 1h sintering before decreasing to 419 HV for the 180 min test.

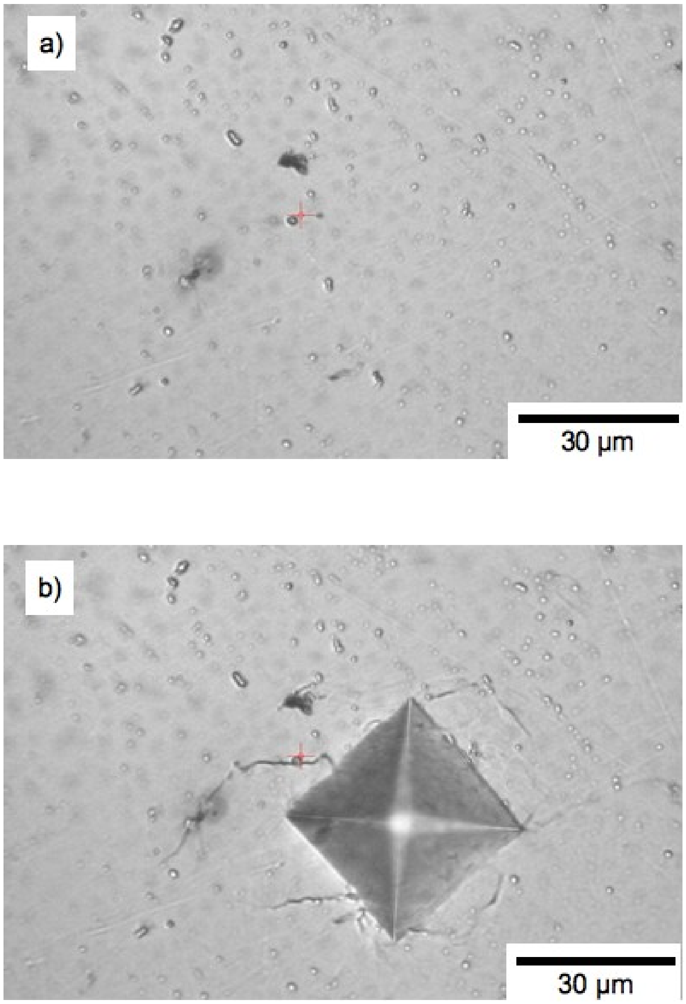

Figure 6-8: Micrograph of the as-sprayed deposit a) before and b) after indentation

To see if any gain in mechanical properties could be obtained from aging, a solution treatment and a standard aging treatment were performed on the deposits sintered at 1250°C for 60 min and 180 min. The measured hardnesses were 441±10 HV and 452±8 HV, respectively. The hardness increased slightly for the 1250°C samples sintered for 180 min, but not for the sample sintered at 1250°C for 60 min. This result is similar to the maximum hardness obtained by Slama *et al.* [6.29]; they obtained a hardness of 466 HV after aging wrought Inconel 718 for 4h at 750°C.

Table 6-2: Measured Vickers microhardness for as-sprayed, sintered and aged deposits

Sintering Temperature	Load	Hardness for each sintering time (HV)		
		10 min	60 min	180 min
1200°C	25 g	399 ± 18	414 ± 10	456 ± 15
	500 g	360 ± 25	364 ± 18	343 ± 27
1225°C	25 g	401 ± 10	378 ± 23	391 ± 14
	500 g	366 ± 20	382 ± 28	397 ± 25
1250°C	25 g	438 ± 18	466 ± 21	419 ± 13
	500 g	399 ± 12	464 ± 30	395 ± 19
1250°C + aged	25 g	-	441 ± 10	452 ± 8
	500 g	-	497 ± 11	496 ± 19
As-Sprayed	25 g	516 ± 22		
	500 g	423 ± 26		

6.6.2. Three-point bending test

The flexural strength was measured on as-sprayed and sintered samples following a sintering treatment at 1250°C for 60 min and 180 min. The results are shown in Table 6.3. As expected, the sintering of the CS samples significantly increased both the strength and ductility. For the 60 min sintering, an increase of 6.5 and 7 fold was observed for the flexural strength (from 187 to 1225 MPa) and flexural strain (from 0.026 to 0.183), respectively. This result compares well with what was achieved by Meng *et al.* using CS deposits of stainless steel where they showed an increase of 5.3 and 30 times the as-sprayed values of strength and ductility, respectively [6.7]. The samples sintered at 1250°C for 180 min reached an average flexural strength statistically similar to the 1h samples. Aging the samples further improved the strength of both the 60 min and 180 min samples by 20% and 33%, respectively, and this without affecting the ductility. However, a much larger scattering of the flexural strength values was observed for the latter sintering condition. An extraordinary aged sample had a flexural strength of 2303 MPa, which was in the range of what was reported for wrought Inconel 718 (1750-2500MPa) [6.30]. It is believed that this sample exhibited full consolidation without any residual pores known to harm the strength of PM materials. Optimizing process parameters to obtain such conditions may be complex as the control in the densification of the green compact is highly linked with the quality and homogeneity of the green compact, which may be difficult to control in a stochastic process such as CS.

Table 6-3 : Flexural strength and strain results for the sintered CS samples

	Flexural strength (MPa)	Flexural strain
As Sprayed	187 ± 41	0,026 ± 0,022
Sintered 1250-60min	1225 ± 122	0,183 ± 0,037
Sintered 1250-180min	1512 ± 207	0,161 ± 0,025
Sintered 1250-60min + aged	1475 ± 130	0,160 ± 0,046
Sintered 1250-180min + aged	1651 ± 658	0,159 ± 0,045

The fracture surfaces were observed in the SEM to analyze the nature of the failure. Figure 6.9 shows (a) a low magnification and (b) a high magnification micrograph of the fracture surface for the as-sprayed samples, respectively. In this case, the fracture surface is characterized by interparticle fracturing, for which no signs of adhesion/ductility are observed. Such a fracture surface corresponds to what is typically observed during fracturing green compacts. Figure 6.10 a) and b), and c) and d) presents comparative fracture surface micrographs for samples sintered at 1250°C for 60 min and 180 min. The sintering treatment allowed interparticle bonding, shown by the presence of numerous dimples at the prior-particle boundaries. No second phase could be identified as the primary source of the reduced strength, compared to the wrought alloy. Further examination of the fracture surface shows localized regions where clean interparticle boundaries are present (as indicated by the arrows). These regions most likely served as crack initiation sites, and are arising from the incomplete sintering cycle. These regions would most probably correspond to the larger defects present within the as-sprayed samples and for which prolonged sintering time, or slightly higher temperature, would have been necessary to reduce their influence on crack propagation, if ever possible.

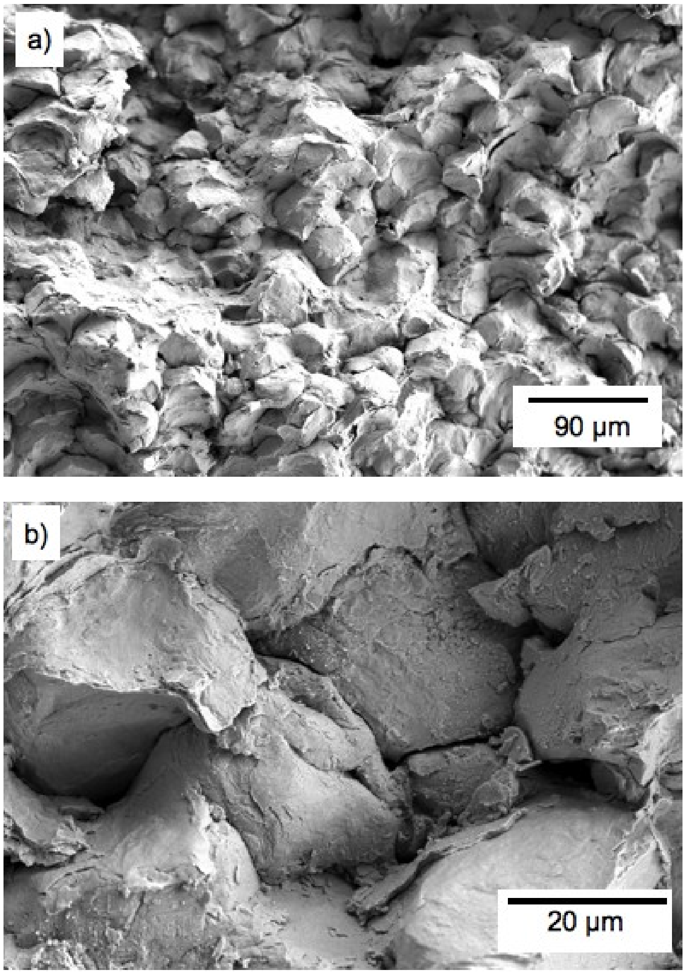

Figure 6-9 : Micrograph from the fracture surface of the as-sprayed three point bending sample at low magnification (a) and high magnification (b)

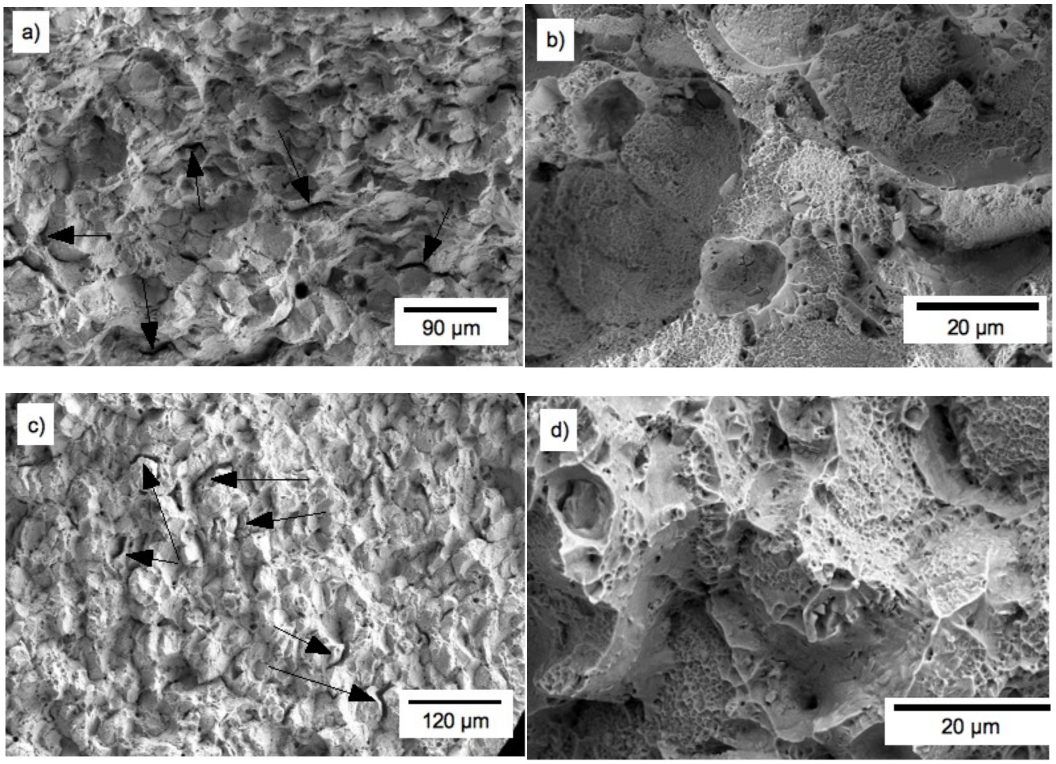

Figure 6-10 : Micrograph from the fracture surface of the three-point bending samples sintered at 1250°C for 60 min (a,b) and 180 min (c,d)

ACKNOWLEDGEMENTS

The authors would like to thank the Natural Sciences and Engineering Research Council of Canada, for their assistance in making this work possible, and the McGill Engineering Doctoral Award provided to D. Levasseur.

6.7. REFERENCES

6.1. Alkhimov, A.P., A.N. Papyrin, and V.F. Kosarev, *Gas-dynamic spraying method for applying a coating*. 1994: US.

6.2. Ajdelsztajn, L., et al., *Cold gas dynamic spraying of a high temperature Al alloy.* Surface and Coatings Technology, 2006. **201**(6): p. 2109-2116.

6.3. Eason, P.D., et al., *On the characterization of bulk copper produced by cold gas dynamic spray processing in as fabricated and annealed conditions.* Materials Science and Engineering A, 2011. **- 528**(- 28): p. 8174- 8178.

6.4. Cadney, S., et al., *Cold gas dynamic spraying as a method for freeforming and joining materials.* Surface and Coatings Technology, 2008. **202**(12): p. 2801-2806.

6.5. Assadi, H., et al., *Bonding mechanism in cold gas spraying.* Acta Materialia, 2003. **51**(15): p. 4379-4394.

6.6. Phani, P.S., V. Vishnukanthan, and G. Sundararajan, *Effect of heat treatment on properties of cold sprayed nanocrystalline copper alumina coatings.* Acta Materialia, 2007. **55**(14): p. 4741-4751.

6.7. Meng, X.-M., et al., *Influence of annealing treatment on the microstructure and mechanical performance of cold sprayed 304 stainless steel coating.* Applied Surface Science, 2011. **- 258**(2): p. 700-704.

6.8. Beffort, O., C. Solenthaler, and M.O. Speidel, *Improvement of Strength and Fracture-Toughness of a Spray-Deposited Al-Cu-Mg-Ag-Mn-Ti-Zr Alloy by Optimized Heat-Treatments and Thermomechanical Treatments.* Materials Science and Engineering a-Structural Materials Properties Microstructure and Processing, 1995. **191**(1-2): p. 113-120.

6.9. Hall, A.C., et al., *The effect of a simple annealing heat treatment on the mechanical properties of cold-sprayed aluminum.* Journal of Thermal Spray Technology, 2006. **15**(2): p. 233-238.

6.10. Li, C.J. and W.Y. Li, *Microstructure evolution of cold-sprayed coating during deposition and through post-spraying heat treatment.* Transactions of Nonferrous Metals Society of China, 2004. **14**: p. 49-54.

6.11. Hajmrle, K. and R. Angers, *Sintering of Inconel-718.* International Journal of Powder Metallurgy, 1980. **16**(3): p. 255-266.

6.12. *Metals Handbook*. 9th ed. Vol. 4. 1981, Metals Park, Ohio: American Society for Metals.

6.13. Marrocco, T., D.G. McCartney, and P.H. Shipway, *Comparison of the microstructure of Cold Sprayed and Thermally Sprayed IN718 Coatings*, in *International thermal Spray Conference*. 2006, ASM International: Seattle.

6.14. Grujicic, M., et al., *Analysis of the impact velocity of powder particles in the cold-gas dynamic-spray process.* Materials Science and Engineering: A, 2004. **368**(1-2): p. 222-230.

6.15. Marrocco, T., et al., *Production of titanium deposits by cold-gas dynamic spray: Numerical modeling and experimental characterization.* Journal of Thermal Spray Technology, 2006. **15**(2): p. 263-272.

6.16. Dykhuizen, R.C. and M.F. Smith, *Gas Dynamic Principles of Cold Spray.* Journal of Thermal Spray Technology, 1998. **7**(2): p. 205-212.

6.17. Hillert, M., *On Theory of Normal and Abnormal Grain Growth.* Acta Metallurgica, 1965. **13**(3): p. 227-238.

6.18. Randle, V. and D. Horton, *Grain growth phenomena in nickel.* Scripta Metallurgica et Materialia, 1994. **31**(7): p. 891-895.

6.19. Grey, E.A. and G.T. Higgins, *Solute limited grain boundary migration: A rationalisation of grain growth.* Acta Metallurgica, 1973. **21**(4): p. 309-321.

6.20. Grest, G.S., D.J. Srolovitz, and M.P. Anderson, *Computer simulation of grain growth,ÄîIV. Anisotropic grain boundary energies.* Acta Metallurgica, 1985. **33**(3): p. 509-520.

6.21. Kirman, I. and Warringt.Dh, *Precipitation of Ni3nb Phases in a Ni-Fe-Cr-Nb Alloy.* Metallurgical Transactions, 1970. **1**(10): p. 2667-2675.

6.22. Cozar, R. and A. Pineau, *Morphology of Y' and Y'' Precipitates and Thermal-Stability of Inconel 718 Type Alloys.* Metallurgical Transactions, 1973. **4**(1): p. 47-59.

6.23. Sundararaman, M., P. Mukhopadhyay, and S. Banerjee, *Some Aspects of the Precipitation of Metastable Intermetallic Phases in Inconel-718.* Metallurgical Transactions a-Physical Metallurgy and Materials Science, 1992. **23**(7): p. 2015-2028.

6.24. Rao, G.A., M. Srinivas, and D.S. Sarma, *Effect of solution treatment temperature on microstructure and mechanical properties of hot isostatically pressed superalloy Inconel*718.* Materials Science and Technology, 2004. **20**(9): p. 1161-1170.

6.25. Hajmrle, K., R. Angers, and G. Dufour, *Phase analysis of sintered and heat treated alloy 718.* Metallurgical Transactions A, 1982. **- 13 A**(1): p.5 - 12.

6.26. Azadian, S., L.Y. Wei, and R. Warren, *Delta phase precipitation in Inconel 718.* Materials Characterization, 2004. **53**(1): p. 7-16.

6.27. Sundararaman, M., P. Mukhopadhyay, and S. Banerjee, *Precipitation of the Delta-Ni3nb Phase in 2 Nickel-Base Superalloys.* Metallurgical Transactions a-Physical Metallurgy and Materials Science, 1988. **19**(3): p. 453-465.

6.28. Knorovsky, G., et al., *INCONEL 718: A solidification diagram.* Metallurgical and Materials Transactions A, 1989. **20**(10): p. 2149-2158.

6.29. Slama, C., C. Servant, and G. Cizeron, *Aging of the Inconel 718 alloy between 500 and 750 degrees C.* Journal of Materials Research, 1997. **12**(9): p. 2298-2316.

6.30. Chang, S.H., et al., *Evaluation of HIP pressure on Inconel 718 superalloy.* International Journal of Cast Metals Research, 2006. **19**(3): p. 181-187.

CHAPTER 7. EFFECT OF HEATING RATE ON THE PRESSURELESS SINTERING DENSIFICATION OF A NICKEL BASED SUPERALLOY

D. Levasseur and M. Brochu

Mining and Materials Engineering Department, McGill University, 3610 University Street, Montreal, Canada, H3A 0C5

7.1. PREFACE

After considering the effect of green density on Inconel 718 pressureless sintering process, the third objective of this thesis was to study the effect of heating rate. Chapter 7 reports Inconel 718 pressureless sintering results obtained with various heating rates. The analysis of the sintering data (density and grain size) through the Master Sintering Curve model is used to highlight the effect of heating rate during supersolidus liquid phase sintering. Since liquid phase formation has a strong influence on the densification of this alloy, the effect of heating rate on liquation is addressed. This manuscript conclusion is presented in Chapter 10 with the conclusions from the other manuscripts inserted in this thesis.

This manuscript was submitted to Metallurgical and Materials Transactions A (2015)

7.2. ABSTRACT

Pressureless sintering of Inconel 718 has important technological applications for the densification of metal injection molding or additive manufacturing of parts with powder/binder systems. The effect of heating rates ranging from 15 to 200 K/min on the sintering behavior of fine (-325 mesh) Inconel 718 powders was studied using the master sintering curve (MSC) concept. A pressureless pulsed electric current sintering setup was used to heat samples. The temperature at the onset of sintering increased as the heating rate increased. The formation of a supersolidus liquid fraction was shifted toward higher temperatures for increased heating rates.

The apparent activation energy of sintering was obtained by least squares fitting of the sintering data to the MSC and was in good agreement with the lattice diffusion activation energy of the alloying elements present in Inconel 718. The MSC followed different kinetics for low heating rates (≤50 K/min) and high heating rates (≥75 K/min), and these differences were related to liquation kinetics.

7.3. INTRODUCTION

Inconel 718 is a nickel-based superalloy that is widely used in hot zones of land-based turbines as well as in jet engines [7.1]. Among the existing manufacturing routes for this alloy, powder metallurgy (PM) is advantageous as it yields a low buy-to-fly ratio for complex-shaped parts. Unfortunately, Inconel 718 is hard to sinter to full density owing to its high strength at high temperatures; accordingly, it requires high sintering temperatures and pressure-assisted processes [7.2]. Metal injection molding (MIM) with Inconel 718 is used to produce green parts that can be sintered to densities exceeding 97%. Full density is achieved after a hot isostatic pressing treatment [7.3-7.5]. Based on previous studies on the sintering of MIM Inconel 718, the powder particle size varies from a D_{50} of 10 to 22 µm and sintering temperatures vary between 1533 and 1573 K, with a holding time of 1 to 6 h [7.3-7.8]. The reported mechanical properties of the sintered, hot isostatic pressed and aged parts are summarized in Table 7-1.

The reduced strength and elongation of Inconel 718 PM parts compared to cast or wrought parts can be explained by their lower density and the presence of brittle second phases, such as Laves phase and MC carbides that form during sintering [7.5]. Özgün *et al*. [7.5] have studied the effect of microstructure on mechanical properties of sintered Inconel 718 MIM parts. They highlighted the unusually high volume fraction of MC carbides that form due to carbon pickup from the binder used to produce MIM green parts. The formation of MC carbides is associated with scavenging of the second-phase forming elements, such as Ti and Nb, which precipitate as γ' ($Ni_3(Al,Ti)$) and γ'' (Ni_3Nb) and confer beneficial mechanical properties at high temperatures (up to 923 K). As depicted in the mechanical properties shown in Table 7-1, the production of Inconel 718 MIM parts with mechanical properties close to those of wrought parts necessitates hot isostatic pressing post-treatment. The achievement of full density directly after sintering would improve the properties of sintered materials. In this study, a wide range of heating rates were used to study the densification and microstructure evolution of Inconel 718 sintered parts based on the master sintering curve concept to assess the optimal sintering conditions for the direct production of Inconel 718 PM parts.

Table 7-1: Summary of published data on the sintering of Inconel 718 MIM parts

Mechanical properties of sintered Inconel 718 at room temperature

Author	**Process**	**Density (g/cm^3)/(%TD)**	**YS (MPa)**	**UTS (MPa)**	**EL (%)**	**Grain size (μm)**	**Reference**
Wohlfromm *et al.*	MIM + HT	7.99 (97.2%)	840	1259	21	NA	[4]
	MIM+HIP+HT	8.19 (99.6%)	908	1340	23	NA	[4]
Valencia *et al.*	MIM	8.2 (98.7%)	NA	NA	NA	28	[3]
	MIM+HT	8.21 (98.9%)	1062	1238	11,4	NA	[3]
	MIM+HIP	8.26 (99.5%)	1133	1350	14.2	25.6	[3]
Davies *et al.*	MIM	NA	503	936	20	<15	[6]
	MIM+HT	NA	1046	1211	6	<15	[6]
Schmees *et al.*	MIM+HIP+HT	NA	1139	1350	14.1	NA	[7]
Youhua *et al.*	MIM	98%	876	1054	25.4	NA	[8]
	MIM+HT	98%	1124	1304	8.7	NA	[8]
	MIM+HIP	100%	824	1009	39.3	NA	[8]
	MIM+HIP+HT	99.90%	1078	1250	21.7	NA	[8]
Özgün *et al.*	MIM	97.30%	506	667	5.8	20–30	[5]
	MIM+HT	97.30%	780	1022	5.3	NA	[5]
	Cast	8.22	915	1090	11		[9]
	Wrought	8.22	1185	1435	21		[9]
	AMS 5662M-2009 Min Requirements		1034	1241	12		[10]

7.3.1. Master Sintering Curve

The master sintering curve (MSC) concept is a useful framework to predict pressureless sintering behavior from experimental densification data [7.11]. The MSC analysis was developed by Su and Johnson to model the pressureless sintering behavior of metals and ceramics using the apparent activation energy from a few dilatometer densification tests performed at different heating rates. Considering that only a single dominant diffusion mechanism is active during sintering, equation 7.1 can be used to predict changes in density over time during sintering.

$$\frac{d\rho}{3\rho dt}=\frac{\gamma\Omega(\Gamma(\rho))D_0}{kT(G[\rho])^n}\exp\left(-\frac{Q}{RT}\right) \qquad \text{eq. 7.1}$$

where ρ is the relative density, t is time, γ is the surface energy, Ω is the atomic volume, Γ is the lumped scaling parameter as described by Hansen *et al.* [7.12], D_0 is the appropriate diffusion constant (grain boundary or lattice diffusion), k is the Boltzmann constant, T is temperature, G is grain size, n = 3 for lattice diffusion and 4 for grain boundary diffusion, R is the gas constant, and Q is the apparent activation energy of sintering. If the lumped scaling parameter and grain size are functions of density alone, then equation 7.1 can be reorganized and integrated as follows:

$$\frac{k}{\gamma\Omega D_0}\int_{\rho_0}^{\rho}\frac{(G(\rho))^n}{3\rho\Gamma(\rho)}d\rho=\int_0^t\frac{1}{T}\exp\left(-\frac{Q}{RT}\right)d \qquad \text{eq. 7.2}$$

where ρ_0 represents the green density. The terms in equation 7.2 can be arranged to separate the material properties on the left-hand side from Q and the temperature-time data on the right-hand side as follows:

$$\Phi(\rho)=\Theta(t,T(t)) \qquad \text{eq. 7.3}$$

where $\Phi(\rho)$ includes all the material-related parameters except for Q, and $\Theta(t,T(t))$ is the "thermal work" term, which can be integrated by numerical methods from the temperature profiles of different sintering tests or from dilatometer curves. Once the apparent activation energy of sintering is determined empirically, a single function can be used to predict the density as a function of thermal work.

However, a drawback of the MSC model is that it considers only a single sintering mechanism responsible for shrinkage. The activation energy of this mechanism is related to the activation energy for diffusion, which is usually proportional to the amount of grain boundary diffusion and lattice diffusion that occurs within the system. A shift in sintering mechanism can then be readily observed, as it would change the MSC parameter and apparent activation energy. The development of an MSC analysis would permit postulations regarding the effectiveness of high heating rate sintering cycles for the processing of Inconel 718 PM parts.

7.4. EXPERIMENTAL METHOD

The prealloyed gas-atomized powder feedstock (low oxygen content and spherical morphology) used in this study was AMDRY 1718 supplied by Oerlikon (formerly Sulzer Metco; Winterthur, Switzerland). The chemical composition of the powder, as provided by the supplier, is presented in Table 7. 2.

Table 7-2 : Chemical analysis of the AMDRY 1718 powder

	Al	C	Co	Cr	Fe	Nb	Ni	Mo	Ti	O
wt%	0.43	0.05	0.09	19.11	17.92	5.07	53.07	3.13	0.94	0.02

The powder size distribution was characterized by a laser interferometer; the geometric mean particle size was 33 μm and geometric standard deviation was 8 μm.

The compacts were prepared by slip casting based on a procedure developed by Hamjrle and Anger [7.13]. Following this procedure, they obtained carbon contamination ranging from 100 to 300 ppm [7.14]. The powder was mixed with a solution of ammonium alginate, slip cast, and dried for at least 24 h. The slip cast compacts were cut into cubes of 5 × 5 × 5 mm. The binder was removed from the green compacts in a vacuum furnace (2×10^{-4} torr) at 788 K for 30 min and then furnace cooled. Assuming a theoretical density (TD) of Inconel 718 of 8.22 g/cm^3, the initial density of the binder-less compacts was 61 ± 3% TD based on the Archimedes method. The compacts were then sintered in the pulsed electric current sintering equipment with a custom pressureless die assembly inspired by Bradbury and Olevsky [7.15], as shown in Figure 7-1.

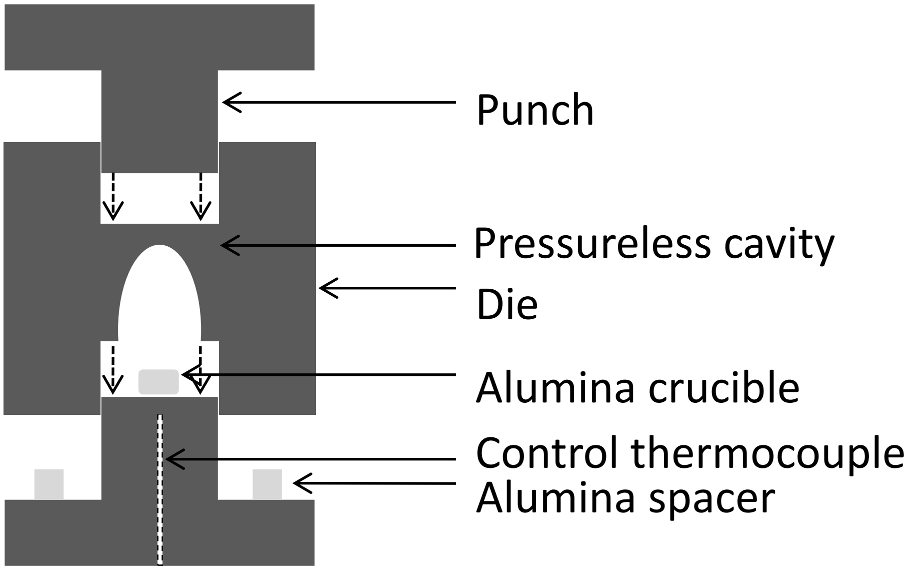

Figure 7-1: Assembly used for pressureless sintering in the pulsed electric current sintering (PECS) apparatus.

The sample was set in an open alumina crucible in the graphite die assembly and sintered in a Thermal Technologies 10-3 SPS press. The control thermocouple was set in the lower punch 2 mm below the sample chamber. The pressure applied to the die assembly was 5 MPa to ensure good electrical contact, which was only sustained by the graphite insert forming the sample chamber. The true temperature of the sample was corrected for each heating rate by calibrating the process temperature against the melting temperature of pure copper and pure nickel for various heating rates.

The sintering of the binder-less compacts was performed at heating rates of 15, 25, 50, 75, 100, and 200 K/min. Interrupted tests were used to build a density-temperature curve for each heating rate to mimic a dilatometer trace. At the tested temperature, the power was turned off and the sample was cooled to room temperature within 10 min, with an initial cooling rate of approximately 300 K/min. Within 1 min, the temperature dropped to below 70% of the T_m of Inconel 718, at which point sintering is negligible. The sample density was measured by the Archimedes method. Metallographic analysis was performed by cutting with a low-cutting-speed wafering blade, cold mounting, and impregnation in epoxy before grinding with 600 grit SiC paper and polishing with 9 µm, 1 µm, and colloidal silica solutions on appropriate cloths. Grain size was evaluated by an image analysis (Buehler OmniMet, Lake Bluff, IL, USA) of light optical micrographs (Nikon Eclipse LV150; Tokyo, Japan) for samples etched with a solution consisting of 10 ml of HNO_3, 5 ml of glacial acetic acid, and 85 ml of H_2O under 1.5 V for 8 s. The porosity measurements were performed by image analysis with Clemex software (Longueuil, Canada) for images obtained using a light optical microscope (Olympus, Tokyo, Japan) at 50X magnification using a mosaic picture of cross-sections of a polished sample.

7.5. RESULTS

7.5.1. Densification experiments

The densification plots for all sintering experiments are shown in Figure 7-2. The sintering densification curves for all sets of experimental data followed a classical sigmoidal shape and were thus fitted to a sigmoidal curve using equation 7.4. As shown in Figure 7-3, the second derivative of the sigmoidal curve was computed to determine the onset temperature for densification for each heating rate. As expected, the densification onset temperature increased as the heating rate increased, but a discontinuity (i.e., a dip) in the curve was observed for heating rates of 75 and 100 K/min. The observed dip in densification onset temperature could indicate a change in sintering mechanism that could be visualized through the MSC analysis. Hereafter, two densification regimes will be presented, i.e., low (15–50 K/min) and high (75–200 K/min) heating rates.

$$y = A_2 + \frac{(A_1 - A_2)}{\left(1 + \exp\left((x - x_0)/dx\right)\right)} \qquad \text{eq. 7.4}$$

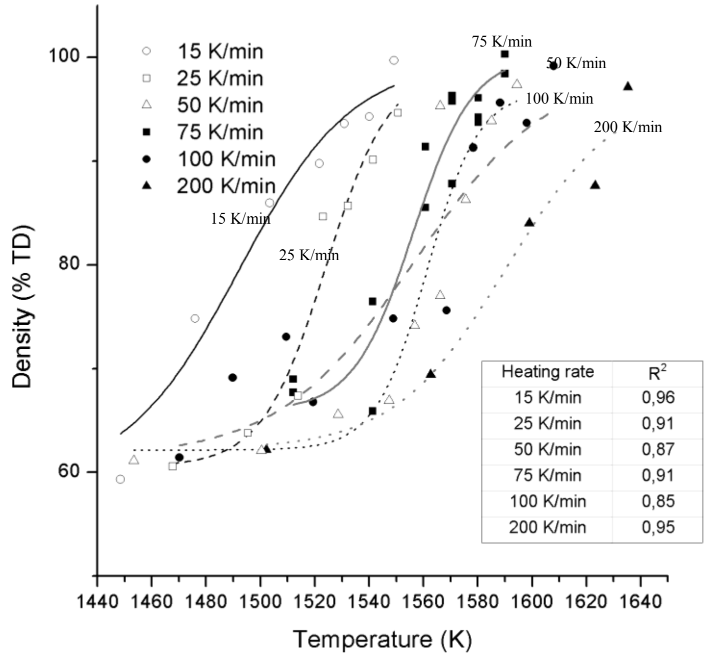

Figure 7-2: Sintering data fitted with sigmoidal curves for heating rates of 15 K/min, 25 K/min, 50 K/min, 75 K/min, 100 K/min, and 200 K/min.

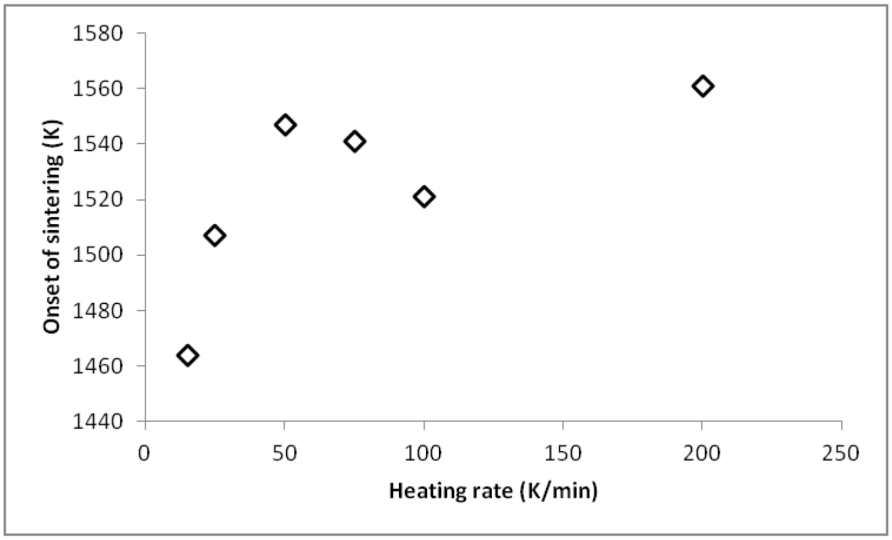

Figure 7-3: Onset temperature of densification for each heating rate experiment.

7.5.2. Assessment of porosity distribution

Intrinsic heat conduction within the porous compact could create large thermal gradients from the surface to the core when high heating rates are used. Garcia *et al.* [7.16] studied the effect of high heating rates during alumina sintering and showed that a thermal gradient between the surface and the material bulk created a sintering front that was analogous to a solidification front. This phenomenon produced a porosity gradient that is referred to as a “core-shell structure.” This is easily observed as the compact surface approaches full density, while the core remains close to the green density. The Biot number expressed in equation 7.5 was used to evaluate temperature gradients in the compact.

$$Bi = hL/k \qquad \text{eq. 7.5}$$

where h is the heat transfer coefficient, L is the characteristic length of the body, and k is the thermal conductivity of the body. When the Biot number is larger than 1, a thermal gradient between the surface and the core of the compact exists.

The observed temperature difference between the thermocouple placed in the graphite punch below the sample and the calibrated temperature of the compact is 250 K for a 200 K/min heating rate. The calculated radiation heat transfer coefficient over the compact surface is used to compute the Biot number for samples with a heating rate of 200 K/min, assuming a conductivity of 6 W/m/K, and taking into account the initial 40% void fraction and the increase of conductivity as the temperature increases [7.17]. The Biot number was 0.21 for the sample sintered at 1635 K for a heating rate of 200 K/min. The other samples are bound to have smaller Biot numbers since the thermal gradients between the sample and the die walls are lower for the other conditions (i.e., lower heating rates). As the Biot number is less than one, the temperature of the compact can be considered homogeneous during the heating ramp.

The absence of a core-shell structure was experimentally verified by measuring the porosity gradient from the surface to the center of the compact sintered up to 1635 K at 200 K/min, as shown in Figure 7-4. The porosity was between 3.18% and 4.15%; however, there was no sign of a porosity gradient.

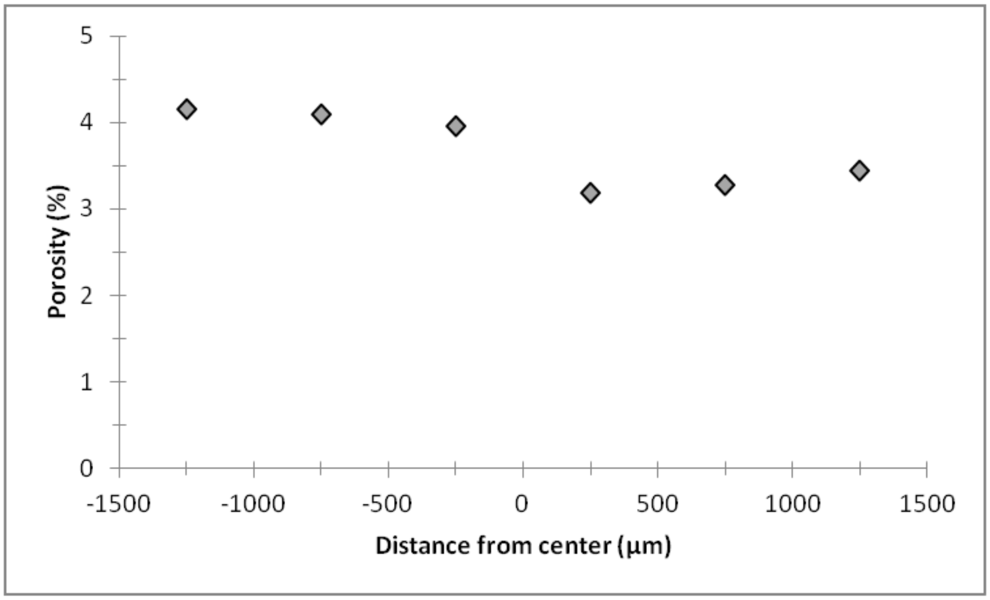

Figure 7-4: Porosity measurement across the 200 K/min compact sintered at 1635 K.

7.5.3. Assessment of grain size evolution

An assumption of the MSC analysis is that grain size is only dependant on density. In most sintering cases, this assumption is largely met. Park *et al.* introduced a grain growth master curve to their MSC analysis to extend the model applications to cases of exaggerated grain growth or substantial surface diffusion [7.18]. The validity of this assumption for Inconel 718 was assessed using experimental measurements of the grain size distribution for all sintering conditions used in the study.

The grain size distribution of samples was measured by an image analysis using optical microscopy of etched samples, and a representative micrograph is shown in Figure 7-5. The average grain size is plotted against density in Figure 7-6 for each heating rate. The error bars represent the 99% confidence interval computed from the grain size distribution for each sample. Two observations can be extracted from this graph. First, the average grain size was not statistically significantly different between the low and high heating rates for all densities. Second, the average grain size never surpassed the average powder particle size of 33 µm. Accordingly, within the current experimental conditions, the grain size distribution was a function of density only, consistent with the MSC assumption described above.

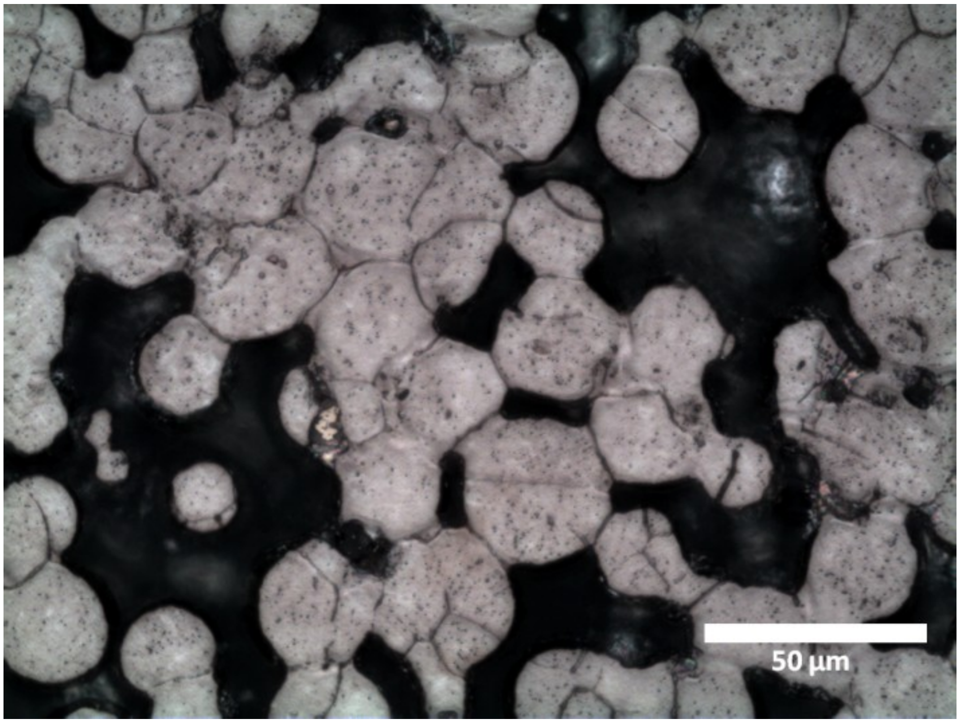

Figure 7-5: Micrograph from an etched sample sintered at 1476 K at 15 K/min

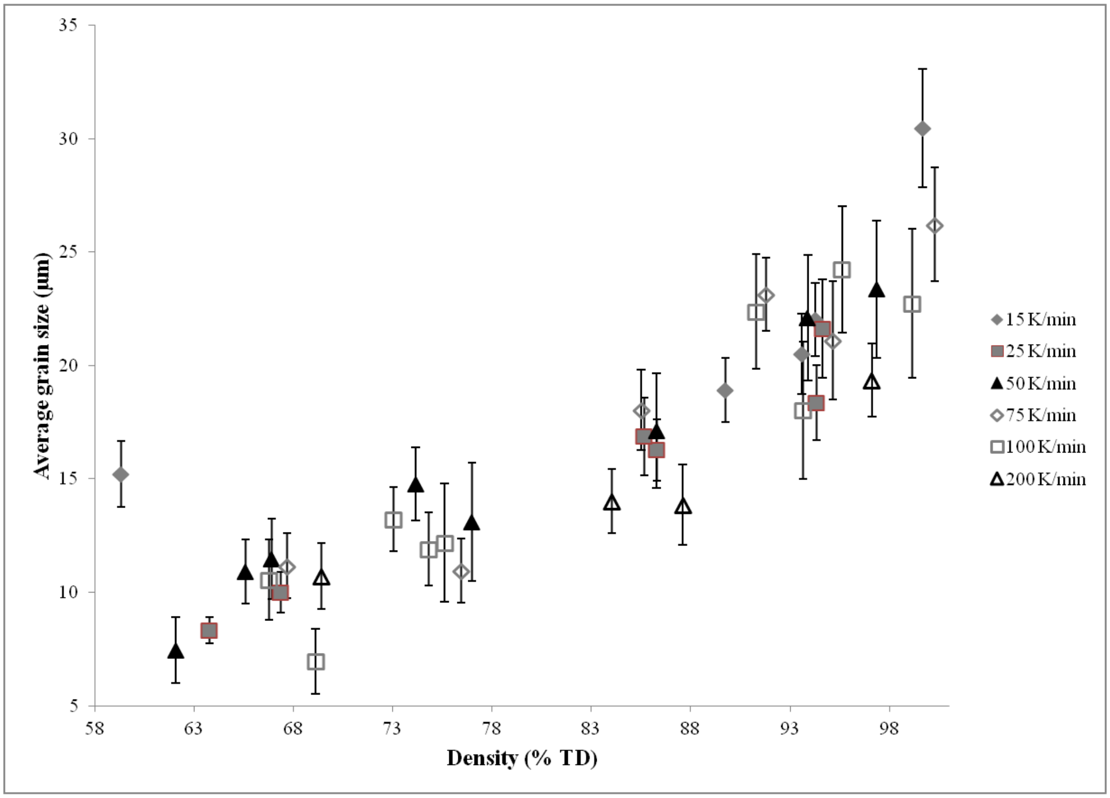

Figure 7-6: Average grain size evolution with respect to density plotted for each heating rate used in this study; error bars represent the 99% confidence intervals around each value.

7.5.4. Assessment of microstructure evolution

Microstructure observations revealed the formation of a liquid phase during high-temperature excursions, i.e., greater than 1513 K. The micrographs presented in Figure 7-7 show the liquid phase observed for each heating rate. The liquid fraction was evaluated by image analysis for several samples and these data are presented in Figure 7-8 with the onset temperature of sintering identified for each heating rate. However, conditions that presented low liquid fractions and low densities could not be analyzed owing to the difficulty of sorting liquation zones from non-wetted grain boundaries. Except for at 75 K/min, the liquid fraction increased with temperature for all heating rates.

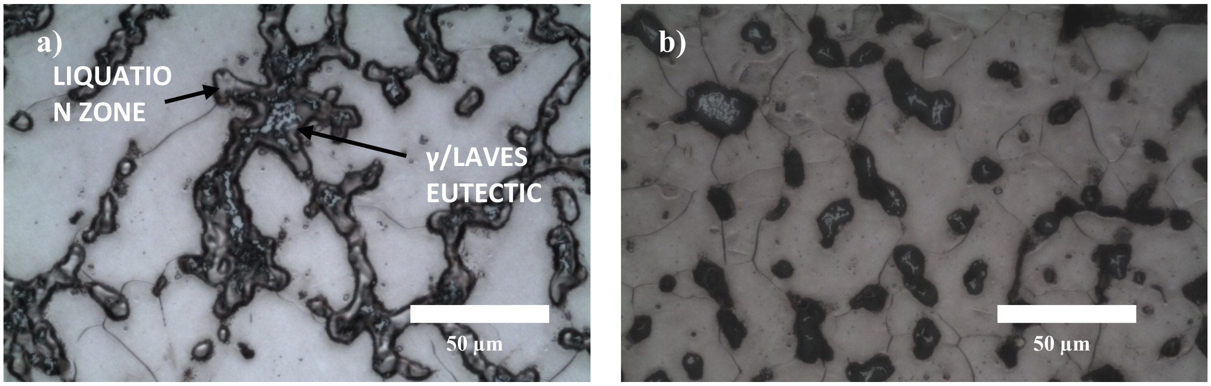

Figure 7-7: Optical micrograph of the liquation zone and γ/Laves eutectic for the samples sintered at a) 15 K/min at 1549 K and b) 200 K/min at 1635 K.

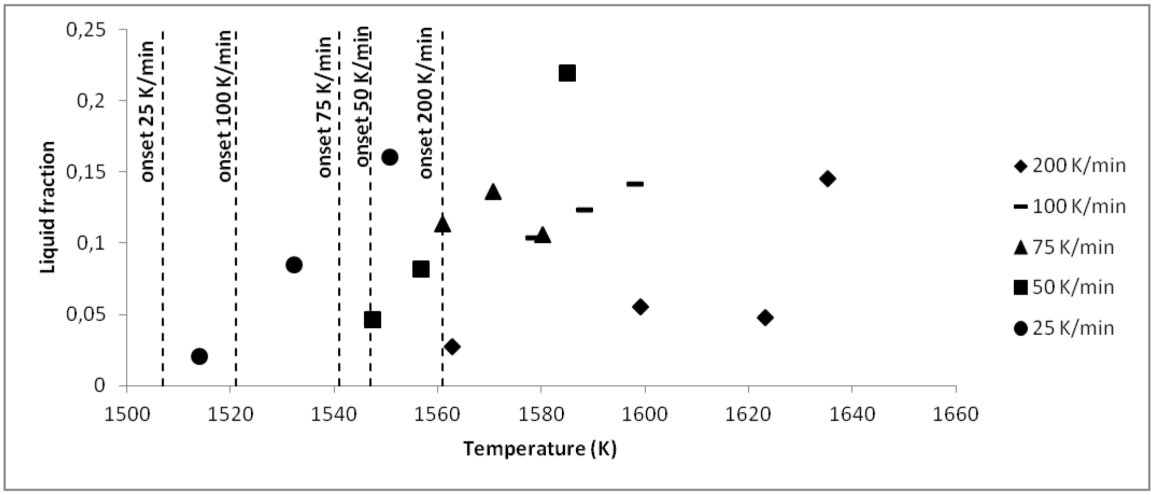

Figure 7-8: Measured liquid fractions of several sintered Inconel 718 samples for heating rates from 25 K/min to 200 K/min. The liquid fraction observed is compared with the calculated onset temperature of sintering identified for each heating rate.

In the samples sintered at over 1540 K, there was a eutectic morphology that can be distinguished from the surrounding liquation zone. This morphology has been observed by Antonsson and Fredriksson and is associated with the γ/Laves eutectic reaction [7.19]. The temperature of the first occurrence of the liquid phase for each heating rate is plotted in Figure 7-9. The temperature at which liquation was first observed was ~1520 K for heating rates of 15 and 25 K/min, 1547 K for 50 K/min, ~1563 K for 75 and 100 K/min, and 1562 K for 200 K/min.

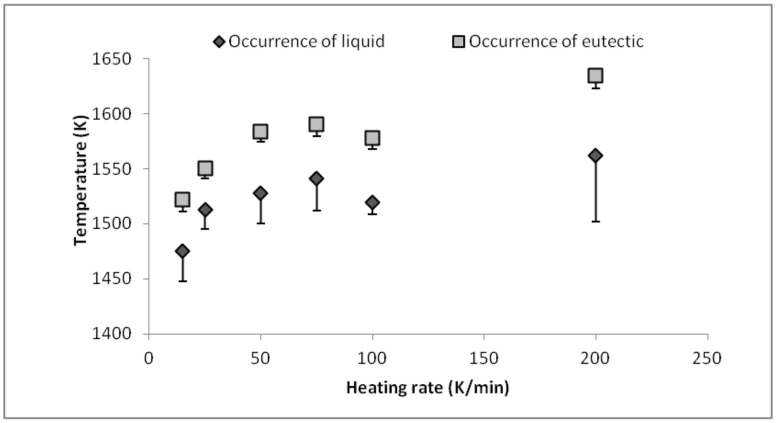

Figure 7-9: Temperature of the first observation of liquid phase and γ/Laves eutectic formation for each heating rate. The error bars indicate the highest temperature sample in which no liquid or eutectic was observed.

Figure 7-10 presents the results of an EDS analysis of a γ/Laves eutectic zone in the sample sintered at 200 K/min and 1635 K. The niobium concentration profile of the matrix, the liquation zone, and the eutectic zone were qualitatively assessed. As expected, the niobium content was higher in the eutectic zone and lower in the liquation zone adjacent to the eutectic region. This observation confirms that the eutectic is a γ/Laves phase [7.19].

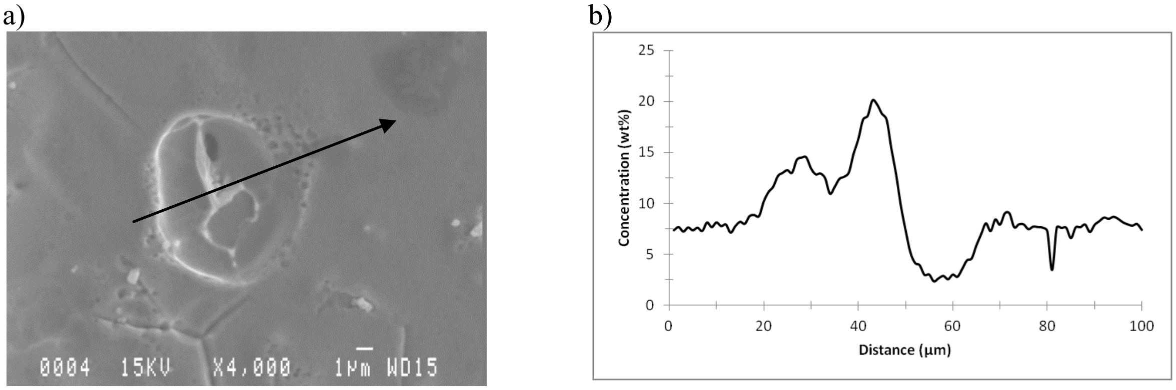

Figure 7-10: EDS linescan of the eutectic zone (a), the liquation zone (the arrow shows the region analyzed) (b) linescan Nb profile.

7.5.5. Determination of Q and MSC fit

The low and high heating rate sintering curves were analyzed using the MSC methodology described in the Introduction. The data for both solid-state and liquid-state sintering were considered in the analysis to obtain the apparent activation energy of sintering that describes the entire sintering cycle. The onset temperature of sintering (Figure 7-3) was equal to or higher than the temperature of liquation (Figure 7-9) for all heating rates, except the lowest one (15 K/min). The samples sintered at 15 K/min showed no detectable sign of liquid before 1475 K (75% TD); however, the onset of sintering for this heating rate occurred at 1464 K (65% TD). Since the liquid phase in this sample formed between 1450 and 1475 K, it is reasonable to assume that densification largely occurs in the transient liquid phase regime and that the apparent activation energy is valid if similar liquation conditions are obtained.

The apparent activation energy of sintering was determined by the minimization of residuals between the constructed MSC and the sigmoidal curve fit obtained with equation 7.4. The residuals for the MSC at low and high heating rates were computed for a range of *Q* and are shown in Figure 7-11.

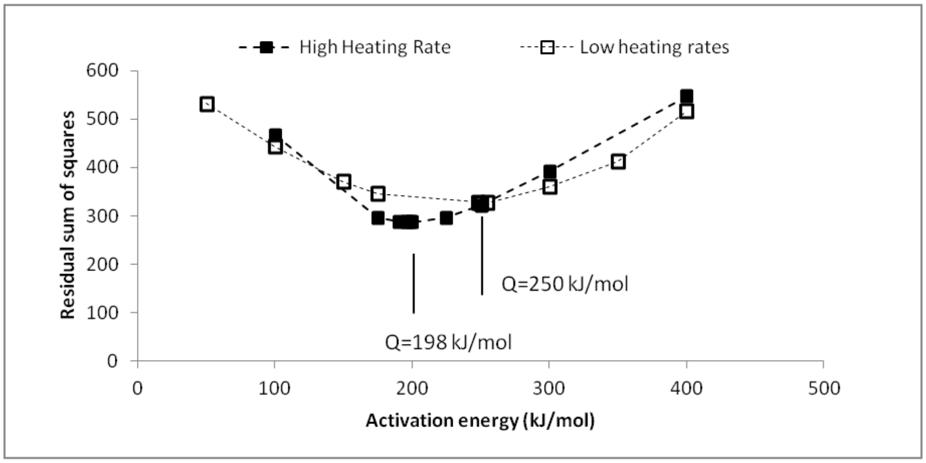

Figure 7-11: Residual plot for different values of *Q* for the low heating rate master sintering curve (MSC) (left) and the high heating rate MSC (right).

The apparent activation energy resulting in the lowest residual for the MSC at the low heating rate was 250 kJ/mol. The apparent activation energy value that minimized the residuals of the MSC for high heating rates was 198 kJ/mol. These activation energies were not significantly different based on a test of variance (F-test) to compare the 95% confidence limits for Q. The similarity in activation energy for the low and high heating rates does not however indicate similar MSC behavior, as will be discussed in the next section.

The thermal work integral shown on the right-hand side of equation 7.2 is very sensitive to the apparent activation energy of sintering. Typically, the apparent activation energy of sintering is related to the atomic motion mechanism: surface, boundary, or lattice diffusion. In the case of solid-state sintering, these mechanisms are responsible for material transport from the particles to the pores. Liquid-phase sintering relies on capillary forces, particle sliding, and pore filling to achieve densification [7.20]. Liquid-phase sintering behavior is related to the liquid fraction and distribution in the compacted powder (grain size, density, liquid film thickness, and dihedral angle). Thus, the apparent activation energy for liquid-phase sintering should be related to the liquid-state and solid-state diffusion activation energy in proportion to the liquid volume fraction. The diffusion of eutectic forming species and the liquid-state diffusion of nickel should be considered in the apparent activation energy for liquid-phase sintering. The liquid-state diffusion activation energy for nickel is 38–42 kJ/mol [7.21-7.22] and the activation energy for the lattice diffusion of the main alloying elements composing Inconel 718 is given in Table 7-3. Niobium is the main eutectic former, and solid-state diffusion followed by the development of the liquid phase is believed to be the most effective sintering mechanism; accordingly, solid-state diffusion is the limiting factor in the entire sintering cycle, and the activation energy should be close to the corresponding solid-state diffusion energy of Nb in Ni, i.e., 202 kJ/mol. Therefore, the apparent activation energy of sintering observed for high heating rates (198 kJ/mol) was used to compare the MSC for the low and high heating rates shown in Figure 7-12.

Table : 7-3 : Lattice diffusion activation energy of the principal chemical constituents of Inconel 718 in nickel

Element	Q (kJ/mol)	Ref
Ni	285	[7.23]
Al	268	[7.24]
Ti	257	[7.24]
Fe	282	[7.24]
Cr	283	[7.25]
Nb	202	[7.26]

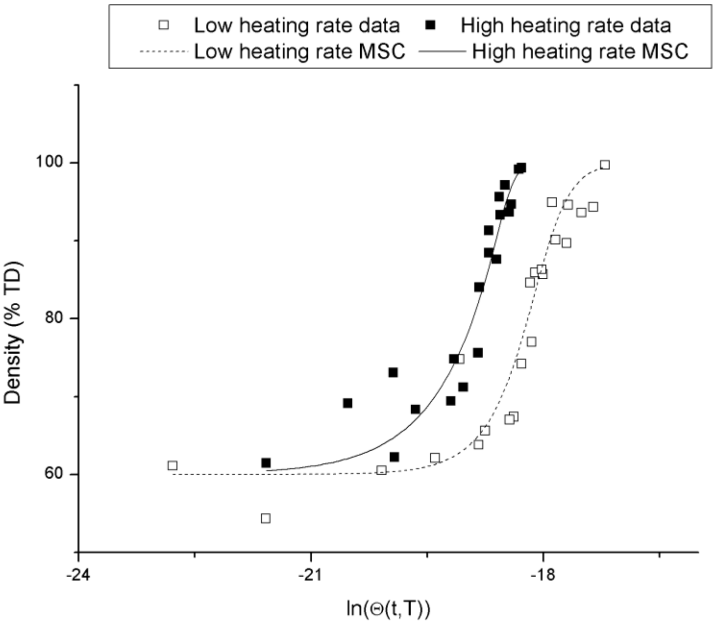

Figure 7-12: MSC for Inconel 718 powders sintered in a non-contacting pulsed DC field with an apparent activation energy of 198 kJ/mol for the low and high heating rates.

7.6. DISCUSSION

Since the work of Hamjrle *et al.* [7.13-7.14], it has been suggested that a liquid phase contributes to the sintering of Inconel 718. The liquid phase forms at temperatures between 1435 and 1485 K based on dilatometer measurements performed at 0.23 K/min [7.13].

The solidification path of Inconel 718 has been described by various authors [7.19, 7.27-7.30]; however, the eutectic reactions and formation temperatures measured during Inconel 718 heating vary markedly among studies, and the temperature ranges are presented in Table 7-4.

Table : 7-4 : Melting and solidification events for Inconel 718

$L \rightarrow \gamma$ + Laves	L + NbC $\rightarrow$ γ + Laves	$L \rightarrow \gamma$ + NbC	Solidus	Liquidus
1422 K – 1450 K	1433 K	1498 K – 1594 K	1503 K – 1593 K	1613 K – 1637 K

The liquation temperature reported by Hajmrle *et al.* [7.13] agrees with the γ/Laves eutectic temperature of 1422–1450 K. The results presented in Figure 7-7 confirm that a supersolidus liquid phase forms during sintering and Figure 7-9 shows the temperatures at which the liquid phase was first observed. The liquation temperature for the 15 K/min samples agrees with the results reported by Hajmrle *et al.*; however, the liquation temperature for heating rates of 25 K/min and higher increase to ~1503–1563 K, while the reported solidus temperature is 1503–1593 K. The heating rate influences the liquation kinetics; heating rates of less than 15 K/min promote low-temperature γ/Laves eutectic melting and heating rates of greater than 25 K/min promote higher melting point events, such as those of the γ/NbC eutectic and solidus.

Liquation is also responsible for the formation of secondary phases (NbC, Laves) at grain boundaries when the sintered compact cools from its processing temperature. The niobium concentration for γ/Laves eutectic formation is 22% as compared to 19% for γ/NbC eutectic formation. The niobium concentration in Inconel 718 is ~5.5% wt. However, its reported partition coefficient of 0.29–0.41 [7.19, 7.27, 7.31] favors segregation. Under the high cooling rate obtained in levitation casting (10^3–10^4 K/s), a γ-dendritic structure solidified with ~2% Nb in solution, while the interdendritic region contained 16% Nb [7.19]. Similar cooling rates are obtained in gas atomization, for which it is common to obtain values of 10^3 to 10^6 K/s, depending on particle size [7.32]. Assuming that the niobium concentration is similar in the gas-atomized powder structure and the levitation cast samples mentioned above, the γ/Laves eutectic cannot form upon reheating without niobium diffusion from the dendrite core to the interdendritic region. Therefore, upon reheating, Laves phase formation is related to diffusion kinetics and soaking time at the eutectic reaction temperature.

The diffusion distance is proportional to $\sqrt{Dt}$, where D represents the diffusion coefficient and t is time. Table 7-5 shows the results of 1D diffusion calculations, which were performed to evaluate the diffusion distances when the Nb concentration reaches the γ/NbC eutectic composition (19%) at the eutectic temperature (1498 K).

Table 7-5 : Diffusion depth of Nb at 1498K for heating rates of 15K/min to 200 K/min

Heating rate (K/min)	15	25	50	75	100	200
Diffusion distance (m)	1,27E-05	9,80E-06	6,92E-06	5,65E-06	4,90E-06	3,47E-06

***The diffusion coefficient of Nb in Inconel 718 was taken as 0.3exp(-35800/T), the initial Nb concentration of the NbC and matrix was taken as 0.87 and 0.025 respectively [7.28].*

The Nb diffusion analysis highlights the difference in niobium diffusion depth between the 15 K/min (12.7 μm) and 200 K/min heating rates (3.47 μm). A larger diffusion distance is associated with an increase in the volume of eutectic compound formed at low heating rates. As shown in Figure 7-9, the temperature of liquid phase occurrence was ~1475 K at heating rates of 15 K/min, and 1513–1563 K for rates of 25–200 K/min. Liquation at ~1513–1563 K is within the temperature range of both the γ/NbC reaction and solidus, but is higher than the γ/Laves eutectic temperature (1422–1450 K). The microstructure did not show the Laves phase until 1522, 1550, 1584, 1590, 1578, and 1635 K for heating rates of 15, 25, 50, 75, 100, and 200 K/min, respectively. This indicates that the niobium concentration did not reach the γ/Laves eutectic composition at the heating rates used in this study and that liquation occurred for a local niobium concentration of less than 22%.

The γ/Laves eutectics for samples sintered at 1522–1635 K formed during the solidification of the liquid fraction at the relatively slow cooling rate (5 K/s) obtained at the end of the sintering run. The lag between the Laves phase and liquation indicates that a critical liquid fraction is necessary for its formation. Laves phase formation depends on Nb microsegregation during solidification, which is directly related to the solidification velocity, length scale, and solidification time, as shown in equation 7.6 [7.31]:

$$MSI \propto \frac{\overline{V} R_f^3}{t_f} \quad , \qquad \text{eq. 7.6}$$

where MSI represents a qualitative microsegregation factor, $\overline{V}$ is the solidification velocity, R_f is the length scale, and t_f is the solidification time. At a very small length scale, microsegregation is negligible, but as the liquid pool increases in radius, microsegregation increases. This could explain the occurrence of the Laves phase only for the samples with the highest temperature for each heating rate studied.

The MSC is used to predict the sintering of powders of the same nature, geometry, and green density with different thermal cycles. For a given thermal cycle, this model allows the use of a single master curve to calculate the final density of the compact; however, modifications of the underlying sintering mechanism require a different MSC. The sintering of Inconel 718 at heating rates of over 50 K/min require less thermal work than that at lower heating rates, while the apparent activation energy is similar for all heating rates. A single MSC was not appropriate for the whole range of heating rates studied.

The cause of the observed relationship between heating rate and the densification of Inconel 718 cannot be attributed to thermal gradient or grain size differences, as evidenced by the data presented in Sections 7.5.2 and 7.5.3. The physical and geometrical constants used in the MSC model (left-hand side of equation 7.3) were the same; accordingly, the model cannot explain, in its current state, the effect of heating rate on the sintering of Inconel 718. However, the sintering mechanism is not only solid-state diffusion, but also includes the effect of a supersolidus liquid phase. In fact, most sintering occurs in the presence of the liquid phase, as evidenced by the onset temperatures of sintering and the occurrence of liquid. Only the samples sintered at a heating rate of 15 K/min could possibly include solid state sintering, when the onset of sintering occurred at 1464 K and liquation was only observed at 1475 K. The liquid phase formation kinetics were empirically shown to require less thermal work at heating rates of ≥75 K/min than

≤50 K/min. This suggests the addition of a liquid fraction term to the MSC for the analysis of liquid-phase sintering, at least for non isothermal conditions. The MSC concept was adapted by Bollina *et al.* to analyze the supersolidus liquid-phase sintering of stainless steel 316 with boron addition [7.33]. Their analysis involved the fitting of three separate regions of the densification curve with interpolation of the fitting equations between regions to closely match the supersolidus liquid-phase sintering densification data. However, the limited number of densification data points in the present study was not sufficient to use this method. Moreover, the low and high heating rate densification curves were satisfactorily separated with their respective sigmoidal curves.

Since thermal work is the time integral of temperature, the kinetics of liquation can be assessed by comparing the liquid fraction obtained at a given thermal work for low heating rates and high heating rates. Figure 7-13 presents the measured liquid fraction as a function of the thermal work term from the MSC computed at an apparent activation energy of 198 kJ/mol. The separation of the MSC into two curves (see Figure 7-12) reflects the difference in liquation kinetics between the 15–50 and 75–200 K/min rates. The liquid fraction increases with thermal work and the formation of the supersolidus liquid phase typically occurs at lower values of thermal work for high heating rates, as seen by the shift toward lower thermal work for all but one of the high heating rate data points in Figure 7-13. However, additional phenomena linked to the presence of liquid could have contributed to a reduction in the thermal work needed for densification at high heating rates. The diffusion coefficient of Nb in Inconel 718 liquid phase was estimated to be 10^{-9} m^2/s compared to 10^{-12} m^2/s for solid state diffusion according to Nastac and Stefanescu [7.31]. The liquid phase is a more efficient diffusion phase and will decrease the apparent activation energy of sintering, a phenomenon also observed by Park *et al.* [7.34]. In addition to the enhanced liquid phase diffusivity, the capillary force exerted by the liquid at particle boundaries and pore filling also contribute to densification. The observation that an increased sintering heating rate was associated with an increase in the temperature at which liquation occurs indicates that the liquid equilibrium Nb composition and the local Nb distribution at a microscale were functions of heating rate for a given liquid fraction. In turn, this shifted the kinetics of liquid formation towards lower thermal work values at high heating rates. This inclusive liquefaction phenomenon is believed to be the main cause of the MSC shift towards lower thermal work values for heating rates of ≥75 K/min than ≤50 K/min.

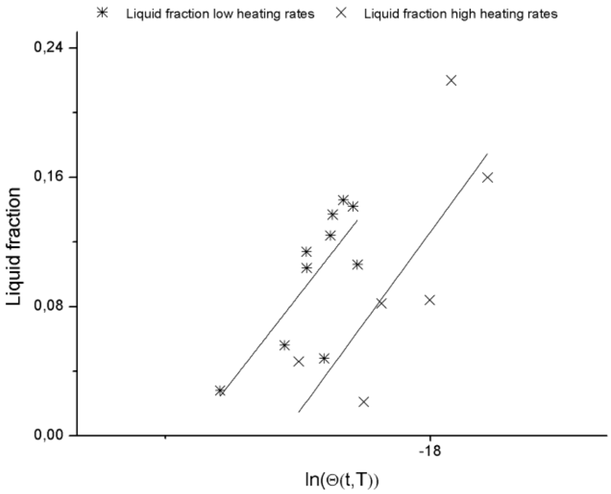

Figure 7-13: Liquid fraction as a function of thermal work for low and high heating rates.

ACKNOWLEDGEMENTS

The authors would like to thank the Natural Sciences and Engineering Research Council of Canada, for their assistance in making this work possible, and the McGill Engineering Doctoral Award provided to D. Levasseur.

7.7. REFERENCES

7.1. Geddes, B., H. Leon, and X. Huang, *Superalloys alloying and performance*. 2010, ASM International: Materials Park, Ohio. p. xii, 176 p.
7.2. Gessinger, G.H., *Powder metallurgy of superalloys*. Butterworths monographs in materials. 1984, London ; Boston: Butterworths. 348 p.
7.3. Valencia, J.J., J. Spirko, and R. Schmees, *Sintering effect on the microstructure and mechanical properties of alloy 718 processed by powder injection molding.* Superalloys 718, 625, 706 and Various Derivatives, 1997: p. 753-762.

7.4. Wohlfromm, H., et al., *Metal Injection Moulding of Nickel-based Superalloys for High Temperature Applications.* Proceedings Euro PM2003 Congr. Exhib., 2003. 3: p. 207-215.

7.5. Özgün, O., et al., *Microstructural and mechanical characterization of injection molded 718 superalloy powders.* Journal of Alloys and Compounds, 2013. 576: p. 140-153.

7.6. Davies, P., et al., *Metal Injection Moulding of Heat Treated Alloy 718 Master Alloy.* Proc. Int. Powder Met., Chicago June, 2004.

7.7. Schmees, R., J.R. Spirko, and J. Valencia. *Powder injection molding (PIM) of Inconel 718 aerospace components*. in *Proceedings of the Advanced Particulate Materials & Processes*. 1997.

7.8. Youhua, H., et al., *Preparation and Mechanical Properties of Inconel718 Alloy by Metal Injection Molding.* Rare Metal Materials and Engineering, 2010. 39(5): p. 775-780.

7.9. Donachie, M.J. and S.J. Donachie, *Superalloys : a technical guide*. 2nd ed. 2002, Materials Park, OH: ASM International, 439 p.

7.10. International, S.A.E., *AMS5662M*, in *AMS 5662M* 2009.

7.11. Su, H.H. and D.L. Johnson, *Master sintering curve: A practical approach to sintering.* Journal of the American Ceramic Society, 1996. 79(12): p. 3211-3217.

7.12. Hansen, J.D., et al., *Combined-Stage Sintering Model.* Journal of the American Ceramic Society, 1992. 75(5): p. 1129-1135.

7.13. Hajmrle, K. and R. Angers, *SINTERING OF INCONEL-718.* International Journal of Powder Metallurgy, 1980. 16(3): p. 255-266.

7.14. Hajmrle, K., *Forgeage d'ébauches poreuses d'Inconel 718 préparées par coulage en moule poreux et frittage*. 1978, Université Laval: p. 413

7.15. Bradbury, W.L. and E.A. Olevsky, *Production of SiC-C composites by free-pressureless spark plasma sintering (FPSPS).* Scripta Materialia, 2010. 63(1): p. 77-80.

7.16. Garcia, D.E., D. Hotza, and R. Janssen, *Building a Sintering Front through Fast Firing.* International Journal of Applied Ceramic Technology, 2011. 8(6): p. 1486-1493.

7.17. Sweet, J.N., E.P. Roth, and M. Moss, *Thermal-Conductivity of Inconel-718 and 304 Stainless-Steel.* International Journal of Thermophysics, 1987. 8(5): p. 593-606.

7.18. Conrad, H. and D. Yang, *Effect of the strength of an AC electric field compared to DC on the sintering rate and related grain size of zirconia (3Y-TZP).* Materials Science and Engineering a-Structural Materials Properties Microstructure and Processing, 2013. 559: p. 591-594.

7.19. Park, S.J., et al., *Master sintering curve for densification derived from a constitutive equation with consideration of grain growth: Application to tungsten heavy alloys.* Metallurgical and Materials Transactions A: Physical Metallurgy and Materials Science, 2008. 39(12): p. 2941-2948.

7.20. Antonsson, T. and H. Fredriksson, *The effect of cooling rate on the solidification of INCONEL 718.* Metallurgical and Materials Transactions B-Process Metallurgy and Materials Processing Science, 2005. 36(1): p. 85-96.

7.21. Fang, Z.Z., *Sintering of advanced materials : fundamentals and processes*. Woodhead Publishing in materials. 2010, Oxford ; Philadelphia, PA: Woodhead Publishing, 483 p.

7.22. Pottlacher, G., et al., *Thermophysical properties of solid and liquid Inconel 718.* Thermochimica Acta, 2002. 382(1-2): p. 255-267.

7.23. Hirano, K., et al., *Diffusion in Cobalt-Nickel Alloys.* Journal of Applied Physics, 1962. 33(10): p. 3049-3054.

7.24. Swalin, R.A., *University Microfilm Publication No. 10043*, Ann Arbor, Michigan.

7.25. Murarka, S.P., R.P. Agarwala, and M.S. Anand, *Diffusion of Chromium in Nickel.* Journal of Applied Physics, 1964. 35(4): p. 1339-1341.

7.26. Patil, R.V. and G.B. Kale, *Chemical diffusion of niobium in nickel.* Journal of Nuclear Materials, 1996. 230(1): p. 57-60.

7.27. Knorovsky, G.A., et al., *Inconel-718 - a Solidification Diagram.* Metallurgical Transactions a-Physical Metallurgy and Materials Science, 1989. 20(10): p. 2149-2158.

7.28. Luo, X., et al., *Theoretical analysis of grain boundary liquation in heat affected zone of Inconel 718 alloy. Study of laser weldability of Ni-base superalloys (3rd report).* Welding research abroad, 2002. 48(1): p. 16-24.

7.29. Fayman, Y.C., *Microstructural Characterization and Elemental Partitioning in a Direct-Aged Superalloy (Da-718).* Materials Science and Engineering, 1987. 92: p. 159-171.

7.30. Cao, W.D. in *Superalloys 718, 625 and Various Derivatives*. 1991. Warrendale, PA.

7.31. Nastac, L. and D.M. Stefanescu, *Macrotransport-solidification kinetics modeling of equiaxed dendritic growth .2. Computation problems and validation on INCONEL 718 superalloy castings.* Metallurgical and Materials Transactions a-Physical Metallurgy and Materials Science, 1996. 27(12): p. 4075-4083.

7.32. Duflos, F. and J.F. Stohr, *Comparison of the Quench Rates Attained in Gas-Atomized Powders and Melt-Spun Ribbons of Co-Base and Ni-Base Super-Alloys - Influence on Resulting Microstructures.* Journal of Materials Science, 1982. 17(12): p. 3641-3652.

7.33. Bollina, R., S.J. Park, and R.M. German, *Master sintering curve concepts applied to full-density supersolidus liquid phase sintering of 316L stainless steel powder.* Powder Metallurgy, 2010. 53(1): p. 20-26.

7.34. Park, S.J., et al., *Densification behavior of tungsten heavy alloy based on master sintering curve concept.* Metallurgical and Materials Transactions a-Physical Metallurgy and Materials Science, 2006. 37A(9): p. 2837-2848.

CHAPTER 8. SPARK PLASMA SINTERING OF INCONEL 718

D. Levasseur and M. Brochu

Mining and Materials Engineering Department, McGill University, 3610 University Street, Montreal, Canada, H3A 0C5

8.1. PREFACE

The fourth objective described in Chapter 3 was to investigate the microstructure obtained after pressure assisted sintering of Inconel 718 by Spark plasma sintering (SPS). The role of green density (Chapters 5 and 6) and the role of heating rate (Chapter 7) already defined the liquid phase quantity and distribution as the most important parameters that influence the final density and microstructure. The following chapter presents the effect of pressure on supersolidus liquid phase sintering of Inconel 718 and shows how the final microstructure is influenced by the sintering parameters through the liquid phase formation. As for the previous result chapters, the conclusion was truncated from this manuscript and placed in the Conclusion chapter (Chapter 10) along with the conclusions from Chapters 5, 6 and 7.

Submitted in Metallurgical and Materials Transactions B (2015)

8.2. ABSTRACT

Spark plasma sintering is investigated as an alternative to avoid the necessary encapsulation of Inconel 718 powders for the production of near-net-shape parts via the direct hot isostatic pressing sintering route. The study develops an understanding of the sintering mechanism within the temperatures interval of 900°C and 1200°C, and reports evolution of densification and associated microstructure. The effect of pressure and heating rate is also investigated. It is shown that Inconel 718 densifies only in the presence of liquid, appearing first at 1100°C. However, full density was only achieved at 1200°C with minimum of 150 sec holding time. Prior particle

boundary carbides are found in samples sintered over 1100°C and are linked with the liquid phase formation.

8.3. INTRODUCTION

Inconel 718 is one of the most used nickel based superalloys in the aerospace and power generation industry [8.1] because of its good strength at high temperature, corrosion resistance, oxidation resistance and weldability. The alloy transformation processes involving either casting or thermomecanical forming requires extensive machining and welding operations. Nickel alloys are notoriously difficult to machine due to their high strain rate sensitivity, low and elevated temperature high strength, abrasive carbides, chemical affinity with many tool materials [8.2], driving the need for near-net-shape processes such as powder metallurgy (PM). Potential gains regarding energy consumption, production cycle time and material yield has been stimulating Inconel 718 PM process development since the 1960's [8.3].

Inconel 718 was shown to be a good candidate for both powder injection molding (PIM) process [8.4-8.8] and sintering under pressure by hot isostatic pressing (HIP) of encapsulated powder [8.9-8.11]; the later being the most direct process since PIM parts require a final HIP consolidation step. However, the production cycle of Inconel 718 PM parts could be shortened even more through the spark plasma sintering (SPS) process. This sintering process involves the concurrent application of uniaxial pressure and pulsed direct current heating to rapidly consolidate powder materials. Indeed, several authors reported sintering nickel or nickel alloys powders to near full density (>98%) using SPS in less than 10 minutes [8.12-8.15].

The SPS process can achieve heating rates up to 800°C/min because of the current induced Joule heating in the die assembly and powder bed. Different studies on the SPS process have shown two main effects of the heating mechanism and associated heating rates. First, the uniformity of Joule heating strongly depends on the current distribution in the compacted powder and die assembly [8.14, 8.16-8.20]. In fact, the uneven current distribution between the die and the powder (conductive or non-conductive) was shown to generate a macroscopic thermal gradient from the center of the powder to the die wall. The temperature increase of electrically conductive powders is higher than the surrounding graphite die, which leads to a temperature difference that could influence the sintering behavior. Second, the sintering mechanism is affected by the heating rate magnitude [8.12, 8.21-8.23]. Olevsky *et al.* [8.22] showed from constitutive modeling that heating rate played a major role in promoting grain boundary diffusion densification mechanism over low temperature surface diffusion mechanism, which is responsible for pore coarsening and grain growth. Thus, explaining the many observations that crystalline materials microstructures resulting from the SPS process had limited grain coarsening. The retention of small grains in the final sintered microstructure is beneficial to the alloy mechanical properties.

The selection of powder and SPS parameters mostly relies on trial and error because of the lack of theoretical understanding on the sintering mechanism active during this process. Thus there is a strong demand for the development of process parameters for different alloy systems and in particular for Inconel 718. An effort is made in this work both to develop a theoretical understanding of Inconel 718 SPS densification mechanism; and to develop process parameters for the rapid production of dense powder metallurgy Inconel 718 parts.

8.4. EXPERIMENTAL

Gas atomized Inconel 718 prealloyed powder was used in this study (Sulzer Metco, AMDRY1718). The powder composition as supplied by the manufacturer is found in Table 8.1. The particle size distribution was measured by laser scattering (Horiba LA-920) and the cumulative distribution is presented in Figure 1 along with the values of the powder d_{10}, d_{50} and d_{90}.

Table 8-1 : Inconel 718 powder composition

Elements	Al	B	C	Co	Cr	Fe	Nb	Ni	Mo	Ti	O
WT%	0.43	<0.006	0.05	0.09	19.11	17.92	5.07	53.07	3.13	0.94	0.02

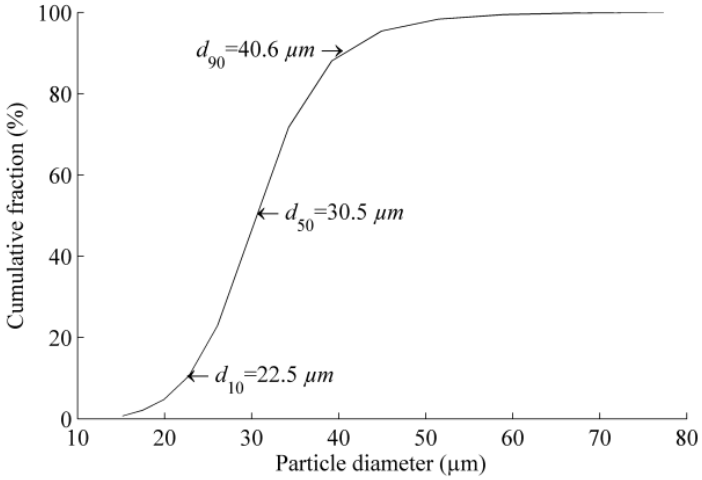

Figure 8-1 : Inconel 718 particle size distribution measured by laser interferometer

The powder was sintered under vacuum (0.06 Torr) by SPS in a Thermal Technology LLC 10-3 press using a cylindrical graphite die of 20 mm inside diameter lined with graphite foil and two graphite punches of the same size. The SPS process equipment was automated using a Proportional-Integral-Derivative (PID) controller to follow user defined temperature cycles, pressure ramps and holding time. The process temperature was measured by a S type thermocouple situated in the bored lower punch, just below the powder charge and the ram displacement was measured with a linear variable differential transformer (LVDT). Finally, the density of the samples was determined by the Archimedes method and a theoretical density of 8.22 g/cm^3 was used as the true density of Inconel 718.

Preliminary work revealed the susceptibility of diffusion/reaction bonding between Inconel 718 and the graphite die components at sintering temperatures above 1200°C limiting the range of temperature that could be tested.

To study the effect of the sintering temperature on the density, a first set of experiments was done at different temperatures between 900°C and 1200°C using a heating rate of 200°C/min and a holding time of 1 min. at target temperature. A pressure of 50 MPa and 25 MPa was applied during the heating cycle as presented in Table 8.2.

A study of the heating rate impact on density was conducted at a sintering temperature of 1200°C with heating rates of 20°C/min, 200°C/min, 400°C/min and 800°C/min. A pressure of 50 MPa was used for all the tests and was applied during the initial heating to 600°C in order to sinter the powder under constant pressure conditions. The holding time of the samples sintered at 200, 400 and 800°C/min were adjusted to keep the same energy of sintering (same integrated temperature curve); leaving the 20°C/min condition out of this analysis because of the impractical long holding time that would be required at high heating rates.

Table 8-2 : Sintering parameters used for the compaction of Inconel 718 samples

	Temperature (°C)	**Pressure (Mpa)**	**Heating rate (°C/min)**	**Holding time (min)**
Temperature experiment	900, 1000, 1025, 1050, 1075, 1100, 1125, 1150, 1175, 1200	50 (applied at sintering temperature)	200	1
	1000, 1100, 1200	25 (applied at sintering temperature)		
Heating rate experiment	1200	50 (applied at 600°C)	20	1
			200	1
			400	2,5
			800	3,5

The heating rate effect on the shrinkage was evaluated by the comparison of the density curves obtained from the ram displacement data. Equation 8.1 expresses the relationship between the density of the sintered powder, and the ram position:

$$\rho = \rho_f h / \left(h + (\Delta L)\right) \qquad \text{eq. 8.1}$$

where ρ is the density, ρ_f is the final density, h is the height of the sintered compact and $\Delta L = L(t) - L_f$ is the displacement difference between the ram position at time t and the final position of the ram once the sintering cycle is finished. For this calculation to be valid the contribution of the powder and graphite punches thermal expansion needs to be subtracted from the displacement curve obtained from the SPS. From this equation a density curve could be obtained for each sintering run.

The sintered samples were cut and the section cold mounted in epoxy resin for further grinding and polishing. Polished sections were electrochemically etched using a solution of 10 ml HNO3, 5 ml glacial acetic acid and 85 ml H2O under 1.5V for 5-20 seconds. Alternatively, selected samples section were cut by a low speed diamond waffering blade and left unmounted. The fine surface finish after the cut allowed direct electropolishing in 2:8 perchloric acid:methanol at -40°C and 25V for 25s, followed by electroetching in the same solution at 5V for 3s.

High density samples sintered at 1175°C and 1200°C for 1 min were analyzed for carbon content using a LECO CS230 carbon sulfur analyzer. The average of two analyses is reported.

8.5. RESULTS AND DISCUSSION

8.5.1. Effect of sintering temperature on density

Analysis of the measured density for the samples sintered between 900°C and 1200°C, shown in Figure 8.2, revealed two densification events where sharp increase of more than 5% occurred. A first density plateau (77% - 81%) was identified when the sintering temperatures were between 900°C and 1075°C. Followed by a first densification event occurring at 1100°C, where the density was found to increase to 89%. Further heating to 1150°C did not incur more densification, yielding a density of 90%, thus the temperature region between 1100°C and 1150°C defines a second density plateau. Once more, at 1175°C, the density was observed to increase by 6% going from 90% at 1150°C to 96% and 97% at 1175°C and 1200°C. The densification behavior of Inconel 718 could be divided into three temperature range: low (<1100°C), intermediate (1100°C – 1150°C) and high (>1150°C) temperatures.

Further sintering tests were performed at 25 MPa to evaluate the effect of pressure on the final density obtained at 1000°C, 1100°C and 1200°C. The final relative density was 0.70, 0.84 and 0.88 respectively. The density change caused by the pressure increase from 25 MPa to 50 MPa can be explained by particle rearrangement, which is affected by the interparticle sliding resistance as well as the applied pressure.

The pressure increase has a direct effect on densification by improving the stress at particle contact. Additional stress is generating more deformation (plastic yield) and was shown to increase the final density. The density change when increasing the sintering temperature from 1000°C to 1100°C was 14% TD under 25 MPa and 11% TD under 50 MPa. This behavior suggests a melting event occurred at 1100°C that could assist particle rearrangement by grain boundary lubrication. Observation of the sintered Inconel 718 microstructure could provide insight into the sintering mechanism responsible for the three densification regions identified on Figure 8.2.

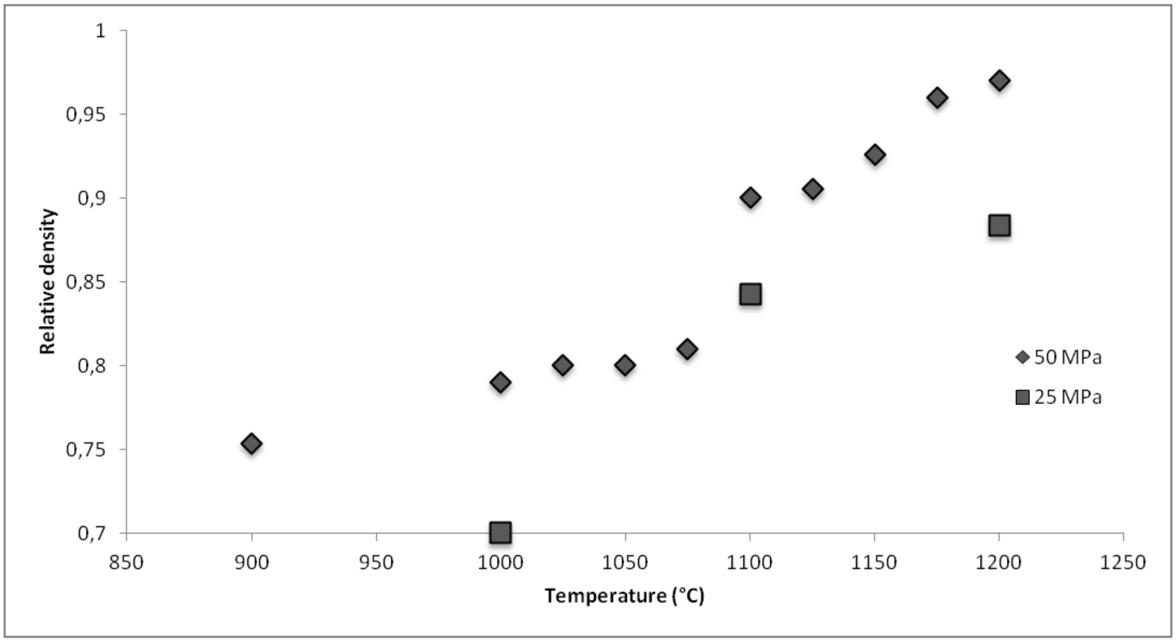

Figure 8-2 : Inconel 718 final density after SPS at different temperatures and applied pressures

The micrographs presented in Figure 8.3(a-c) were taken from the samples sintered at 1000°C, 1125°C and 1175°C; representing each densification regions described in Figure 8.2. The microstructure of Inconel 718 sintered at 1000°C (Figure 8.3a) presented a fine dendritic structure that is typical of the starting powder. The limited sintering temperature and holding time did not allow homogenization of the powder particles. The micrograph shown in Figure 8.3b was taken on the sample sintered at 1125°C. The structure was partially homogenized as can be seen by the formation of equiaxed grains, while some dendrites are still discernible. The pore structure was showing a few signs of liquid phase formation as pointed by the black arrows. Finally, the 1175°C sintering micrograph, presented in Figure 8.3c, was found to be completely homogenized as can be seen from the fully equiaxed grain structure. Second phase particles are distributed within the structure, both at grain boundaries and within grains. The pore structure was again presenting typical features of liquid phase formation and prior particle boundaries were partially populated with second phase particles. Figure 8.3d represents a powder particle observed in the 1150°C interrupted sintering test section. The particle shows signs of melting and second phase particles are distributed on its surface. The second phases can be associated to interdendritic regions, however the second phases bordering the melted zone show a distinct rounded geometry and are thought to be of a different nature.

The liquid phase is known to assist sintering by particle rearrangement, in the initial sintering stage, then by viscous flow and grain boundary sliding creep processes in the final sintering stage [8.24-8.25]. The next section will analyse the liquid phase formation in Inconel 718 in relation to the sintering temperature.

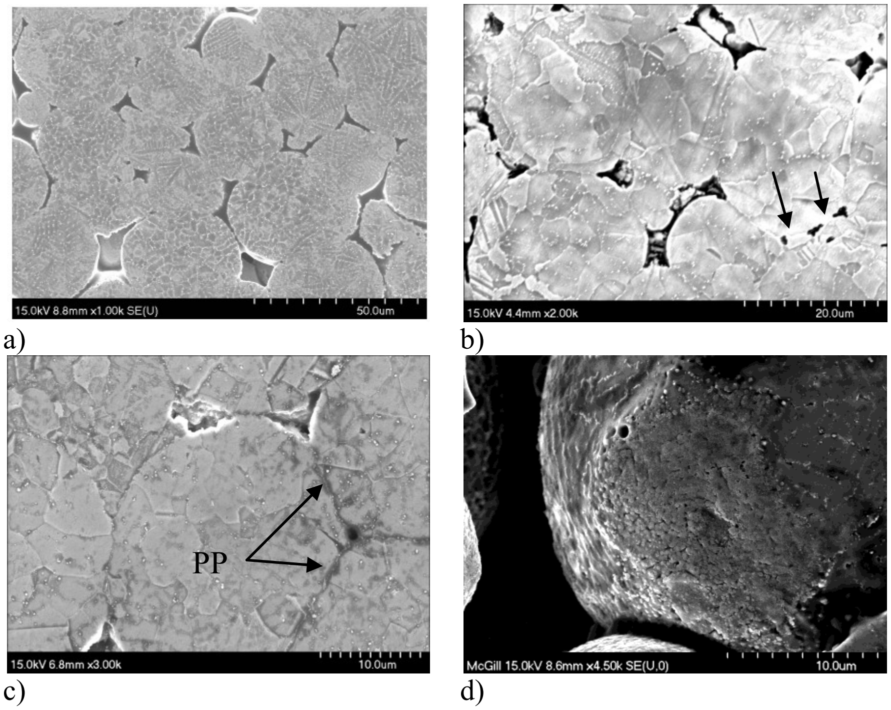

a) b) c) d)

Figure 8-3 : Inconel 718 SPS microstructure after sintering at a temperature of a)1000°C, b) 1125°C, c) 1175°C and d) Particle surface observed in 1150°C interrupted sintering sample

8.5.2. Liquation of Inconel 718

The first melting event identified in the literature, during heating of Inconel 718, is the γ+Laves eutectic reaction (1075°C – 1160°C) [8.26]. In a previous study, differential scanning calorimetry (DSC) of the same Inconel 718 powder, using a heating rate of 10°C/min, showed this reaction to occur at 1098°C – 1128°C [8.27]. Figure 8.4 depicts the liquid fraction reported from the DSC data, which revealed a liquid fraction of 0.2% at 1128°C compared to a liquid fraction of 1.7% at 1200°C.

The predicted value given by Thermocalc software also supplements Figure 8.4 to illustrate the effect of carbon contamination on the liquid fraction formation in Inconel 718. The carbon contamination retards liquid formation from 1165°C at 0.05%C to 1224°C at 0.24%C. Since graphite tooling was used in SPS, carbon contamination is a concern. Contamination could occur by solid state diffusion or CO formation due to graphite reaction with adsorbed water vapor or oxygen [8.28]. However, carbon analysis performed on samples prepared from the 1175°C (0.051%C) and 1200°C (0.053%C) compacts revealed no significant carbon contamination during the sintering time used in this study. Consequently, the liquid fraction predicted at 0.05% carbon concentration should be valid as well as the results obtained by DSC on the same powder.

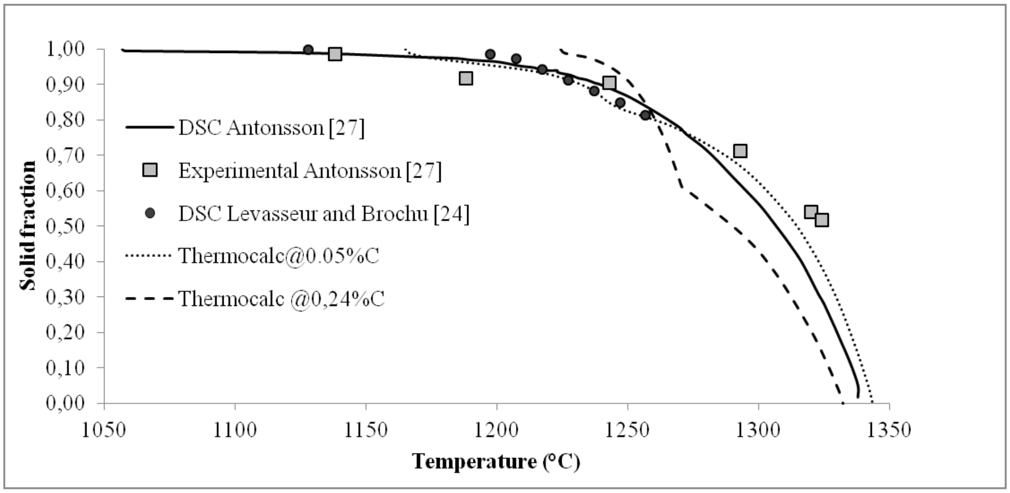

Figure 8-4 : Liquid fraction of Inconel 718 determined by DSC and by Thermocalc™

The discrepancy between the DSC data and Thermocalc™ software can be attributed to the non-equilibrium solidification structure of the powder. As the powder particles were gas atomized, their structure were expected to present features of rapidly solidified metals such as fine dendritic structure. Since the dendritic structure is characterized by microsegregation, which results from solute rejection in the interdendritic regions and constitutional undercooling [9.29], the initial powder structure presented a composition difference between the dendrites core and the interdendritic regions. This segregation was captured by EDS (Figure 8.5) of the residual dendritic structure in the sample sintered at 1125°C.

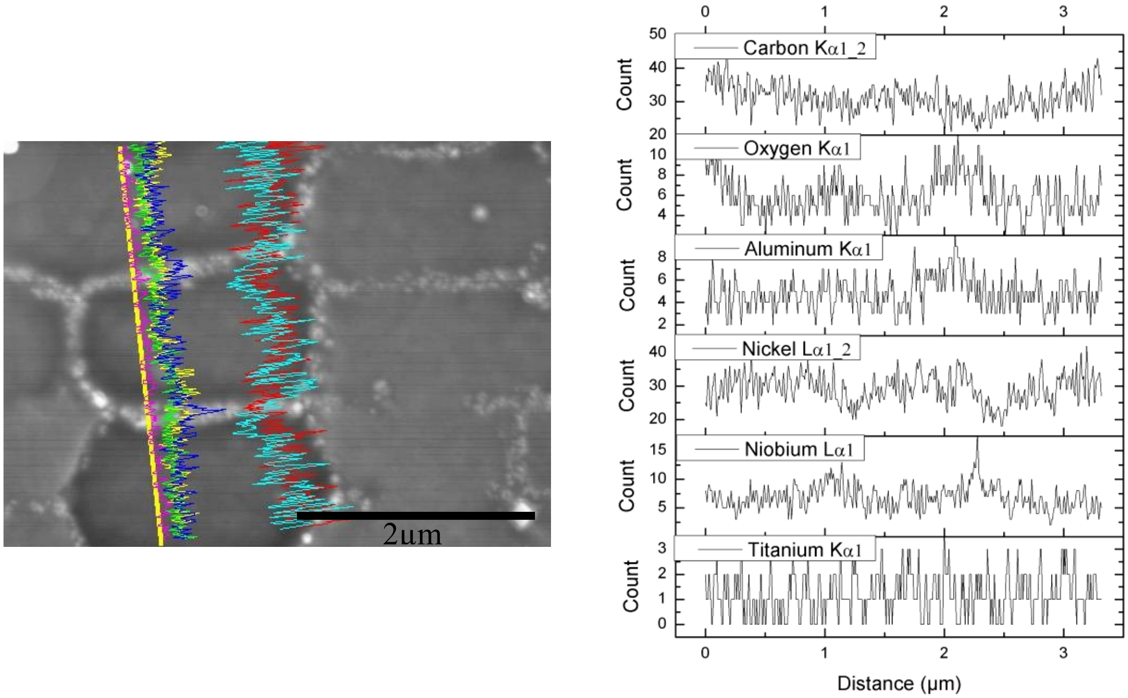

Figure 8-5 : EDS analysis of the remaining dendritic structure after sintering in SPS at 1125°C for 1 min.

Upon reheating, the solute rich interdendritic regions will melt first, and more so when homogenization is limited such as is the case when using high heating rates (200°C/min). Retained dendritic structure was observed in sintered compact at temperatures up to 1150°C, therefore at 200°C/min heating rate, the non-equilibrium liquid formation and homogenization is not completed until the sintering temperature increases to 1175°C and 1200°C.

In that context, the liquid phase increases the sintering rate and a step in density is observed at 1100°C. Since the density does not evolve rapidly between 1100°C and 1175°C it can be deduced that the liquid fraction remains relatively stable in this temperature range, as was measured by DSC. The second density change observed at 1175°C and 1200°C correspond to the Thermocalc™ prediction of liquid formation. The thermodynamic simulation predicts a solidus temperature for Inconel 718 at 0.05%C of 1165°C, and a steady increase in liquid fraction formation up to 4.8% at 1200°C.

Both the density obtained at 50 MPa and 25 MPa pressure indicated a significant increase at 1100°C which supports the rearrangement assisted by liquid phase mechanism. Similarly, the density obtained at 1200°C with the same holding time can be linked with the increase in liquid volume fraction at that temperature. The densification rate in pressure assisted supersolidus liquid phase sintering can be related to the applied pressure through equations 8.2 [8.30] and 8.3 [8.31]:

$$\left(\frac{P_E}{P_A}\right)=\frac{1-\rho_0}{\rho^2\left(\rho-\rho_0\right)}, \qquad \text{eq. 8.2}$$

$$\frac{d\rho}{dt}=\frac{3P_E\left(1-\rho\right)}{4\eta\left(1-\rho_0\right)}, \qquad \text{eq. 8.3}$$

where P_A is the applied pressure, P_E is the effective pressure and η is the system viscosity. Equation 8.2 shows the relationship between the applied pressure and the effective pressure as the density increase. In turn equation 8.3 presents the effect of effective pressure, viscosity and density on the densification rate. For the same densification rate, green density and system viscosity, a reduction of P_E involves a proportional increase in porosity ($1-\rho$), which is in line with the results presented in Figure 8.2 (i.e. density difference 5%–10% between 25 and 50 MPa).

Rao *et al.* sintered Inconel 718 in HIP at 1200°C, but did use 3-h holding time [8.10]. As was shown in this study, heating Inconel 718 powders above 1165°C warrants the formation of a liquid phase, which assist sintering. The pressure application in HIP is hydrostatic; therefore, the liquid phase is most beneficial as a rapid diffusion path, but shear stresses are not experienced [8.31]. Since shear stresses are responsible for liquid assisted grain rearrangement, densification in HIP follows a different kinetic than in SPS or HP.

Consequently, the sintering temperature is lower than for pressureless sintering of Inconel 718 which is commonly sintered between 1250°C and 1300°C [8.4, 8.7-8.8]. The advantage of using lower sintering temperatures is to reduce the liquid fraction formed over 1098°C which is responsible for the formation of brittle laves phase [8.8, 8.27] and PPB carbides.

8.5.3. Prior particle boundaries

The local chemical composition of a PPB in Inconel 718 sintered at 1075°C is shown in Figure 8.6. The PPB (position 3μm) shows a slight segregation of Al, Ti and Nb, which is less apparent than for the carbide particle that was captured at position 5.5μm. The EDS analysis evidenced the cleanliness of the PPB at temperatures of 1075°C. In fact, PPB carbides were found to appear in Inconel 718 sintered at 1100°C, which is the temperature of the early γ/Laves eutectic liquid phase formation.

The PPBs of Inconel 718 sintered at temperatures higher than 1100°C were dotted with second phase particles as shown in Figure 8.3(b,c). Figure 8.7a presents the structure of Inconel 718 sintered at 1200°C. The PPB chemical composition was analysed by EDS on two locations (Figure 8.7b,c). The first location was crossing a second phase particle and the second was taken on a particle free PPB. The composition of the PPB particle was rich in Al, Ti and Nb, which are prone to segregate during liquid solidification. The concentration of C, O and N were also found to be higher at the PPB particle.

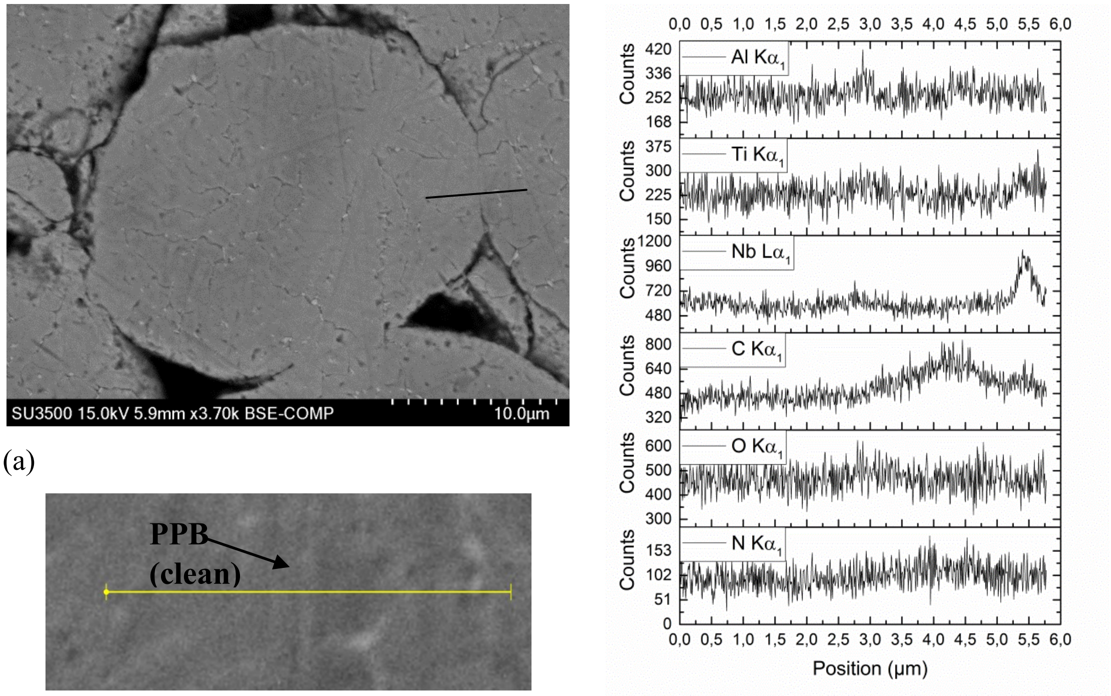

(a)

(b)

(c)

Figure 8-6 : EDS linescan taken on the PPB of Inconel 718 sintered at 1075°C in SPS for 1 min. (a) The linescan locations is given by the black line on the micrograph, (b) enlargement of the linescan area (same scale as *Position* axis in (c)) and (c) elemental profile across the PPB at position 3µm and capturing a grain boundary carbide at position 5.5µm

Using electrolytic dissolution, the matrix of the sample sintered at 1200°C for 1 min was etched and the remaining second phase particles could be separated and analyzed by XRD and EDS (Figure 8.8). The fine blocky particles were found to be Nb and Ti rich and could be identified as MC carbides.

This finding is in line with the chemical analysis of PPB found in HIPed Inconel 718 [8.10, 8.32-8.33], where the particle were identified as MC carbides (M=Nb,Ti) and oxides of aluminum and titanium. Menzies *et al.* observed several instances of carbides growing from an oxide particle and suggested that PPB carbides nucleates more easily on particles surface oxides. The results presented here agree with their observation since the chemical composition of the PPB particles corresponds to what is expected from MC carbides and oxides.

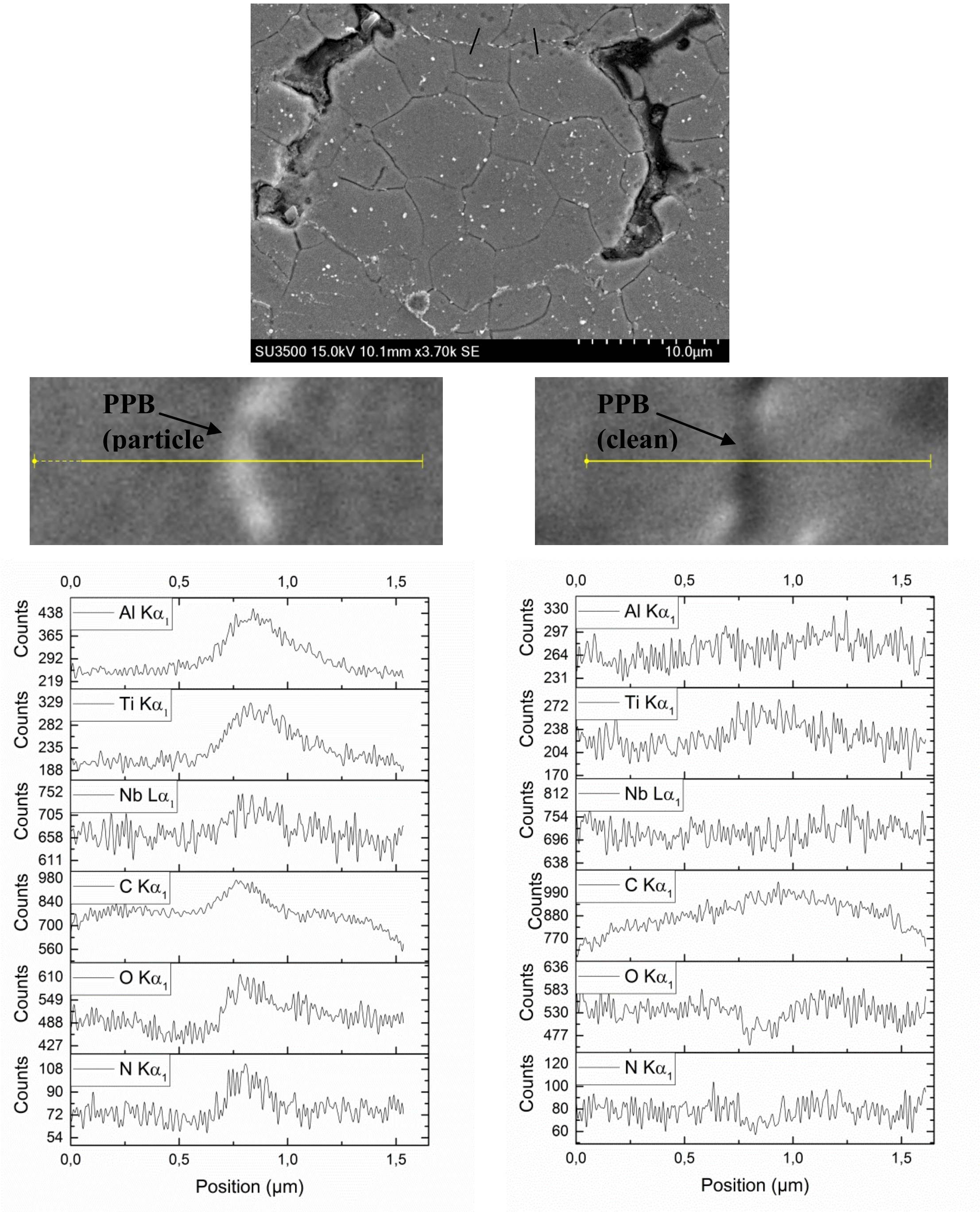

Figure 8-7 : Two EDS linescans taken on the PPB of Inconel 718 sintered at 1200°C in SPS for 1 min. The linescans locations are given by the black line on the micrograph, b) chemical profile across a PPB particle at position 0.8µm, c) chemical profile across a particle free PPB region at position 0.8µm

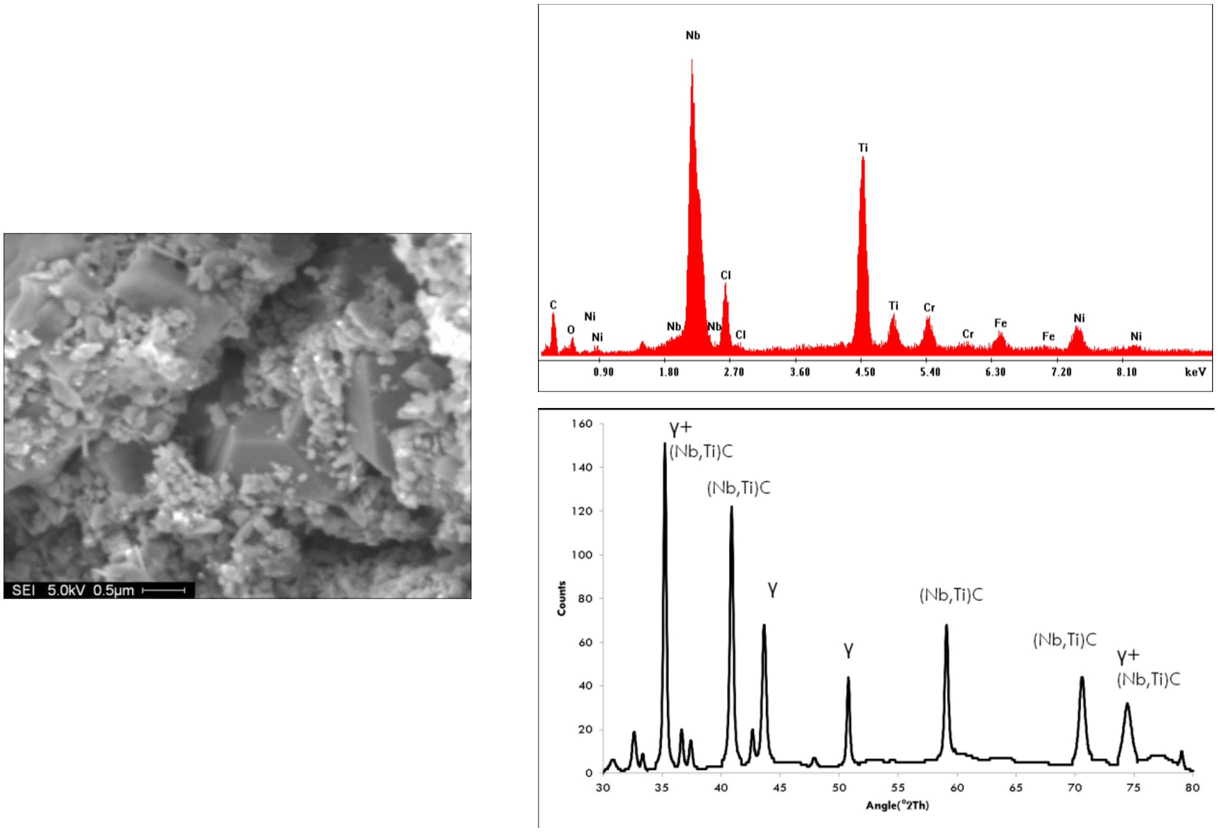

Figure 8-8 : a) Electrolytic dissolution residue of Inconel 718, b) EDS analysis of the blocky particle observed in a) and c) XRD spectrum of the dissolution residue showing MC carbides and Inconel 718 γ matrix

Figure 8.9 presents the neck region obtained in the interrupted test at 1150°C, where a PPB is shown to form. The PPB is not completely wetted by the liquid as is evidenced by the presence of a void in the neck. Moreover, discrete and fine carbides are shown to have formed at the powder particles boundary, while the remaining boundary is the solidified liquid phase.

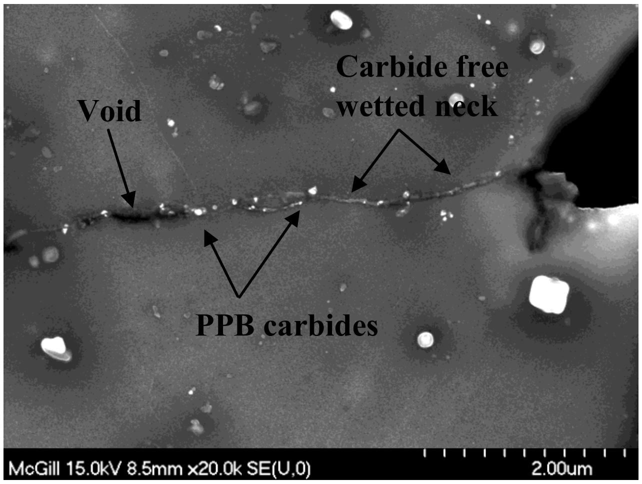

Figure 8-9 : Neck region between two Inconel 718 particles from the 1150°C interrupted sintering test

The PPB carbides observed in SPS of Inconel 718 are similar to those observed in HIP [8.10, 8.32-8.33], as they are niobium and titanium rich, and appear to have nucleated on aluminum and titanium oxides. The appearance of PPB carbides and the first density change are occurring at 1100°C. Both events can be associated with the formation of a liquid phase, since PPB carbides involves niobium and titanium reactions, which are segregated in the interdendritic regions of Inconel 718 powder particles, and density change can be associated to a mass flow mechanism transition from solid state pressure assisted sintering to supersolidus liquid phase pressure assisted sintering. The possible mass transport mechanism for the migration of titanium and niobium from the interdendritic regions to the PPB are grain boundary diffusion, volume diffusion or diffusion through a liquid phase. The clean PPB shown in Figure 6 do not present significant segregation of Nb and Ti at the neck, which demonstrate that these elements have to migrate to the neck region in order to form a continuous carbide film. Consequently it is tought that Inconel 718 liquation occurring at 1100°C permits the mass transport of Nb and Ti through liquid phase migration to the neck. The availability of nucleation sites for MC carbides in the presence of oxides of aluminum and titanium at the PPB would favour the formation of carbides. Rao *et al.* have shown low oxygen content Inconel 718 powder to be devoid of PPB carbides after HIPing at 1200°C. Therefore, in the absence of nucleation sites, Nb and Ti would remain in solution at the grain boundary, or diffuse in the matrix since a chemical gradient favours migration from the liquid phase to the matrix [8.34].

8.5.4. Effect of heating rate

The density of Inconel 718 sintered at 1200°C using increasing heating rates from 20°C/min to 800°C/min is presented in Table 8.3. The final density was found to increase from 95% to 97%, 100% and 100% for the 20°C/min, 200°C/min, 400°C/min and 800°C/min respectively; while the sintering cycle time decreased from 60 min to 5 min.

Table 8-3 : Inconel 718 sintering parameters as a function of the heating rate in SPS

Heating rate (°C/min)	Final density (% TD)	Peak densification rate (μm/μm)	Peak densification rate temperature (°C)	Grain size (μm)
20°C/min	95	0.06	1015	5.0 ± 0.25
200°C/min	97	0.34	1171	5.1 ± 0.20
400°C/min	100	0.44	1200	5.2 ± 0.22
800°C/min	100	0.60	1200	6.5 ± 0.28

The effect of SPS heating rate on the final density of $MoSi_2$ reported by Stanciu *et al.* [8.23] showed a stable final density between 50°C/min and 250°C/min followed by an increased final density at 700°C/min. Similarly, Hu *et al.* [8.21] showed a temperature dependency of the heating rate effect on density with Ni-Fe-W powder. They showed there was a critical sintering temperature under which an increase of the heating rate resulted in a lower density; whereas increasing heating rates for sintering temperatures higher than this critical value either caused an increase or retention of the final density. Based on their observations the sintering temperature chosen in this study for the heating rate experiments was clearly larger than the critical temperature since the final density increased with heating rate.

As the principal densification mechanism in the test conditions was particle rearrangement assisted by liquid phase, it could be hypothesized that the final density is linked to the liquid fraction formed in Inconel 718 at 1200°C using different heating rates.

The densification rate of Inconel 718 shown in Figure 8.5b are listed in Table 8.3 along with the final density, the peak densification temperature and the average grain size (± 95% confidence interval). The increasing heating rate was found to delay the liquid formation to higher temperatures as can be seen by the peak densification temperature shift towards higher temperature. Liquid formation is delayed to higher temperature as a result of the melting rate compared to the heating rate, especially since the temperature sensor is not attached directly to the sample.

The final density increase with heating rate can be related to the higher amount of time spend at the sintering temperature (1200°C). Effectively the experiments were designed to obtain an equivalent thermal work (temperature-time integral) between each heating rate except the lowest one (20°C/min). This results in prolonged holding time at the sintering temperature for the higher heating rates. Since Inconel 718 is mainly sintered by liquid phase assistance, the sintering is more active during the 1200°C hold than while heating. Therefore, the high heating rates achieved by SPS of Inconel 718 at 1200°C yielded improved final density for the same thermal work.

ACKNOWLEDGEMENTS

The authors are grateful to Dr Bernard Tougas for providing the Thermocalc data for Inconel 718 and Mr Yuan Tian for performing the EDS linescan. The financial support from the McGill Engineering Doctoral Award provided to D. Levasseur is also acknowledged.

8.6. REFERENCES

8.1. Betteridge, W. and S.W.K. Shaw, *Development of Superalloys.* Materials Science and Technology, 1987. **3**(9): p. 682-694.

8.2. Dudzinski, D., et al., *A review of developments towards dry and high speed machining of Inconel 718 alloy.* International Journal of Machine Tools and Manufacture, 2004. **44**(4): p. 439-456.

8.3. Gessinger, G.H., *Powder metallurgy of superalloys*. Butterworths monographs in materials. 1984, London ; Boston: Butterworths. 348 p.

8.4. Valencia, J.J., J. Spirko, and R. Schmees, *Sintering effect on the microstructure and mechanical properties of alloy 718 processed by powder injection molding.* Superalloys 718, 625, 706 and Various Derivatives, 1996: p. 753-762.

8.5. Bose, A., et al., *Powder injection molding of Inconel 718 alloy.* Advances in Powder Metallurgy & Particulate Materials - 1997, 1997: p. 1899-18112.

8.6. Schmees, R., J.R. Spirko, and J. Valencia. *Powder injection molding (PIM) of Inconel 718 aerospace components*. in *Proceedings of the Advanced Particulate Materials & Processes*. 1997.

8.7. Wohlfromm, H., et al., *Metal Injection Moulding of Nickel-based Superalloys for High Temperature Applications.* Proceedings Euro PM2003 Congr. Exhib., 2003. **3**: p. 207-215.

8.8. Özgün, O., et al., *Microstructural and mechanical characterization of injection molded 718 superalloy powders.* Journal of Alloys and Compounds, 2013. **576**: p. 140-153.

8.9. Reichman, S., *Low cost P/M superalloy applications in turbines.* International Journal of Powder Metallurgy and Powder Technology, 1975. **11**: p. 277-283.

8.10. Rao, G.A., et al., *Characterisation of hot isostatically pressed nickel base superalloy Inconel*718.* Materials Science and Technology, 2003. **19**(3): p. 313-321.

8.11. Rao, G.A., M. Srinivas, and D.S. Sarma, *Effect of oxygen content of powder on microstructure and mechanical properties of hot isostatically pressed superalloy Inconel 718.* Materials Science and Engineering a-Structural Materials Properties Microstructure and Processing, 2006. **435**: p. 84-99.

8.12. Yamanoglu, R., et al., *Characterisation of nickel alloy powders processed by spark plasma sintering.* Powder Metallurgy, 2014. **57**(5): p. 380-386.

8.13. Kodash, V., et al., *Field-assisted sintering of Ni nanopowders.* Materials Science and Engineering: A, 2004. **385**(1): p. 367-371.

8.14. Minier, L., et al., *Influence of the current flow on the SPS sintering of a Ni powder.* Journal of Alloys and Compounds, 2010. **508**(2): p. 412-418.

8.15. Zhang, Z., et al., *Mechanical Behavior of Cryomilled Ni Superalloy by Spark Plasma Sintering.* Metallurgical and Materials Transactions a-Physical Metallurgy and Materials Science, 2009. **40A**(9): p. 2023-2029.

8.16. Minier, L., et al., *A comparative study of nickel and alumina sintering using spark plasma sintering (SPS).* Materials Chemistry and Physics, 2012. **134**(1): p. 243-253.

8.17. Vanmeensel, K., et al., *Modelling of the temperature distribution during field assisted sintering.* Acta Materialia, 2005. **53**(16): p. 4379-4388.

8.18. Tiwari, D., B. Basu, and K. Biswas, *Simulation of thermal and electric field evolution during spark plasma sintering.* Ceramics International, 2009. **35**(2): p. 699-708.

8.19. Räthel, J., M. Herrmann, and W. Beckert, *Temperature distribution for electrically conductive and non-conductive materials during field assisted sintering (FAST).* Journal of the European Ceramic Society, 2009. **29**(8): p. 1419-1425.

8.20. Molénat, G., et al., *Temperature control in Spark Plasma sintering: an FEM approach.* Journal of Metallurgy, 2010. p.9-9.

8.21. Hu, K., et al., *Effect of Heating Rate on Densification and Grain Growth During Spark Plasma Sintering of 93W-5.6 Ni-1.4 Fe Heavy Alloys.* Metallurgical and Materials Transactions A: Physical Metallurgy and Materials Science, 2013. **44**(9): p. 4323-4336.

8.22. Olevsky, E.A., S. Kandukuri, and L. Froyen, *Consolidation enhancement in spark-plasma sintering: Impact of high heating rates.* Journal of Applied Physics, 2007. **102**(11).

8.23. Stanciu, L.A., V.Y. Kodash, and J.R. Groza, *Effects of heating rate on densification and grain growth during field-assisted sintering of alpha-Al2O3 and MoSi2 powders.* Metallurgical and Materials Transactions a-Physical Metallurgy and Materials Science, 2001. **32**(10): p. 2633-2638.

8.24. German, R.M., *Supersolidus liquid-phase sintering of prealloyed powders.* Metallurgical and Materials Transactions A: Physical Metallurgy and Materials Science, 1997. **28**(7): p. 1553-1567.

8.25. Kingery, W., J. Woulbroun, and F. Charvat, *Effects of applied pressure on densification during sintering in the presence of a liquid phase.* Journal of the American Ceramic Society, 1963. **46**(8): p. 391-395.

8.26. Antonsson, T. and H. Fredriksson, *The effect of cooling rate on the solidification of INCONEL 718.* Metallurgical and Materials Transactions B-Process Metallurgy and Materials Processing Science, 2005. **36**(1): p. 85-96.

8.27. Levasseur, D. and M. Brochu, (2015), *Supersolidus Liquid Phase Sintering Modelling of Inconel 718 Superalloy.* Manuscript submitted for publication

8.28. Guillon, O., et al., *Field-Assisted Sintering Technology/Spark Plasma Sintering: Mechanisms, Materials, and Technology Developments.* Advanced Engineering Materials, 2014. **16**(7): p. 830-849.

8.29. Glicksman, M.E., *Principles of solidification: an introduction to modern casting and crystal growth concepts*. 2010: Springer Science & Business Media.

8.30. Helle, A.S., K.E. Easterling, and M.F. Ashby, *Hot-isostatic pressing diagrams: New developments.* Acta Metallurgica, 1985. **33**(12): p. 2163-2174.

8.31. German, R.M., *Chapter Ten - Sintering With External Pressure*, in *Sintering: from Empirical Observations to Scientific Principles*, R.M. German, Editor. 2014, Butterworth-Heinemann: Boston. p. 305-354.

8.32. Menzies, R.G., R.H. Bricknell, and A.J. Craven, *Stem Microanalysis Of Precipitates And Their Nuclei In A Nickel-Base Super-Alloy.* Philosophical Magazine A, 1980. **41**(4): p. 493-508.

8.33. Marquez, C., G. Lesperance, and A.K. Koul, *PRIOR PARTICLE BOUNDARY PRECIPITATION IN NI-BASE SUPERALLOYS.* International Journal of Powder Metallurgy, 1989. **25**(4): p. 301-308.

8.34. Zuo, H., *Mechanism of constitutional liquid film migration*. 1996, The University of Alabama at Birmingham: Ann Arbor. p. 123-123

CHAPTER 9. GENERAL DISCUSSION

The objective of this study is to evaluate different sintering approaches to produce high-density near-net-shape Inconel 718 P/M parts. Inconel 718 P/M parts are commonly HIPed to obtain full density and improve the mechanical properties [9.1-9.5]. To eliminate the necessity of HIPing mandatorily requires the development of alternative sintering processes yielding similar final densification. However, the challenges related to the sintering of Inconel 718 powders to full density go beyond parameters optimization, but also require consideration of artifacts that influence the service performance, such as a defect free and small grain size sintered microstructure.

As evidenced by Hajmrle and Anger [9.6], densification of Inconel 718 begins at 1187 °C when sintered in a dilatometer, which could be linked to the formation of a liquid phase that could not be identified at the time. Thus, similar to many other superalloys, Inconel 718 is sintered in the supersolidus liquid phase regime. The liquid formation (including volume fraction and distribution) during sintering is a key process parameter, but is only indirectly controlled by the sintering temperature and is affected by initial powder segregation and contamination. Moreover, the liquid phase formation and distribution in the powder compact is a dynamic process which can be influenced by the sintering heating rate [9.7]. The liquid phase is responsible for particle rearrangement and pore filling in pressureless sintering, while it increases the densification rate during pressure assisted sintering by viscous flow processes [9.7-9.11]. Since the general objective of this study is to produce full density P/M Inconel 718, the effect of sintering process parameters such as the sintering temperature, heating rate, green density and applied external pressure on the sintered density, liquid phase formation and microstructure (grain size, carbides, Laves phase) will be discussed.

9.1. SINTERING OF INCONEL 718 IN THE SLPS REGIME

Coarse gas atomized prealloyed Inconel 718 powders (>10 μm) are the most common feedstock for P/M production, since finer particle sizes were shown to be severely contaminated with surface oxides [9.12-9.13] which are detrimental to the part sinterability and final properties. These powders are typically spherical with an inherent high strength, which impedes the ability to compact the powder to high green densities and sufficient green strength [9.13]. In that context, green compacts are typically produced by mixing powder with an organic binder, developing interparticle linkages and providing strength to the unconsolidated part. However, the process adds a debinding step that must be conducted prior to sintering, to remove the binder while avoiding contamination by carbon, oxygen and hydrogen.

Using larger particle size powders reduces the contamination, but is also known to inhibit the solid state sintering process. The driving force of solid state sintering is the minimization of the system free energy by the elimination of internal pore surface and its associated solid-vapor interface energy. Since the pore surface to volume ratio is particle size dependant, the sintering driving force also scales proportionally to $1/D$, where D is the particle diameter. Moreover, the alloying elements were found to decrease solid state sinterability by a combination of powder surface oxidation (oxide formers: Al, Ti) and limited ability of grain boundaries to act as vacancy sinks [9.13]. In view of the difficulties involved in sintering coarse superalloy powders, the Inconel 718 sintering process requires the assistance of a supersolidus liquid phase to rapidly achieve high density.

Liquid phase sintering requires prior knowledge of the powders solidification structure and its melting behavior in order to control the liquid fraction formation during the heating and holding cycle of the sintering process. Solidification of Inconel 718 is characterized by segregation of Nb, Ti and Mo, which readily form Laves phase $(Ni,Fe,Cr)_2(Nb,Ti)$ and MC carbides eutectics [9.14-9.15]. This was confirmed by chemical microanalysis of the powder interdendritic regions. Niobium-rich Laves phases were observed surrounding the dendrite arms, which had lower niobium concentration. Thermal analysis of Inconel 718 powders have shown the occurrence of two eutectic reactions: γ/Laves at 1098 °C and γ/NbC at 1247 °C. The lowest temperature for SLPS is defined by the first eutectic reaction starting at 1098 °C. Liquid volume fraction of 0.2% was computed from the DSC trace at 1127 °C and 1.3% at 1197 °C. SLPS model predictions of the coverage of grain boundaries by the liquid phase (F_c, assuming dihedral angle of 30°) yielded 10.8% at 1098 °C and 27.4% at 1197 °C. The values of fractional coverage F_c are obtained by considering that all the liquid was distributed at grain boundaries. Since rapid viscous flow rearrangement in SLPS occurs at F_c values between 0.8 and 0.9 [9.16], the liquid fraction formed by the γ/Laves eutectic reaction is not sufficient to obtain full density in pressureless sintering and the γ/NbC eutectic temperature must be used.

The formation of liquid phase in the powder compact creates a semi-solid part whose rigidity is determined by the presence and strength of a solid skeleton [9.8]. Solid-solid particle contact strength is the only force maintaining the part integrity against the action of gravity [9.17]. Therefore, the amount and distribution of liquid phase in the powder compact is very important in determining the rigidity of the semi-solid part. When the solid skeleton strength is insufficient to resist deformation under gravity, the part shape is lost due to slumping of the semi-solid body. Liu *et al.* have shown that the solid skeleton strength is related to grain size and liquid fraction [9.17]. They developed a softening parameter, which is a function of the solid skeleton rigidity, to predict the onset of densification as well as distortion. Based on pressureless sintering experimental results obtained in this study and from other works, the softening parameter of Inconel 718 was determined. A distortion threshold was defined based on the sintering temperature and grain size; however, the main parameter was found to be sintering temperature. It was found that sintering Inconel 718 without distortion was possible at 1300 °C up to a grain size of 20 μm. Consequently, the upper temperature limit for sintering Inconel 718 was determined thereby defining the pressureless sintering process window.

Is distortion an issue with high green density compacts such as the CGDS deposits? Unfortunately, there is no straightforward answer to this question. Lal [9.18] sintered bronze with starting densities of 59% and 88% in the SLPS regime; their results showed the same distortion trend for low and high green density compacts as a function of sintering temperature, but the high green density compact yielded the highest final density. In the case of Inconel 718 deposits produced by CGDS the green density is 97.5%. The simple fact that less liquid volume fraction is needed to achieve full density is advantageous, as slumping is active only at a critical temperature.

9.2. THE EFFECT OF GREEN DENSITY ON INCONEL 718 SINTERING

Maximum density achieved by the powder-binder production route lies between 60% and 75% TD depending on the powder size distribution. Using a wide powder size distribution allows better packing as was shown by Contreras *et al*. [9.19]. The main effect of green density during SLPS is to reduce the shrinkage of the compact during densification. Hence, improving the green density minimizes the pore fraction that has to be filled by liquid phase assisted viscous flow. As was mentioned, the high hardness and sphericity of the gas atomized prealloyed Inconel 718 powders prevents the use of cold compaction methods to increase the green density.

To circumvent the compressibility limitation, Inconel 718 powders were sprayed using the high velocity cold gas dynamic spray (CGDS) process. The relatively low temperature of the gas stream (800 °C) is advantageous to avoid oxidation of the powder surface and the particles high velocity (750 m/s) is responsible for their deformation and compaction upon hitting the substrate. The CGDS process efficiency was found to be very sensitive to the gas stream temperature. The deposition efficiency increased from 19% at 550 °C to 30% at 800 °C. Considering that the powder cannot be reused, the BTF ratio starts at 3.33 which is just under the 3.6 BTF ratio obtained using the direct near-net-shape HIP process route [9.20]. Nonetheless, the CGDS process could be further optimized and was found to be an interesting option for building protrusions on simple shapes. Therefore, it is important to determine the benefits of higher green density in order to evaluate the potential of this processing route.

Figure 9.1 shows the sintered density comparison between 95% green density CGDS compacts and 60% green density slip cast compacts.

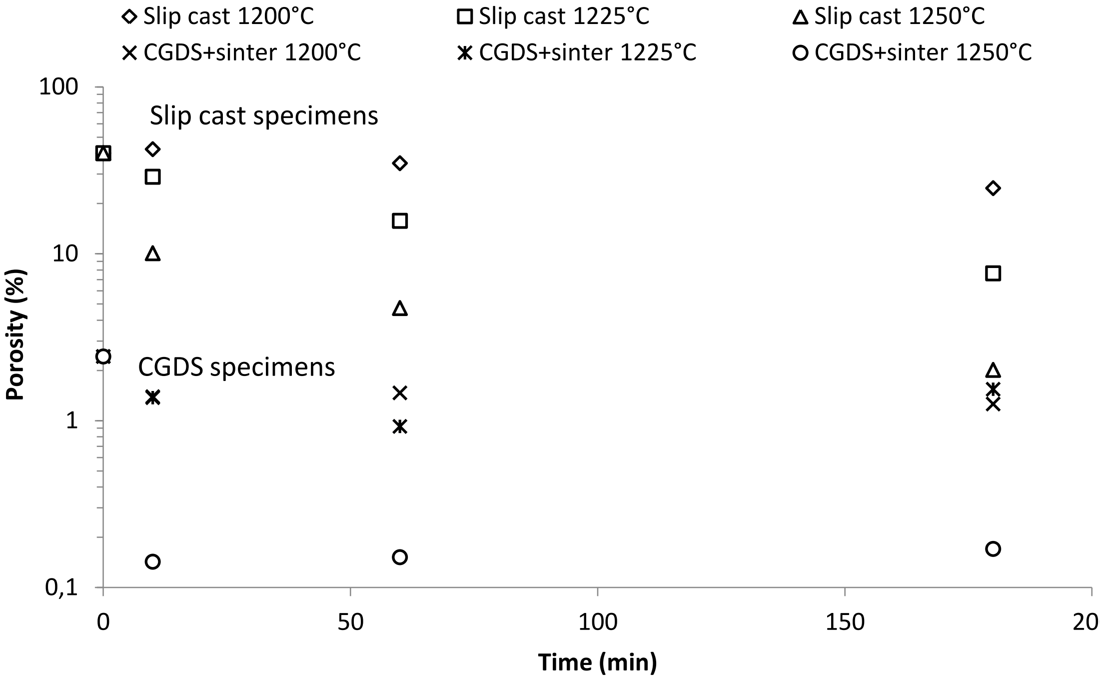

Figure 9-1 : Comparison of the porosity fraction evolution during isothermal holding of slip cast samples and CGDS samples on semi-log scale

As expected in SLPS, the sintering temperature is a key parameter to achieve full densification. The slip cast specimens had a starting porosity of 40% therefore the limited amount of liquid phase formed at 1250 °C was sufficient to cause shrinkage of the compact. Thus the capillary stress is found to be greater for porous structures, as the solid contact area is small within the compact. Consequently, a small capillary force is able to induce shrinkage at lower densities, where the capillary stresses overcome the particle contact strength. On the other hand sintering at 1250 °C provided both the low and high porosity specimens with enough liquid phase formation to reduce porosity up to the closed pore regime (>94% TD). The advantage of the CGDS specimen having a low starting porosity is evident even for the shortest sintering time experimented in this study (10 min), where the porosity reached a final value of 0.15% compared to 10% for the slip cast specimen. This level of porosity is on par with the results published for the near-net-shape MIM+HIP route and is a promising, "binderless" alternative to MIM.

9.3. THE ROLE OF HEATING RATE IN INCONEL 718 SINTERING

The current assisted sintering technique, commonly known as spark plasma sintering (SPS), involves rapid heating to the sintering temperature and is widely applied to consolidate powders produced with metastable structures or nanosized grains. The technique was used with a special pressureless setup (FPSPS) to sinter Inconel 718 at heating rates ranging from 20 °C/min to 200 °C/min. The primary and most obvious effect of the increase in heating rate is to reduce the sintering cycle time from 60 minutes at 20 °C/min to 6 minutes at 200 °C/min. This is an important productivity advantage, but it is not the only positive effect. The Inconel 718 MSC was computed based on the FPSPS data, and it was shown that sintering at heating rates of less than 50 °C/min required more "Thermal Work" to achieve the same density than with heating rates of 75 °C/min up to 200 °C/min. Since the Thermal Work is a function of temperature and time of sintering, it is analogous to a work of sintering in terms of energy required to bring a compact to a given density. Therefore, increasing the heating rate over 75 °C/min decreases the energy required to sinter the compact.

As the key parameter in SLPS is the liquid phase volume fraction, shrinkage due to solid state sintering during the heating ramp is not expected to play a significant role during densification. The final temperature of sintering should have more impact on shrinkage, as it is directly related to the liquid phase formation. However, it was found that liquid phase formation is delayed till higher temperatures as the heating rate is increased. Effectively, upon reaching the eutectic temperature the liquid starts forming while the furnace temperature is still increasing. As the eutectic melting consumes energy (endothermic reaction), the temperature of the sample is expected to stay constant until the reaction is completed. Accordingly, by measuring the furnace temperature, there is a discrepancy between the recorded sintering temperature and the sample temperature during the liquid formation; this discrepancy increases with heating rate. The reduction of the MSC "Thermal Work" for high heating rates is independent of the exact sample temperature as it considers the temperature-time integral of the furnace temperature. Therefore, the sintering heating rates of 75 °C/min and higher improve the shrinkage by enhancing the SLPS mechanism. The situation is similar to that of transient liquid phase sintering, where limiting the microstructure homogenization prior to processing at the melting temperature of the transient liquid phase increases the amount of liquid phase formation and hence the shrinkage. In the case of Inconel 718, a transient liquid phase is formed when the γ/Laves eutectic temperature is reached. The interdendritic regions are composed of this eutectic and should melt first; however, homogenization of the interdendritic region is favoured when heating rates under 75 °C/min are used.

Further benefits of the selected heating rates were observed with samples sintered by SPS. Higher heating rates increased the final density for the same temperature-time integral (Thermal work). It should be pointed out that increasing the heating rates also involved longer holding time at the sintering temperature which could be the most beneficial feature of the experiment. In fact, the time saved during the heating ramp was used to extend the holding time, which is the most active sintering time since liquid is present and the action of pressure in SPS is maximized at this temperature (1200 °C).

9.4. PRESSURE ASSISTED SINTERING OF INCONEL 718

Inconel 718 SLPS under an external pressure has been shown to result in full compaction and is also considered an interesting alternative to near-net-shape HIPing processes. The main advantage of SPS is the rapid heating and low total cycle time. However, the production of complex shapes is limited, as the die complexity involves high development cost. Moreover, the short sintering cycle was shown to limit the average final grain size to 6.5 μm. The small grain size allows engineering of the part properties according to its service environment. Coarse grains are beneficial for high temperature creep resistance, however small grains enhance the room temperature yield strength.

The interest in SPS of Inconel 718 lies in the applied pressure, which assists with compaction of the part to high density. Figure 9.2 presents the effect of pressure on sintering Inconel 718 at 1200 °C for short holding times. The pressureless sintering data shows no densification after 10 minutes holding time, however, an applied pressure of 3 MPa in SPS yielded a considerable decrease in porosity to 27%. Further increase in applied pressure to 25 MPa and 50 MPa further reduced porosity to 12% and 2%, respectively. The applied pressure increases densification for a given liquid fraction by assisting grain rearrangement. In pressureless sintering, porosity levels of 2% were obtained with a process temperature of 1250 °C which yielded 14% liquid fraction. In the SPS process, the liquid fraction required for densification is reduced by a factor of 2.9 to 4.8%. Therefore, the part microstructure remains homogeneous and is characterized by the absence of Laves phases.

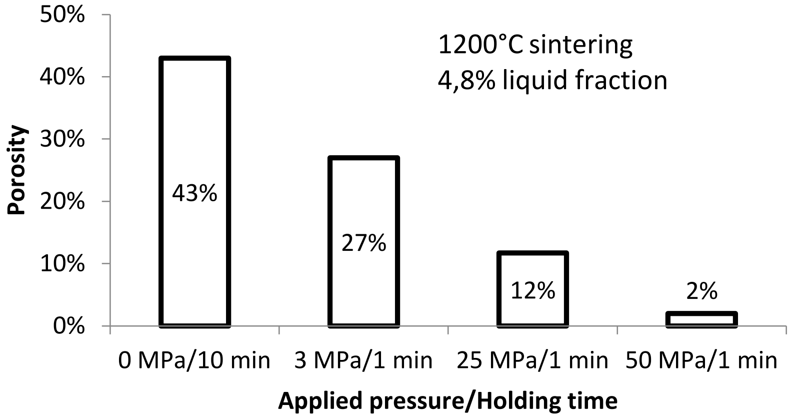

Figure 9-2 : The effect of pressure on the porosity after sintering (the result at 0 MPa was obtained in a resistance furnace, all the other results were obtained in the SPS press)

Laves phase formation in FPSPS was shown to occur upon solidification of the liquid fraction at a critical temperature. This critical temperature was not reached in SPS and the liquid distribution is modified by pressure. Analysis of the second phase found in Inconel 718 after SPS showed the presence of MC carbides and the absence of Laves phase.

9.4.1. Effect of processing parameters on the microstructure evolution

Presented in Figure 9.3 are the microstructure differences between samples of equivalent density sintered by – pressureless sintering at 1250 °C with 180 min hold; FPSPS at 1334 °C, 100 °C/min with no hold; and SPS at 1200 °C, 200 °C/min with 1 min hold. The first apparent difference is the grain size, which is larger in the pressureless sintered samples compared to the SPS sample. The difference in sintering temperature is responsible for the grain coarsening detected in pressureless sintering as was also observed for the cold sprayed samples sintered at 1250 °C. The presence of carbides at the grain boundaries helps restrain grain growth by the Zener pinning effect. Additionally, the high solute content in the grain boundaries increases the solute drag effect. On reaching the temperature of 1250 °C, the γ/NbC eutectic reaction is activated and more liquid is formed at the grain boundaries, which relieves the solute drag and pinning effect and allows free grain coarsening.

The second difference is the liquid fraction in each sample. Chemical etching of the FPSPS sample evidenced approximately 16% liquid fraction, even if the equilibrium value is 73%. The melted regions in the FPSPS sample produced Laves phases on solidification. On the other hand, the liquid fraction obtained in the pressureless and the SPS samples reached 14% and 4.8% (equilibrium values) respectively and did not yield Laves phase or severe segregation.

Finally, all samples presented MC carbides in the grains or at grain boundaries. However, the carbides are more numerous, smaller in diameter and more homogeneously distributed in the SPS sample. This could be due to the combination of low temperature and high heating rate, as will be discussed in the following subsection.

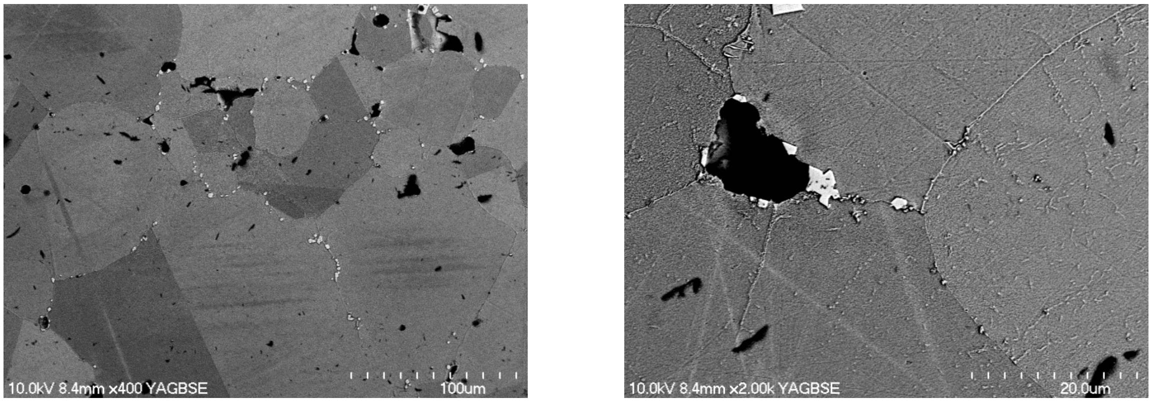

a) Pressureless sintering at 1250 °C for 180 min

b) Pressureless sintering at 1250 °C for 180 min at higher magnification

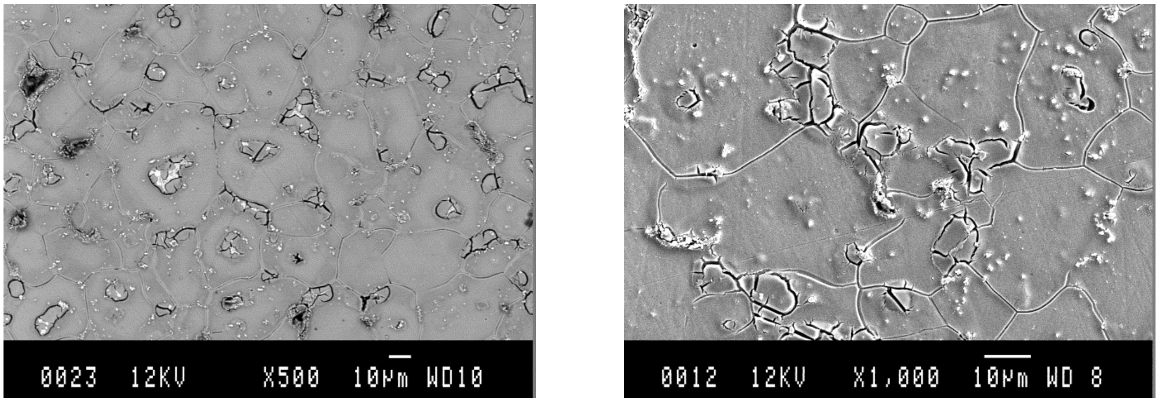

c) FPSPS at 1334 °C, no holding time. Notice the etched areas where liquid was formed.

d) FPSPS at 1334 °C, no holding time. Higher magnification, carbides were formed inside grains.

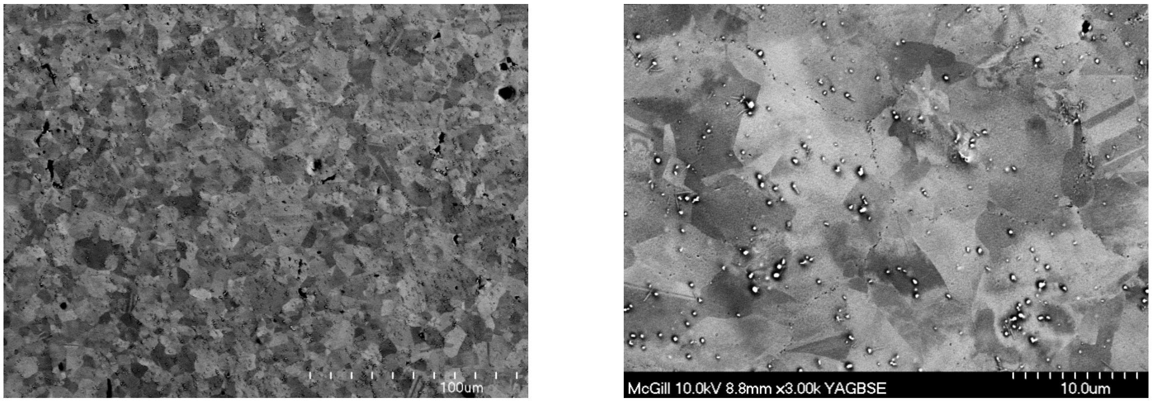

e) SPS at 1200 °C, 1 min holding time

f) SPS at 1200 °C, 1 min holding time. Higher magnification showing the carbides and fine PPB particle chains.

Figure 9-3 : Comparison of the microstructure obtained for similar density samples and different sintering processes

9.4.2. The formation of PPB carbides in pressure assisted sintering

The principal defect responsible for low ductility of pressure assisted sintered Inconel 718 is the formation of small chains of carbides at the PPB. The PPB carbides were observed in all HIP studies except for low oxygen (coarse) powders [9.12]. Post sintering thermomechanical treatment [9.21] or homogenization heat treatments [9.22] have proved successful in disrupting the PPB carbides. However, the drawback of such additional treatments is the processing time and cost increase. In this study, despite using a powder with oxygen content below the published PPB carbides formation threshold (200 ppm), PPB carbides were observed in several sintered samples indicating another source for their formation. The EDS chemical analysis of the powder compact in different stages of sintering was relevant in finding the sequence of formation of PPB carbides. By combining the observation of second phase distribution and chemical composition, it was possible to link the liquid phase formation and spreading to the presence of MC carbides at the PPB.

The first important information was the observation of the homogenization of the dendritic structure when the sintering temperature exceeded 1175 °C. In fact, at heating rates of 200 °C/min, the dendritic structure begins its recrystallization between 1075 °C and 1100 °C and the phenomenon is completed at 1175 °C. It is also in the 1075 °C to 1100 °C temperature range that the first γ/Laves eutectic reaction is expected to occur. Consequently the melting of γ/Laves eutectic is expected to begin in the interdendritic regions and the liquid should be found mainly inside the grains, and at grain boundaries. Figure 9.4(c) presents regions where remnants of the dendritic structure can still be observed, showing how the first liquid is formed inside the particles and must migrate to the neck to be effective in assisting shrinkage. As the liquid present within grains does not provoke a capillary stress between touching particles, the shrinkage is minimal in pressureless sintering. However, a small applied pressure was shown to induce significant shrinkage at 1200 °C, suggesting that the pressure is effectively modifying the liquid distribution and allows densification below the NbC/γ eutectic.

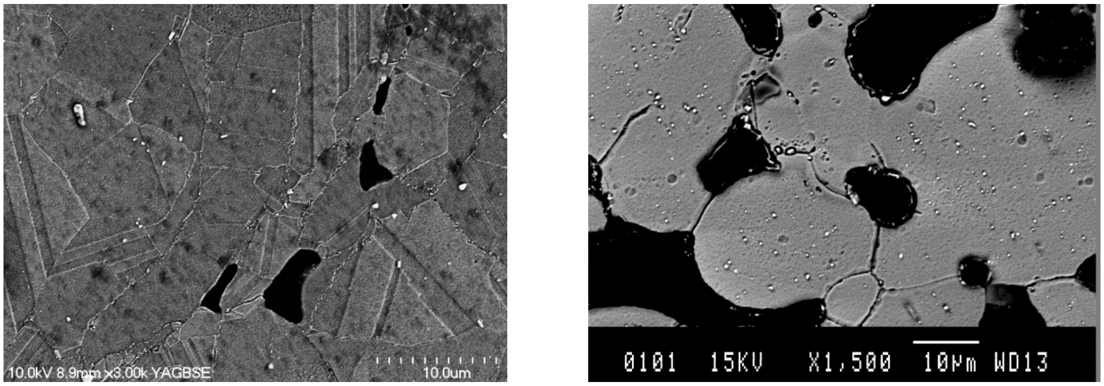

a) CGDS sample sintered at 1200 °C for 10 min; the grains are recrystallized and present MC carbides.

b) FPSPS sample sintered at 15 K/min to 1200 °C; the grains are recrystallized and MC carbides are present

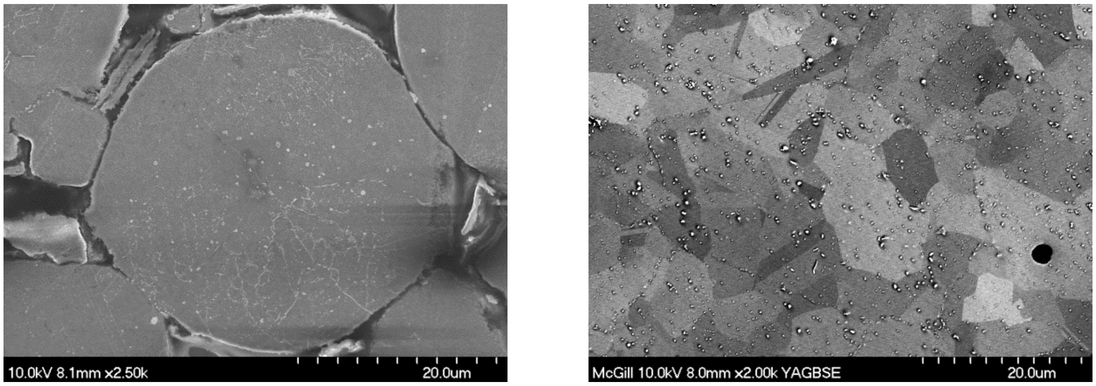

c) Slip cast sample sintered at 1200 °C for 10 min; two regions of the central particle show Laves phases at the prior dendritic structure location and MC carbides are present in recrystallized regions.

d) SPS sample sintered at 1200 °C with a heating rate of 400 °C/min and 1 min holding time; the structure is dotted with MC carbides and a thin PPB carbide chain is present. Notice some grains are crossing the PPB.

Figure 9-4 : Microstructure of samples sintered at 1200 °C
a) CGDS, b) FPSPS, c) Slip cast and d) SPS

Second phase particles located at grain boundaries and within grains (Figure 9.4) were revealed to be MC carbides. Since the eutectic reaction γ+NbC → L only starts at 1247 °C, it is assumed that the MC particles originate from the reaction γ+Laves→L+NbC between the primary phase and the interdendritic region [9.15]. This reaction also involves the nucleation of MC particles within grains following the previous dendritic structure which is what is observed in practice in all samples sintered over 1100 °C. The liquid phase formed in the process migrates to the particle surface because of the pressure applied or by capillary action and essentially wets the particle boundaries and assists consolidation. When the compact temperature decreases during the cooling stage, the liquid at the PPB forms the fine chain of MC carbides rich in Nb. The PPB particles were also found to be rich in Al, Ti and O in many instances, which is in line with the observations of Menzies [9.23] that PPB carbides nucleate on small impurity oxide particles. Therefore, the PPB carbides nucleate from the liquid film present between the particles during SLPS under pressure.

9.5. SUMMARY

Each sintering technique discussed in this section has advantages and drawbacks and it is worthwhile to highlight them.

Starting with the powder-binder compact preparation and pressureless sintering, it is an interesting process for the production of intricate shapes by binder jetting techniques and can be applied more widely to MIM. This route allows achievement of close to full density; however, the reliability of the process depends on the green compact production. Using high heating rates with this technique is beneficial as long as the thermal gradients in the part do not induce unacceptable distortion. On the contrary, fast heating rates can be used to reduce grain coarsening during the heating ramp and prolong the isothermal hold while avoiding slumping.

The CGDS process as a green compact production route holds several advantages: close to 100% green density, low oxygen pickup, flexibility and its binderless characteristic. The main advantage of CGDS is its ability to build up on an existing part. However, the drawback lies in the deposition efficiency of 30%, which should be optimized. This work has shown the feasibility of the CGDS process route when followed by sintering; however, investigation of the sintering treatment effect on the part properties remains to be investigated.

The SPS process advantage over direct HIP is the cycle time, and the simplicity of sample preparation with die filling as opposed to powder encapsulation. On the other hand, the SPS method is limited to flat shapes or cylindrical shapes with a low height to diameter ratio to avoid pressure gradients effects. Near-net-shape parts will demand high development cost for the die design. Die wear and chemical bonding with graphite could also be an issue as was experienced in this study. It is however a very powerful technique, as sintering of Inconel 718 to full density was achieved within minutes.

9.6. REFERENCES

9.1. Youhua, H., et al., *Preparation and Mechanical Properties of Inconel718 Alloy by Metal Injection Molding.* Rare Metal Materials and Engineering, 2010. 39(5): p. 775-780.

9.2. Wohlfromm, H., et al., *Metal Injection Moulding of Nickel-based Superalloys for High Temperature Applications.* Proceedings Euro PM2003 Congr. Exhib., 2003. 3: p. 207-215.

9.3. Valencia, J.J., J. Spirko, and R. Schmees, *Sintering effect on the microstructure and mechanical properties of alloy 718 processed by powder injection molding.* Superalloys 718, 625, 706 and Various Derivatives, 1997: p. 753-762.

9.4. Bose, A., et al., *Powder injection molding of Inconel 718 alloy.* Advances in Powder Metallurgy & Particulate Materials - 1997, 1997: p. 1899-18112.

9.5. Schmees, R., J.R. Spirko, and J. Valencia. *Powder injection molding (PIM) of Inconel 718 aerospace components*. in *Proceedings of the Advanced Particulate Materials & Processes*. 1997.

9.6. Hajmrle, K. and R. Angers, *Sintering of Inconel 718.* International Journal of Powder Metallurgy, 1980. 16(3): p. 255-266.

9.7. German, R.M., *Liquid phase sintering*. 1985: Springer Science & Business Media.

9.8. German, R.M., *Supersolidus liquid-phase sintering of prealloyed powders.* Metallurgical and Materials Transactions A: Physical Metallurgy and Materials Science, 1997. 28(7): p. 1553-1567.

9.9. Liu, Y.X., R. Tandon, and R.M. German, *Modeling of Supersolidus Liquid-Phase Sintering .2. Densification.* Metallurgical and Materials Transactions a-Physical Metallurgy and Materials Science, 1995. 26(9): p. 2423-2430.

9.10. Liu, Y.X., R. Tandon, and R.M. German, *Modeling of Supersolidus Liquid-Phase Sintering .1. Capillary Force.* Metallurgical and Materials Transactions a-Physical Metallurgy and Materials Science, 1995. 26(9): p. 2415-2422.

9.11. Kingery, W., J. Woulbroun, and F. Charvat, *Effects of applied pressure on densification during sintering in the presence of a liquid phase.* Journal of the American Ceramic Society, 1963. 46(8): p. 391-395.

9.12. Rao, G.A., M. Srinivas, and D.S. Sarma, *Effect of oxygen content of powder on microstructure and mechanical properties of hot isostatically pressed superalloy Inconel 718.* Materials Science and Engineering A, 2006. 435: p. 84-99.

9.13. Gessinger, G.H., *Powder metallurgy of superalloys*. Butterworths monographs in materials. 1984, London ; Boston: Butterworths. 348 p.
9.14. Antonsson, T. and H. Fredriksson, *The effect of cooling rate on the solidification of INCONEL 718.* Metallurgical and Materials Transactions B, 2005. 36(1): p. 85-96.
9.15. Kang, S.-H., et al., *Solidification process and behavior of alloying elements in Ni-based superalloy Inconel718.* Materials transactions, 2004. 45(8): p. 2728-2733.
9.16. German, R.M., *Supersolidus liquid-phase sintering of prealloyed powders.* Metallurgical and materials transactions A, 1997. 28(7): p. 1553-1567.
9.17. Liu, J., A. Lal, and R.M. German, *Densification and shape retention in supersolidus liquid phase sintering.* Acta Materialia, 1999. 47(18): p. 4615-4626.
9.18. Lal, A., *Mechanisms and mechanics of shape loss during supersolidus liquid-phase sintering*. 1999, The Pennsylvania State University: Ann Arbor. p. 252-252 p.
9.19. Contreras, J.M., A. Jiménez-Morales, and J.M. Torralba, *Improvement of rheological properties of Inconel 718 MIM feedstock using tailored particle size distributions.* Powder Metallurgy, 2008. 51(2): p. 103-106.
9.20. Reed, R.C., *The superalloys : fundamentals and applications*. 2006, Cambridge, UK; New York: Cambridge University Press.
9.21. Rao, G.A., M. Srinivas, and D.S. Sarma, *Effect of thermomechanical working on the microstructure and mechanical properties of hot isostatically pressed superalloy Inconel 718.* Materials Science and Engineering a-Structural Materials Properties Microstructure and Processing, 2004. 383(2): p. 201-212.
9.22. Rao, G.A., M. Srinivas, and D.S. Sarma, *Effect of solution treatment temperature on microstructure and mechanical properties of hot isostatically pressed superalloy Inconel*718.* Materials Science and Technology, 2004. 20(9): p. 1161-1170.
9.23. Menzies, R.G., R.H. Bricknell, and A.J. Craven, *Stem Microanalysis Of Precipitates And Their Nuclei In A Nickel-Base Super-Alloy.* Philosophical Magazine A, 1980. 41(4): p. 493-508.

CHAPTER 10. CONCLUSION

The conclusions of all result chapter are presented in this chapter followed by general conclusions and suggestions for further study.

1. Liquid phase formation in Inconel 718 powders was characterized by differential scanning calorimetry (DSC). The powder particles exhibited a γ/Laves eutectic at 1098°C–1128°C, where the first liquid was observed. This reaction was followed by the formation of MC carbides through the reaction $\gamma + \text{Laves} \rightarrow L + \text{NbC}$ at 1138°C and the γ/NbC eutectic at 1247°C.

2. The liquid fraction was evaluated as a function of temperature by DSC calculations, and the effect of carbon contamination was assessed using Thermocalc. The effect of carbon contamination was shown to shrink the solidus–liquidus temperature range, increasing the difficulty of sintering control within the SLPS process.

3. The pressureless sintering of Inconel 718 was performed at various temperatures corresponding to increasing liquid phase content; full density was approached at 1250°C, corresponding to a liquid content of 14%.

4. Distortion was predicted using the softening parameter model developed by Liu *et al.* It was shown that sintering at 1290°C should yield distortion-free parts when grain size is under 45 µm. However, sintering at 1300°C will provoke distortion when grain size exceeds 20 µm.

5. The grain growth exponent during sintering of Inconel 718 was determined to be near unity (1.16 on average).
6. CGDS of hard alloys, like Inconel 718, is not sufficient to obtain metal bonds between the deposited particles. However, the CS process can be used advantageously to produce high density green compacts, owing to the necessity that post-deposition sintering is necessary. The pressureless sintering of the CS Inconel 718 powders produced significant gains in flexural strength and ductility (6.5- and 7-fold increases, respectively). Within the tested sintering conditions, the porosity could not be completely remediated; hence, crack propagation sites were still present.

7. The evolution of the grain size during sintering of CS Inconel 718 was found to be strongly correlated with the precipitation of secondary carbides, and rapid grain growth was observed at a sintering temperature of 1250°C.

8. Sintering of Inconel 718 compacts was studied in a specially designed pressureless pulsed electric current sintering assembly at heating rates ranging from to 200 K/min. The final density obtained for each heating rate ranged between 94–99.7% TD. Sintering of Inconel 718 to full density is aided by the formation of a supersolidus liquid phase, as evidenced by the presence of liquid artifacts and the Laves phase during cooling. As such, the sintering behavior could be described by two MSC models that define low (≤50 K/min) and high heating rate (≥75 K/min) behaviors. The apparent activation energy of sintering was statistically similar; a value of 198 kJ/mol, consistent with diffusion data for the species present in Inconel 718, was used for calculations. The difference between the two MSC curves was explained by the difference in liquation kinetics and associated phenomena.

9. Sintering Inconel 718 by SPS produced full density compacts at 1200°C using 50 MPa pressure, a heating rate higher than 400°C/min, and a holding time under 3.5 min. The

microstructure of the sintered Inconel 718 had an average grain size of 5.0–6.5 μm and showed PPB carbides. The sintering mechanism of Inconel 718 relies on the formation of a liquid phase at 1100°C; however, the amount of liquid phase was not sufficient to obtain full density until 1200°C. Pressure reduced the amount of liquid required to obtain a given density. The growth of PPB carbides was found to be positively linked with liquid formation.

Future work in the field of Inconel 718 sintering can follow multiple paths depending on the objective that is pursued. There are process parameters that influence the liquid fraction formation and others that influence the spreading of the liquid, however both will determine the final density of the compact. Temperature, composition and heating rate have an impact on liquid phase formation, whereas particle size distribution, green compact forming process and heating rate will change the distribution of liquid within the powder compact.

If complex parts are sought, the pressureless sintering of green parts produced by metal injection molding or binder jetting is preferred. Then optimization of the sintering cycle should take advantage of the effect of high heating rates to rapidely densify the compact at a very high temperature (1300°C – 1310°C) followed by a soaking period at lower temperature (<1290°C) in order to avoid slumping. The optimization of the green compact should aim at narrowing the pore size distribution and eliminate large pores in order to optimize the liquid phase distribution and pore filling.

The production of protrusions by cold spray is another interesting research direction where more attention should be given to the surface state of the powder particles before and after spraying and its effect on the final properties. Full density was achieved after sintering cold sprayed compacts and the mechanical properties of the resulting part should be characterized both at room temperature and at high temperature.

The study of liquid phase formation at high heating rates is also a relevant field in itself as it impacts on both the welding and sintering processes. The laser based additive manufacturing techniques also require a better understanding of the liquid formation kinetic of Inconel 718 at high heating rates. The effect of initial powder structure and composition is key in determining the process parameters of these manufacturing techniques.

Finally, there is still much to do in order to better understand the complex processes involved in sintering superalloys such as Inconel 718. There are many mechanism active in this process: mass transport, phase change, densification and many parameters influencing the activity of each mechanism.

CHAPTER 11. CONTRIBUTIONS TO ORIGINAL KNOWLEDGE

The principal contributions to the scientific literature stemming from this research work are listed in this section.

1. The softening parameter of Inconel 718 was defined at a value of 0.0064 $\mu m^{1/3}$ for 5-cm-tall parts and the methodology can be used to define the softening parameter of any part dimension. This can be used to analyse the distortion of Inconel 718 during SLPS.

2. The liquid phase formation of Inconel 718 powders was evaluated, as was its role during sintering. It was found that liquid fractions of 14% were able to yield 98% TD or more during pressureless sintering.

3. The CGDS process was found unsuitable for producing dense, consolidated metallic structures with hard alloys such as Inconel 718. However, the sintering post-treatment developed in this work permitted the consolidation of the deposited powder. The density obtained with sintered CGDS deposits was similar to the density obtained after direct HIP treatment of Inconel 718 powders.

4. High heating rates were found to improve the sintering rate. Effectively, the thermal work required for sintering, calculated using the MSC of Inconel 718, was lower for heating rates over 75°C/min.

5. The consolidation of Inconel 718 by SPS was found to sinter Inconel 718 to full density with faster sintering cycle times than direct near-net-shape HIPing. The PPB structure

was related to the liquid spreading along the particle contact regions, and the grain size remained close to the initial powder grain size (<6.5 μm).